DEPARTMENT OF MATERIALS
SCIENCE AND TECHNOLOGY
UNIVERSITY OF CRETE

"RESPONSIVE SELF-ASSEMBLED PEPTIDES BIOMATERIALS AND APPLICATIONS"

Ph.D. THESIS

Chrysanthi Pinelopi Apostolidou,

Biologist

Supervisor: Professor Anna Mitraki

September 2023

ΠΑΝΕΠΙΣΤΗΜΙΟ ΚΡΗΤΗΣ
UNIVERSITY OF CRETE

ΙΣΝ SNF ΙΔΡΥΜΑ ΣΤΑΥΡΟΣ ΝΙΑΡΧΟΣ
STAVROS NIARCHOS FOUNDATION

H.F.R.I.
Hellenic Foundation for
Research & Innovation

Ευρωπαϊκή Ένωση
European Social Fund

Operational Programme
Human Resources Development,
Education and Lifelong Learning

Co-financed by Greece and the European Union

ACKNOWLEDGEMENTS

I would like to express my heartfelt gratitude to my supervisor, Professor Anna Mitraki from the Department of Materials Science and Technology, for her guidance, patience, and motivation throughout my PhD thesis. Her immense knowledge and profound experience have been instrumental in my growth as a scientist, and I am truly grateful for the opportunity I was given to work under her supervision.

Also, I would like to thank my advisory committee, Assistant Professor Kelly Velonia, and Associate Professor Maria Chatzinikolaidou for their support, insightful comments, and collaboration In addition, I would like to thank the other members of my committee

Professor Athanasios Coutsolelo and Dr. Georgios Charalampidis, for our long and fruitful collaboration as well as Professor Maria Vamvakaki and Dr. Androniki Kretsovali for their help and support.

I am deeply grateful to the staff of the Electron Microscopy Facility at the Biology Department, especially Aleka Manousaki and, also, Eva Papadogiorgaki, and Stefanos Papadakis, for their assistance with electron microscopy observations and valuable discussions.

Moreover, I would like to thank my colleagues Dr. Vasilis Nikolaou, Dr. Georgios Landrou, Dr. Manos Nikoloudakis, MSc Mara Kandili, and MSc Eleni Glymenaki from the Chemistry Department for our collaboration. Also, my colleagues from the department of Materials and Technology Science, MSc Varvara Platania, BSc Nikoleta Tavernaraki, and MSc Konstantinos Loukelis for our excellent collaboration and exchange of ideas.

I would like to express a special thanks to Dr. Chrysoula Kokotidou, my teammate, for her invaluable help, support, and guidance throughout my research journey. Also, my deepest gratitude goes to my fellow lab mates for their support and encouragement,

Marita, Petros, Giorgos, Konstantina, Aggelina, Marietta, Simatos, Graziano, Evitina

Their presence, evening discussions, exchange of ideas, and the fun we shared have made this scientific journey even more memorable. I wish all the best for all of you!

I am also grateful for the financial support during the years provided by the Stavros Niarchos Foundation within the framework of the project ARCHERS ("Advancing Young Researchers' Human Capital in Cutting Edge Technologies in the Preservation

of Cultural Heritage and the Tackling of Societal Challenges") (2018-2019), the Hellenic Foundation for Research and Innovation (HFRI) under the HFRI PhD Fellowship grant (Fellowship Number:390) and, lastly, the implementation of the doctoral thesis was co-financed by Greece and the European Union (European Social Fund-ESF) through the Operational Programme «Human Resources Development, Education and Lifelong Learning» in the context of the Act "Enhancing Human Resources Research Potential by undertaking a Doctoral Research" Sub-action 2: IKY Scholarship Programme for PhD candidates in the Greek Universities».

Finally, I dedicate this Ph.D. thesis to my parents, Anna and Apostolos, my brother Giorgos, and my partner Paolo. Their unwavering love, continuous patience, and endless support have been the foundation of my success, and I am forever grateful.

TABLE OF CONTENTS

Table of Figures

SUMMARY

This dissertation focuses on a class of materials that have been designed to exhibit a response to external stimuli such as light, pH, and metals. Commonly referred “as "smart materials," these substances present promising opportunities in a myriad of applications, from bioimaging to antimicrobial and anticancer therapies.

Chapter I presents a general introduction about the peptides, one prime example of such materials. Due to the complex process of protein self-assembly, peptides play a pivotal role in research, serving as foundational components in the development of these novel materials. Biologically, peptides inherently self-assemble into a diverse array of organized structures using a bottom-up approach. Their inherent biocompatibility, biodegradability, and bio-functionality make them prime candidates for such investigations.

This thesis is organized into three primary chapters, each centered on the specific stimulus to which these materials are responsive.

Chapter 2 provides a deep dive into the ability of the dipeptide Fmoc-FF to be used as a light-responsive delivery vehicle. This peptide sequence possesses the inherent capacity to assemble into a three-dimensional hydrogel under physiological conditions. By encapsulating a chromophore molecule, this hydrogel gains the ability to respond to light and form antimicrobial structures. Our research specifically revolved around the investigation of such antimicrobial properties for hydrogels encapsulating porphyrins. In particular, we focused on the cationic porphyrins $H_2T(MePy)P(I_4)$, Zn-$T(MePy)P(I_4)$, and Zn-$T(MePy)P(Cl_4)$, chosen for their distinct structural properties. Field-emission scanning electron microscopy (FESEM) was employed to analyze the morphology of both the scaffold and the embedded structures, which appeared as fibrillar. Additionally, we conducted mechanical tests to assess how the association with porphyrins affected their structural rigidity, revealing that the encapsulation of $H_2T(MePy)P(I_4)$ produced the least rigid structure. Finally, the antimicrobial efficacy was assessed against both Gram-positive and Gram-negative bacterial strains.

In Chapter 3, we present our work related to the development of fluorescent molecules for bioimaging. The broader target was to design trackers which could enter a cancer cell and hence allow its visual detection. In particular, we adopted

peptide sequences containing histidine, which have the potential to coordinate with porphyrin-modified nitrilotriacetic acid (NTA) (chromophores) through metal chelation. This constituted our fluorescent probes tailored for bioimaging applications within cancer cells. Two peptides, namely RDSGAITIGH and the protected dipeptide Fmoc-FH, were at the center of our investigations. Both peptides inherently contain histidine residues in their structures. We confirmed the successful formation of the hybrids via FESEM imaging, and observed the peptide-porphyrin coordination generated structures which were morphologically different from those of the peptides or porphyrins alone. Moreover, this was complemented with UV-Vis spectroscopy measurements, which confirmed the successful coordination. Finally, the coordinated systems were studied for their ability to penetrate HeLa cancer cells.

Finally, Chapter 4 reports our endeavor of assembling biocompatible nanoparticles carrying metal ions, which could be used for antibacterial or anticancer applications. In particular, we studied a cyclic-HF peptide as a coordinating agent for copper and zinc ions. FESEM imaging combined with EDX showed that the fibrillar structure formed by the peptide alone were modified into flower-like in the presence of copper ions indicating that CuO nanoparticles (NPs) were formed, and into spherical ones in the presence of zinc ions indicating that ZnO NPs were formed, which proved the successful coordination. Testing against Gram-positive and Gram-negative bacterial strains provided indication that the CuO NPs are slightly more efficient than ZnO NPs in terms of antimicrobial effect. Moreover, tests performed in tumoral environments showed an increased antitumor efficiency of both NPs, due to the low pH which favors the release of the metal ions.

Synthesis of all porphyrin molecules was carried out by the members of Prof. Coutsolelos group, namely Georgios Charalambidis, Georgios Landrou, Vasilis Nikolaou, Manos Nikoloudakis, Eleni Glymenaki and Maria Kandyli, in the framework of a long term-collaboration of the two groups and part of the research was co-financed by the European Union and Greek national funds through the Operational Program Competitiveness, Entrepreneurship, and Innovation, under the call RESEARCH – CREATE – INNOVATE (project Acronym : EPHESIAN, project code: T1EDK-01504).

ΠΕΡΙΛΗΨΗ

«Αποκρίσιμα Αυτοοργανωμένα Πεπτιδικά Βιοϋλικά και Εφαρμογές»

Η παρούσα διδακτορική διατριβή επικεντρώνεται σε βιοϋλικά, τα οποία έχουν σχεδιαστεί για να αποκρίνονται σε διάφορους εξωτερικούς παράγοντες όπως το φως, το pH και τα μέταλλα. Αυτά τα υλικά, γνωστά ως "έξυπνα υλικά" προσφέρουν πολλές δυνατότητες σε πληθώρα εφαρμογών, από τη βιοαπεικόνιση έως τις αντιμικροβιακές και αντικαρκινικές θεραπείες.

Το κεφάλαιο Ι παρουσιάζει μια γενική εισαγωγή σχετικά με τα πεπτίδια, τα οποία αποτελούν παράδειγμα αυτών των υλικών. Λόγω της πολύπλοκης διαδικασίας οργάνωσης των πρωτεϊνών, τα πεπτίδια έχουν κερδίσει το ενδιαφέρον των ερευνητών και παίζουν καίριο ρόλο στην έρευνα, λειτουργώντας ως θεμελιώδη στοιχεία στην ανάπτυξη των νέων υλικών. Βιολογικά, τα πεπτίδια αυτοοργανώνονται ακολουθώντας μια προσέγγιση " bottom-up " , όπου μεμονωμένα άτομα και μόρια σχηματίζουν μεγαλύτερες νανοδομές. Τα υλικά αυτά είναι βιοσυμβατά, βιο-αποκοδομήσιμα και βιο-λειτουργικά και γι’ αυτό θεωρούνται κατάλληλα για βιολογικές έρευνες.

Η διατριβή χωρίζεται σε τρία κύρια κεφάλαια, το καθένα από τα οποία επικεντρώνεται στην μελέτη πεπτιδικών ακολουθιών, οι οποίες διακρίνονται για την αποκρισιμότητα τους σε κάποιο εξωτερικό ερέθισμα.

Στο κεφάλαιο 2 μελετήθηκε η ικανότητα του διπεπτιδίου Fmoc-FF να χρησιμοποιείται ως μέσο μεταφοράς που ανταποκρίνεται στο φως. Αυτή η πεπτιδική αλληλουχία διαθέτει την εγγενή ικανότητα να αυτοοργανώνεται και να σχηματίζει τρισδιάστατη υδρογέλη υπό φυσιολογικές συνθήκες. Η υδρογέλη αυτή, ενθυλακώνοντας ένα μόριο χρωμοφόρου, έχει την ικανότητα να ενεργοποιείται από το φως και να σχηματίζει δομές με αντιμικροβιακή δράση. Η έρευνά μας επικεντρώθηκε γύρω από τη διερεύνηση τέτοιων αντιμικροβιακών ιδιοτήτων για υδρογέλες που ενθυλακώνουν πορφυρίνες. Συγκεκριμένα, επικεντρωθήκαμε στις κατιονικές πορφυρίνες H_2-T(MePy)P(I_4), Zn-T(MePy)P(I_4) και Zn-T(MePy)P(Cl_4), οι οποίες επιλέχθηκαν για τις ξεχωριστές δομικές τους ιδιότητες. Χρησιμοποιήθηκε σάρωση εκπομπής πεδίου (FESEM) για την ανάλυση της μορφολογίας τόσο του ικριώματος όσο και των δομών, ύστερα από την εγκαψυλίωση των πορφυρινών. Οι

δομές αυτές εμφάνισαν ινώδη διαμόρφωση. Επιπλέον, πραγματοποιήσαμε μηχανικές δοκιμές για να αξιολογήσουμε κατά πόσο η ένωση με τις πορφυρίνες επηρέασε τη δομική τους δυσκαμψία, αποκαλύπτοντας ότι η ενθυλάκωση της μη μεταλλωμένης πορφυρίνης H_2-T(MePy)P(I_4) παρήγαγε τη λιγότερο δύσκαμπτη δομή. Τέλος, αξιολογήθηκε η αντιμικροβιακή αποτελεσματικότητα των υδρογελών έναντι τόσο θετικών κατά Gram όσο και αρνητικών κατά Gram βακτηριακών στελεχών.

Στο κεφάλαιο 3, παρουσιάζουμε την ανάπτυξη φθοριζόντων μορίων για χρήση στον τομέα της βιοαπεικόνισης. Ο ευρύτερος στόχος ήταν ο σχεδιασμός μορίων-ανιχνευτών που θα μπορούσαν να εισέλθουν σε ένα καρκινικό κύτταρο και, ως εκ τούτου, να επιτρέψουν την οπτική ανίχνευσή του. Συγκεκριμένα, εστιάσαμε τη μελέτη μας σε πεπτιδικές αλληλουχίες που περιέχουν ιστιδίνη, οι οποίες έχουν τη δυνατότητα να συναρμόζονται με πορφυρίνες τροποποιημένες με NTA (χρωμοφόρα) μέσω χηλικής σύνδεσης μετάλλων. Αυτό αποτέλεσε τους φθορίζοντες ανιχνευτές μας, προσαρμοσμένους για εφαρμογές βιοαπεικόνισης εντός καρκινικών κυττάρων. Δύο πεπτίδια, συγκεκριμένα το RDSGAITIGH και το προστατευμένο διπεπτίδιο Fmoc-FH, βρέθηκαν στο επίκεντρο των ερευνών μας. Και τα δύο πεπτίδια περιέχουν εγγενώς στη δομή τους κατάλοιπα ιστιδίνης. Επιβεβαιώσαμε τον επιτυχή σχηματισμό των υβριδίων μέσω απεικόνισης FESEM και παρατηρήσαμε ότι η συναρμογή πεπτιδίου-πορφυρίνης παρήγαγε δομές που ήταν μορφολογικά διαφορετικές από εκείνες των πεπτιδίων ή των πορφυρινών μόνων τους. Επιπλέον, μετρήσεις φασματοσκοπίας UV-Vis επιβεβαίωσαν την επιτυχή συναρμογή. Τέλος, τα συναρμοσμένα συστήματα μελετήθηκαν ως προς την ικανότητά τους να διεισδύουν σε καρκινικά κύτταρα HeLa.

Τέλος, στο κεφάλαιο 4 επικεντρωθήκαμε στο σχηματισμό νανοσωματίδιων που μπορούν να μεταφέρουν μεταλλικά ιόντα, τα οποία μπορούν να χρησιμοποιηθούν για αντιβακτηριακές ή αντικαρκινικές εφαρμογές. Συγκεκριμένα, μελετήσαμε το κυκλικό πεπτίδιο-ιστιδίνης φαινυλανανίνης και την ικανότητα του να συναρμόζεται με ιόντα χαλκού και ψευδαργύρου. Η παρατήρηση με μικροσκοπία FESEM και διεξαγωγή EDX έδειξαν ότι η ινώδης διαμόρφωση του πεπτιδίου, τροποποιήθηκε σε δομές-«σαν λουλούδια» ύστερα από την παρουσία ιόντων χαλκού, υποδηλώνοντας ότι δημιουργήθηκαν σύμπλοκα με νανοσωματίδια CuO, και σε σφαιρικές δομές ύστερα από την παρουσία ιόντων ψευδαργύρου, υποδηλώνοντας ότι δημιουργήθηκαν σύμπλοκα με νανοσωματίδια ZnO, κάτι που αποδεικνύει την επιτυχή συναρμογή. Οι δοκιμές έναντι Gram-θετικών και Gram-αρνητικών βακτηριακών στελεχών απέδειξαν ότι τα νανοσωματίδια χαλκού είναι ελαφρώς πιο αποτελεσματικά από τα

νανοσωματίδια ZnO όσον αφορά την αντιμικροβιακή δράση. Επιπλέον, δοκιμές που πραγματοποιήθηκαν σε καρκινικά κύτταρα σε pH 6.4 έδειξαν αυξημένη αντικαρκινική αποτελεσματικότητα και των δύο νανοσωματιδίων, λόγω του χαμηλού pH που ευνοεί την απελευθέρωση των μεταλλικών ιόντων.

Η σύνθεση όλων των μορίων πορφυρίνης πραγματοποιήθηκε από τα μέλη της ομάδας του καθηγητή Αθανάσιου Κουτσολέλου, και πιο συγκεκριμένα από τους Γιώργο Χαραλαμπίδη, Γιώργο Λάνδρου, Βασίλη Νικολάου, Μάνο Νικολουδάκη, Ελένη Γλυμενάκη, και Μαρία Κανδύλη στα πλαίσια μιας μακροχρόνιας συνεργασίας των δύο ομάδων και συν-χρηματοδοτήθηκε από το Επιχειρησιακό Πρόγραμμα "Ανταγωνιστικότητα, Επιχειρηματικότητα και Καινοτομία" 2014-2020 (ΕΠΑΝΕΚ) στο πλαίσιο της δράσης "ΕΡΕΥΝΩ- ΔΗΜΙΟΥΡΓΩ – ΚΑΙΝΟΤΟΜΩ " με ακρωνύμιο “EPHESIAN” και κωδικό έργου Τ1ΕΔΚ-01504.

1. General Introduction

1.1 Proteins and Peptides

Proteins and peptides are composed of amino acid sequences linked by peptide bonds. These essential biomolecules play a significant role in regulating various physiological processes within our body, which are vital for the proper functioning of cells and sustaining life (1). In nature, while there are 22 amino acids, the sequence of amino acids in the polypeptide chain determines their primary structure, and then their function (2). Each amino acid differs by its unique R group, which can feature entities such as hydroxyl (-OH), amino ($-NH_2$), carboxyl (-COOH), sulfhydryl (-SH), or aromatic rings. Chemically, the formation of peptide bonds involves amino acids undergoing a condensation reaction, where the amino group of one amino acid reacts with the carboxyl group of another amino acid, and it is facilitated catalytically by the large subunit of the ribosome (Figure 1) (3).

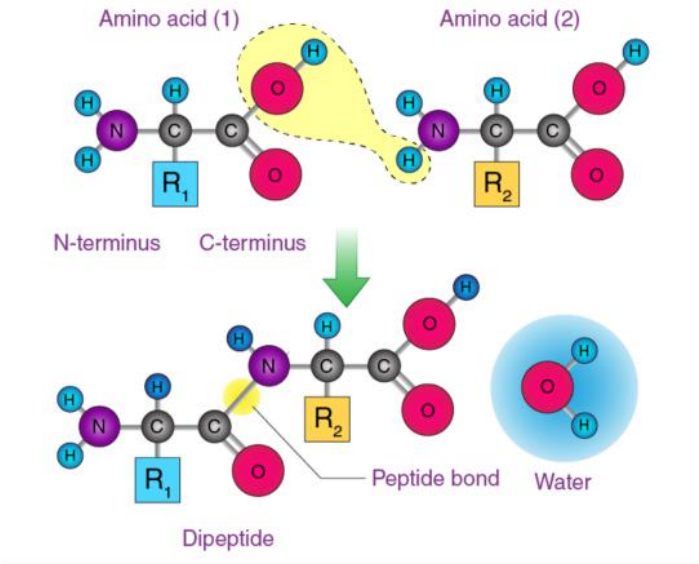

Figure 1: The formation of a peptide bond between two amino acids by a condensation reaction. Picture [source].

Unlike proteins produced by ribosomal synthesis (4), the synthesis of the peptide in the lab follows the solid-phase peptide synthesis (SPPS). The SSPS allows the formation of peptide bonds on an insoluble polymeric support (resin), where a single cleavage permits obtaining the desired peptide in solution (5).

1.2 Linear and Cyclic Peptides

Moving deeper into the world of peptides, consisting of two or more amino acids (typically fewer than 50) (6), one discovers the fascinating distinction between linear and cyclic peptides (CPs). Due to their differences in structural topology, they exhibit contrasting self-assembled patterns and thermal stabilities. Linear peptides are structurally flexible and offer a wide range of conformations and interactions; they have several drawbacks, such as instability, poor cellular uptake, and challenges in their conversion to drug-like compounds (7). On the other hand, cyclic dipeptides or diketopiperazines (DKPs) (8) with their restricted and defined structure, provide unique properties that make them attractive in various applications, especially in drug design and nanotechnology. Cyclic peptides, due to their small size (approximately ∼500−3000 Da) (8,9), and the absence of amino and carboxylic ends, are resistant to hydrolysis by intestinal exopeptidases (9). In addition, their rigid structure may enhance their ability to passively cross membranes and localize intracellular targets (7). Moreover, the cyclization limits the conformational flexibility of peptides (11) and increases their ability to bind with greater affinity to various target molecules or certain metal ions (12). For example, the metal binding of zinc or copper ions to the cyclopeptide oxytocin induces conformational changes (13), which can affect the hormone secretion and stability. In the therapeutic field, cyclic peptides offer a plethora of advantages due to precise targeting, rigidity, and few side effects (14).

1.3 Molecular Organization

The molecular organization of proteins critically influences their functionality (15). Linus Pauling (1951) first described the secondary structure of proteins and laid the foundation for our understanding of protein structure and function (4). Proteins and peptides fold into various three-dimensional structures, including the two most common secondary structures: alpha helices and beta sheets, and play vital roles in biological systems (Figure 2).

The alpha helix is a spiral-shaped structure formed by a polypeptide chain. It is stabilized by intramolecular hydrogen bonds between the carbonyl oxygen of one amino acid and the amide hydrogen of an amino acid four residues down the chain. The rotation of the helix can be either clockwise or counterclockwise, with the former being more energetically favored due to fewer steric clashes between the side chains and the backbone (16).

On the other hand, beta sheets consist of beta strands, which are polypeptide chains of 3 to 10 amino acids long with extended conformations. Beta strands can align in a parallel or antiparallel manner to form beta sheets. In parallel beta sheets, neighboring strands run in the same direction, while in antiparallel beta sheets, neighboring strands run in opposite directions. The alignment of beta strands is stabilized by hydrogen bonds between the carbonyl oxygen of one strand and the amide hydrogen of an adjacent strand, forming a twisted, pleated sheet (17).

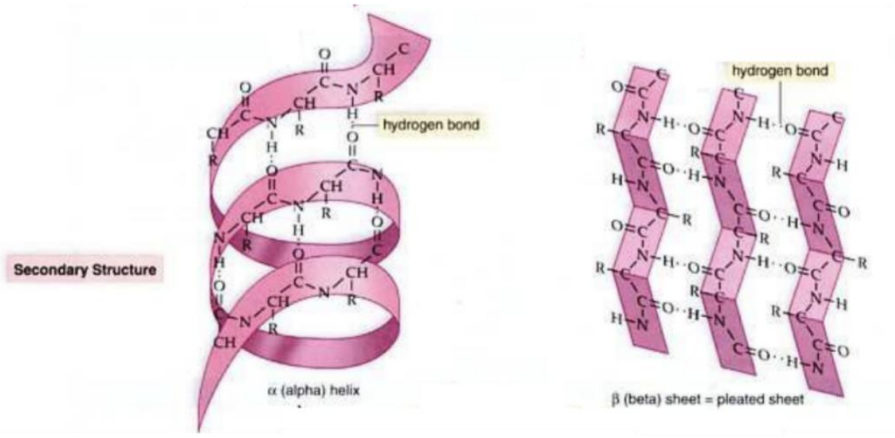

Figure 2: Secondary Structure in protein organization (18).

1.4 Self-Assembly Process

In recent years, peptides have attracted immense attention in research as a minimal building block for the fabrication of materials, due to the complexity of the protein organization process. Self-assembly of peptides is a spontaneous process that follows the bottom-up approach, where atoms, molecules, or clusters organize into well-ordered structures (19) of various sizes and shapes (20). This process of fabrication of novel materials (also "molecular nanotechnology"), is opposed to the top-down

approach, which involves breaking down a bulk material into nanosized structures or particles, such as nanowires (Figure 3) (21).

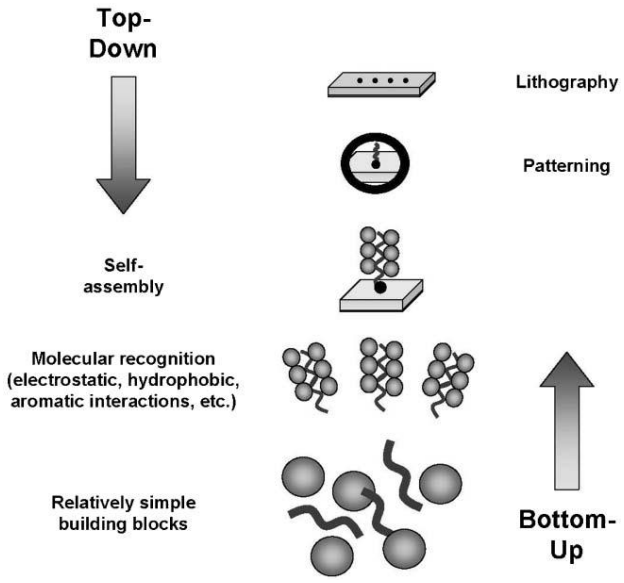

Figure 3: Schematic representation of the "top-down" and "bottom-up" self-assembly process (21).

The self-assembly of peptides is driven by weak non-covalent interactions, such as hydrophobic forces, hydrogen bonding, electrostatic, van der Waals forces, and aromatic stacking between their amino acid groups, influenced by various external conditions, such as temperature, ionic strength, pH, or light. In response to both internal and external stimuli, peptides can undergo self-assembly, forming various amyloid nanostructures (Figure 4) including zero-dimensional (0D) entities like nanoparticles and nanospheres, one-dimensional (1D) structures such as nanofibrils and nanotubes (22) , two-dimensional (2D) configurations like nanosheets, ribbons, and nanofilms, as well as three-dimensional (3D) structures including hydrogels, aerogels, and scaffolds (23,24) . Additionally, the well-organized nanostructures and their mechanical properties can be modulated by several key factors including the sequence of amino acids, the length of the peptides, the concentration of peptides, the chiral arrangement of amino acids, and the involvement of different ions (25).

Self-assembly is a very important process in both science and technology, facilitating the formation of innovative biomaterials that possess remarkable potential across various applications, from tissue engineering and controlled drug delivery to microelectronics.

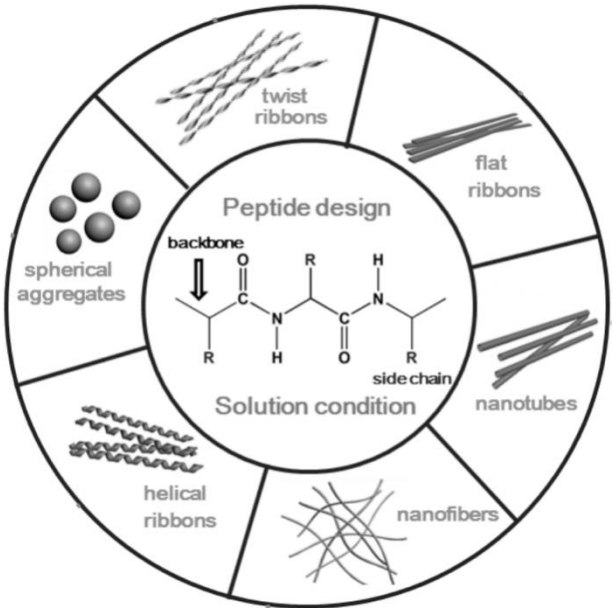

Figure 4: A schematic representation of self-assembled nanostructures (26).

1.4.1 Amyloid Fibrils

Natural proteins in their native state adopt specific three-dimensional structures in living organisms, that are crucial for their physiological activities. However, harsh conditions, such as genetic mutations, environmental stress, changes in pH, elevated temperature, or chemical modifications can lead to the adoption of an alternative conformation (27).

The formation of amyloid fibrils is the result of the misfolding of normally soluble proteins or the self-assembly of peptides (28). These abnormal proteins, also called amyloids, can form a characteristic insoluble filament-like structure that exhibits resilience to proteolytic degradation and denaturation (29). Structural studies reveal that these fibrils share a characteristic "cross-β" core structure, primarily composed of a β-sheet-rich structure that runs parallel to the long fibril's axis with diameters ranging from 100–200 Å (30,31). The mainly stabilizing interaction is due to the intermolecular hydrogen bonding between beta-strands of the main chain (32), while two or more β-sheets are held together by hydrophobic surface contacts or electrostatic interactions (33). The cross beta structure is highly conserved and amyloid fibrils are found to accumulate extracellularly in tissues, amyloids have been

associated with pathological disorders, such as Alzheimer's disease, Parkinson's disease, Huntington's disease, and type 2 diabetes (34).

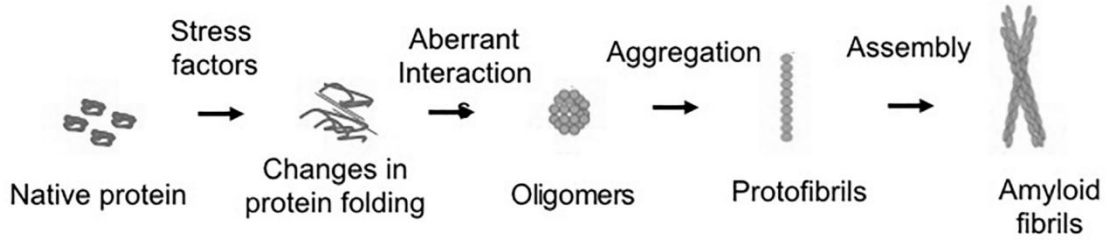

Figure 5: Diagram depicting the typical pathway of protein aggregation.The biologically active native protein structure can experience alterations that result in unfolding or misfolding. Hydrophobic motifs come together to create oligomeric structures. These smaller oligomer aggregates then contribute to the development of protofibrils, ultimately culminating in the creation of fully formed fibrillar structures (35).

1.4.1.1 Characterization Methods of amyloid fibrils

The discovery of amyloids dates back over 160 years; however, it is only in recent years that notable progress has been achieved in determining the atomic structure of amyloid fibrillar assemblies using cryo-electron microscopy. Amyloid fibrils exhibit a characteristic X-ray diffraction pattern that is commonly observed among different types of amyloids. This pattern typically reveals a distinct reflection at approximately 4.7 Å in the meridian direction and another reflection at around 10 Å in the equatorial direction. These reflections correspond to the distances between the strands within the fibril and the stacking distances between beta sheets, respectively (36).

Amyloid fibrils are characterized using specific amyloid dyes such as Thioflavin T (ThT) and Congo Red (CR) (37) . Congo red binds to amyloid fibrils and leads to a characteristic yellow-green birefringence under crossed polarizers (38) . Similarly, thioflavin (ThT) binds to amyloids and the strong fluorescence signal at 480 nm, after the excitation at 440-450 nm, serves as the confirmation of amyloid formation (39).

In addition, microscopic techniques can be employed to characterize and verify the amyloid nature of an assembled moiety. Transmission Electron Microscopy (TEM), Scanning Electron Microscopy (SEM), and Atomic Force Microscopy (AFM) are electron microscopy techniques that can justify the distinct structure of amyloids characterized by long, intertwined, and unbranched fibrils with a width ranging from 7 to 20 nm (40).

In recent times, to overcome the limitations of traditional microscope techniques, cryo-transmission electron microscopy (cryo-TEM) and solid-state NMR spectroscopy have been employed to gain deeper structural insights into amyloid fibrils. These cutting-edge methods enable the visualization of the fundamental structure of the amyloid core and provide valuable information about the intricate structural details of amyloid assemblies (41). More recently, the development of high resolution cryo-electron microscopy techniques led to formidable structural achievements such as the determination of the Aβ Alzheimer's peptide structure (42), or even of tau filaments from the brains of diseased patients (43).

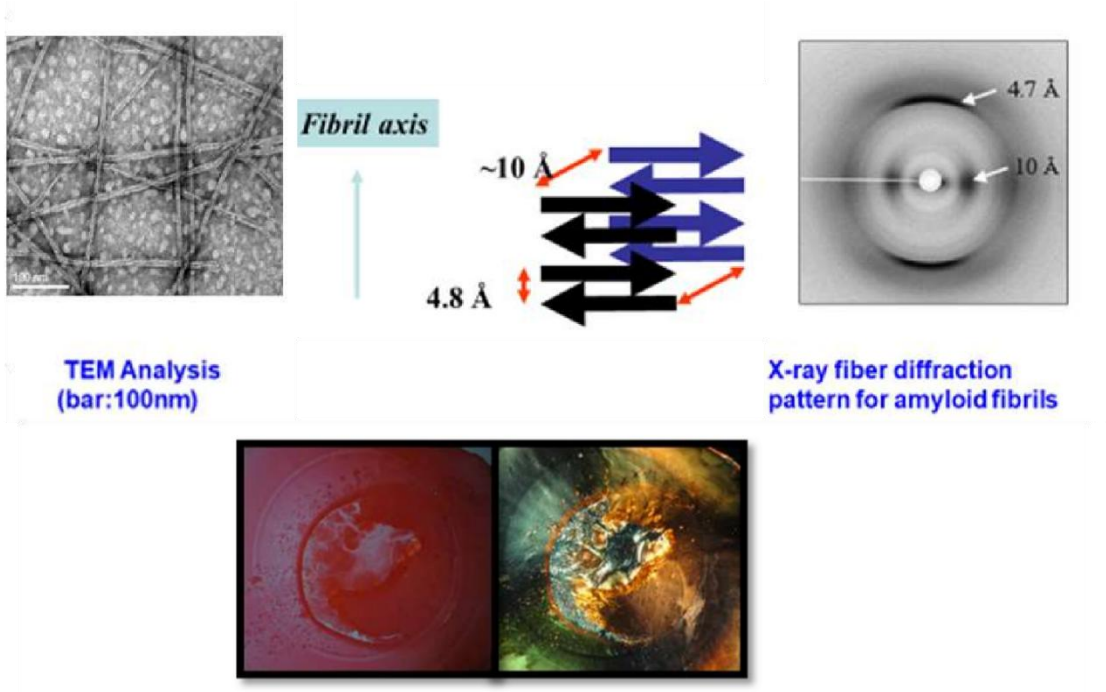

Figure 6: The formation of amyloid fibrils is confirmed by various methods: A) Transmission Electron microscopy (upper left), The cross-beta model is illustrated in the middle, and the X-ray fiber diffraction pattern (upper right), Congo Red staining of amyloid fibrils as visualized under an optical microscope without (bottom left) and with (bottom right) the use of a crossed polarizer. The yellow/green birefringence is a common characteristic of amyloids.

1.4.2 Hydrogel Nanostructures

Amyloid fibrils, when entangled, form a three-dimensional network that retains considerable amounts of water or other biological fluids. This characteristic enhances the ease of hydrogel fabrication (44,45). The pioneering work of Wichterle and Lim

(1960) in synthesizing soft contact lenses introduced a groundbreaking method for the innovative use of hydrogels in biomedical applications (46).

Hydrogels exhibit a remarkable degree of biocompatibility, biodegradability, and biofunctionality, due to the high porosity and their flexibility, which resembles the extracellular matrix (47). Moreover, they can be produced in substantial quantities and used for the encapsulation and controlled release of drugs and biomolecules, such as anti-inflammatory agents or photosensitizers (i.e. porphyrins) to induce release and accelerate the wound healing (48,49). As a result, they are suitable for a wide range of applications, such as tissue engineering, drug delivery systems, and wound healing, which mimic natural proteins (49).

The gelation process of the peptide-based hydrogels mainly relies on cooperative effects of non-covalent interactions, including hydrogen bonds, hydrophobic, and π-π aromatic interactions (30). These hydrogels are also called "smart materials" because they are influenced by stimuli factors, such as pH, temperature, ionic strength, and the sequence of the amino acids (47).

The first self-assembling peptide derived from a natural yeast protein is the repetitive sequence of 16 amino acids, AEAEAKAKAEAEAKAK (EAK16) (25). While many researchers have focused on smaller peptide sequences to form hydrogels, the aliphatic-aromatic dipeptide Isoleucine-Phenylananine (Ile-Phe) has been identified as the smallest hydrogelator composed of natural amino acids (50). The aliphatic-aromatic dipeptide Ile-Phe can form a transparent and thermo-reversible hydrogel without containing any non-coded amino acids or N-terminal modifications (51). Nonetheless, short oligopeptides lacking N-modifications and devoid of any chemical linkages usually cannot function as hydrogelators. To promote the hydrogelation process, aromatic groups are added. Commonly, aromatic groups like fluorenyl methoxycarbonyl (Fmoc), benzyloxycarbonyl (Cbz), naphthoyl, or pyrenyl groups are utilized to improve the mechanical and gelation properties of the small peptides at the N-terminus due to the π-π interactions (52). Further, numerous studies have found that N-(fluorenyl-9-methoxycarbonyl) amino acids exhibit a broad range of anti-inflammatory activity (53) The fluorenylmethoxy-carbonyl-modified aromatic

dipeptide Phe-Phe serves as minimal building block capable of self-assembling and forming hydrogels at physiological pH (54). Therefore, short and ultra-short peptide sequences have been recognized as alternative, easily controllable, and versatile building blocks for creating supramolecular systems. These short amino acid sequences form a family of advanced materials, offering new possibilities for biomedical research and applications (55).

1.5 Responsive Materials

In the field of advanced materials, stimuli-responsive biomolecules have gained significant attention. They display a unique capability to undergo controlled conformational changes in response to external stimuli like temperature, pH, light, metal ions, and enzymes (56). The adaptability of these materials allows them to transition between states, morphologies, or functionalities, making them ideal for a variety of applications.

1.5.1 Light-Responsive Materials

The light-responsive materials present a fascinating avenue in the world of advanced materials. This class of materials normally incorporates a light-sensitive ligand such as the azobenzene group or porphyrins with a functional peptide or protein sequence (56). A key molecule that is central to this field of light-responsive materials is porphyrin. Porphyrins represent a unique class of organic chromophores, capable of absorbing and emitting light, offering a plethora of applications.

They are derived from porphines (57), which are known as critical constituents in natural macromolecules such as hemoglobin and chlorophyll (58,59). Heme is a porphyrin pigment responsible for oxygen transport in red blood cells. It forms the active site of hemoglobin, the protein that carries oxygen in the bloodstream. Chlorophyll, on the other hand, is the porphyrin pigment found in plants and algae that is crucial for capturing light energy during photosynthesis (60).

Porphyrin is an 18 π aromatic macrocyclic compound. It consists of four pyrrole units, which are five-membered aromatic rings, connected by methine (CH) bridges. Its

aromaticity, stemming from the 18-π electron system, (61) , leading to enhanced stability and unique chemical properties. The planar conformation of porphyrin is important for its function as it allows the efficient electron transfer and interactions with other molecules (62).

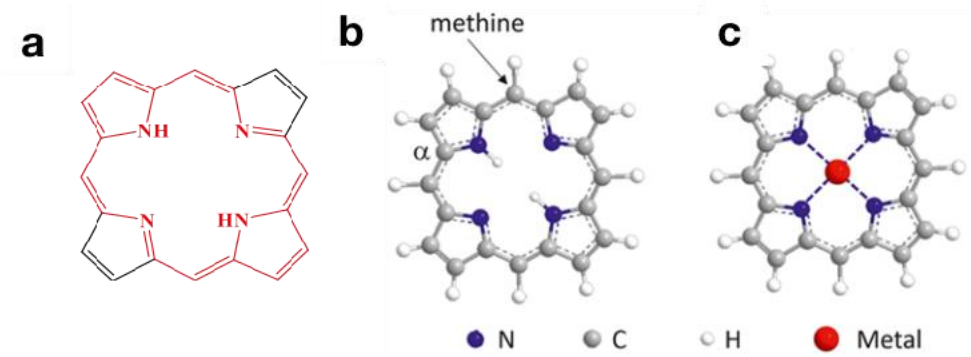

Figure 7: a) The π-electrons of the porphyrin macrocycle that controls aromaticity (depicted in red) b) Three-dimensional molecular structure of porphyrin and (c) metalloporphyrin (63).

The diversity of porphyrin functions can be attributed to the ability of different metal ions (iron zinc, copper) to bind at the core of the porphyrin ring system (64) . Porphyrins are capable of absorbing at wavelengths in the visible range, obtaining their high-intensity absorption peak at 400 nm due to electronic transitions within the porphyrin molecule (65). For wavelengths longer than 450 nm, known as the Q-band region, the absorption coefficients are associated with transitions between excited electronic states of the porphyrin molecule (66).

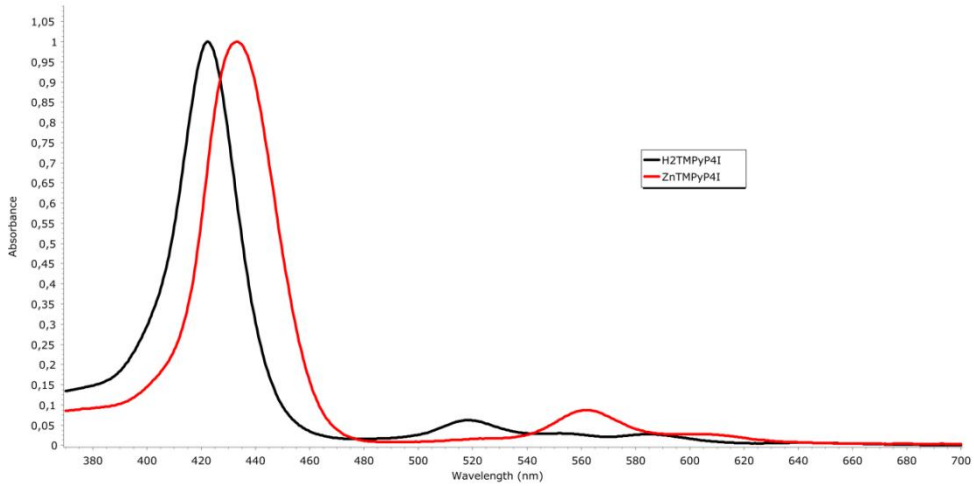

Figure 8: Absorbance Spectra of porphyrin and metallo-porphryrin derivatives.

Upon light activation, the porphyrins and their derivatives catalyze peroxidase and oxidase reactions, absorb photons, and generate reactive oxygen species (ROS), mainly singlet oxygen (Figure 9). Due to the oxidative radicals, a sequence of oxidative reactions occurs in the cell environment that results in the lysis of target cells or organisms, and thereby cell death (Figure 9) (67).

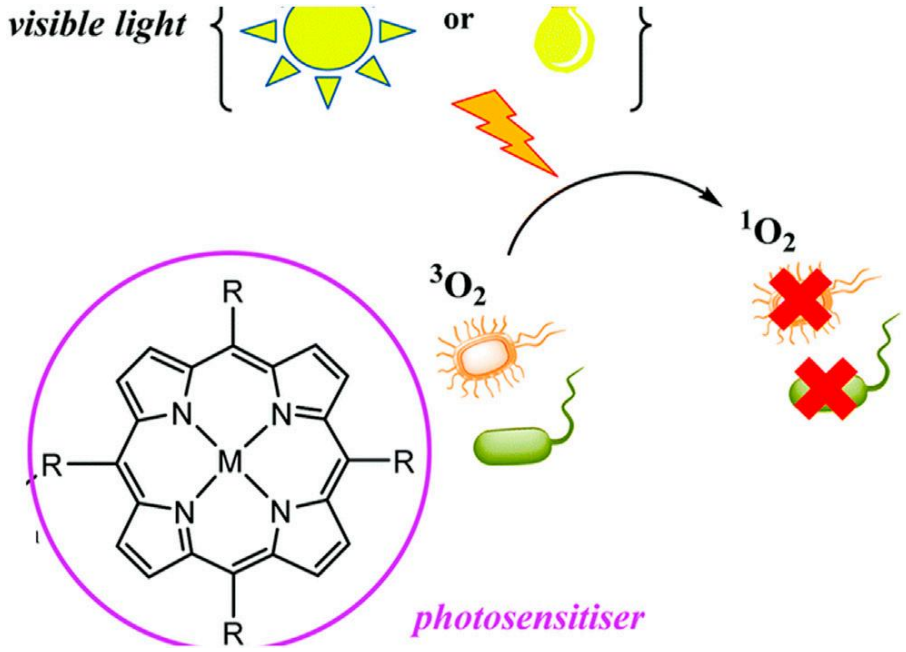

Figure 9: Schematic representation of a generation of singlet oxygen upon irradiation by light, which leads to microorganism death (68).

In conclusion, the light absorption and fluorescence emission (69) render porphyrins invaluable for fluorescence imaging, thus upgrading the field of bioimaging and diagnostics. In addition, their encapsulation into materials enhances the materials' response to light, making them promising photosensitizers (PSs) in photodynamic therapy applications (PDT) (70) However, while there have been significant advancements, particularly with the clinical approval of Photofrin® in cancer treatment, continued research is pivotal to overcome existing challenges and to further unlock the porphyrins in biomedicine (71).

1.5.2 Metal Responsive Materials

In nature, the metal-including biomolecule interactions are of paramount importance in determining the architecture and operational functionality of metalloproteins (72). Metal ions participate as co-factors at approximately one-third of proteins and enzymes, which impart structural, regulatory, and enzymatic functions (73). For instance, the zinc-finger protein demonstrates metal-mediated higher-order organization through its multiple finger motifs, each holding a Zn (II) ion coordinated by His or Cys residues, crucial for DNA binding and stabilization (74).

The stabilization of proteins often occurs through several various metal ions like Cu (II), Zn (II), Mg (II), and Ni (II) at distinct binding sites. These sites are characterized by the presence of amino acid residues like histidine (His), cysteine (Cys), and tryptophan (Trp), which can act as efficient agents to complex metals. They form chelate structures using the N, O, and S atoms located in their side chains as well as in their amino and carboxylate groups (75).

Amongst them, histidine is the most versatile amino acid that plays pivotal roles in protein interactions and predominantly coordinates with a majority of metals (76) Particularly, the His_6-tag sequence, present at the C- or N-terminus of a protein is commonly used in protein purification, called immobilized metal affinity chromatography (IMAC) (Figure 10) (77). During protein purification, metal ions (usually nickel) bind to the His_6 sequence of the protein (78) and then the protein is immobilized by chelation with a ligand (nitrilotriacetic acid (NTA)) bound to a solid matrix (79). Nitrilotriacetic acid, pyridine, bipyridine, and terpyridine have been widely used as ligands in protein purification (72). However, nitrilotriacetic acid (NTA) complexes with transition metal ions [Zn (II), Ni (II), or Cu (II)] coordinate mainly histidine (80). One molecule of NTA can form a coordination bond with two imidazole rings on adjacent histidine residues in a protein (81) and confers great advantages.

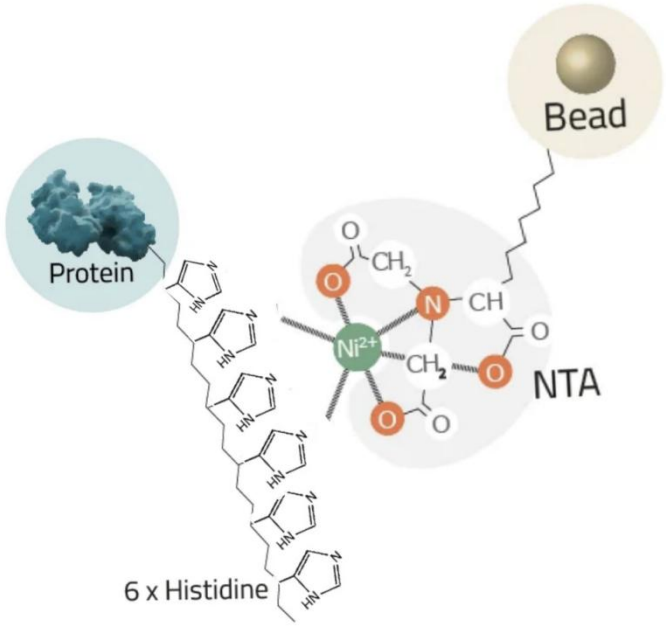

Figure 10: Schematic representation of the complex formed between the poly-histidine tag and a Ni-NTA support.

In the biomedical field, fluorescent probes have been modified with various NTA derivatives (mono-, di-, tri-, or tetra-NTA), in order to enhance the binding affinity of the His-tag with Ni^{2+}-NTA and provide improved properties for bioimaging applications (80).

1.5.2.1 Metal Complexes in Nanotechnology

The importance of metal-mediated interactions extends far beyond simple structural roles. They are associated with physiological activities ranging from nerve conduction, wound healing, antimicrobial activity, and cell adhesion. Conversely, they are also implicated in pathological conditions, like Alzheimer's and Parkinson's disease (20).

Recognizing the importance of metal chelation in natural processes, researchers have sought to emulate these interactions *in vitro* for myriad applications. One such strategy encompasses the synthesis of stable nanoparticles (NPs) for advanced applications. This approach exploits the capability of the peptides to efficiently coordinate metals to form stable nanoparticles (NPs) in situ through a "green process" (82) . The synergy between peptides and inorganic molecules offers considerable

advantages because the amino acids can control the shape, size, or crystallinity, altering the physical properties of the inorganic materials (83).

In nanotechnology, many metals participate in the formation of metallic nanoparticles. At the same time, chemically treatment can yield to metal oxide-based nanoparticles, examples of which include Copper oxides (CuO & Cu_2O), Iron oxide (Fe_2O_3), Aluminium oxide (Al_2O_3), Titanium oxide (TiO_2), Zinc oxide (ZnO) (84). Specifically, among them, zinc oxide (ZnO) and copper oxide (CuO) demonstrated remarkable compatibility with healthy cells within the body. The peptide - NPs complexes offer numerous advantages, including biocompatibility, versatility, and the ability to interface with biological systems, and they are suitable for utilization in fields such as cancer therapy, cosmetic formulations, and catalysts in industrial processes (85) . Focusing on the treatments, factors such as particle size, the duration of exposure time to the target cell, the metal content in the targeted cell, and their physicochemical characteristics play a crucial role in assessing the antimicrobial and anticancer outcomes.

Nevertheless, the mechanism of their activity is still unclear. It is suggested, for example, that the CuO NPs encompass the ability to generate Reactive Oxygen Species (ROS) upon interaction with bacterial cells. This contact with the bacterial membrane causes a decline in the bacteria's transmembrane electrochemical potential, leading to membrane disruption. Once Cu nanoparticles accumulate, they create pinholes on the cell surface, which cause leakage of intracellular components, allowing the Cu nanoparticles to penetrate the cell. The nanoparticles then release both free cuprous (Cu^+) and cupric (Cu^{2+}) ions, potentially disrupting the ROS balance and accelerating ROS production. In the presence of various reducing agents, such as ascorbic acid and superoxide ($O2^{\bullet-}$), the cupric ($Cu^{2+)}$ ions get reduced to cuprous (Cu^+) ions. This ionic transformation promotes and catalyzes the free radical reaction, converting hydrogen peroxide into hydroxyl radicals through the Haber-Weiss reactions.

Fenton Reaction	$O2^{\bullet-} + Cu^{2+} \rightarrow O2 + Cu^{+}$
	$Cu^{+} + H2O2 \rightarrow Cu^{2+} + OH^{-} + \mathbf{OH}^{\bullet}$
Haber-Weiss	$O2^{\bullet-} + H2O2 \rightarrow O2 + \mathbf{OH}^{\bullet} + OH^{-}$

These hydroxyl radicals induce fatal alterations in cells, leading to DNA and protein damage. Furthermore, Cu nanoparticles can interact with sulfhydryl groups of vital enzymes and proteins. For instance, protein tyrosine phosphatase, a crucial enzyme in cell metabolism, can be inhibited or even degraded due to this interaction (86).

A similar mechanism based on the production of reactive oxygen species (ROS) has been proposed for the ZnO NPs. Nonetheless, the destabilization of microbial membranes due to direct ZnO particle contact with cell walls, coupled with the inherent antimicrobial properties of Zn^{2+} ions released in aqueous environments, has also been proposed (87).

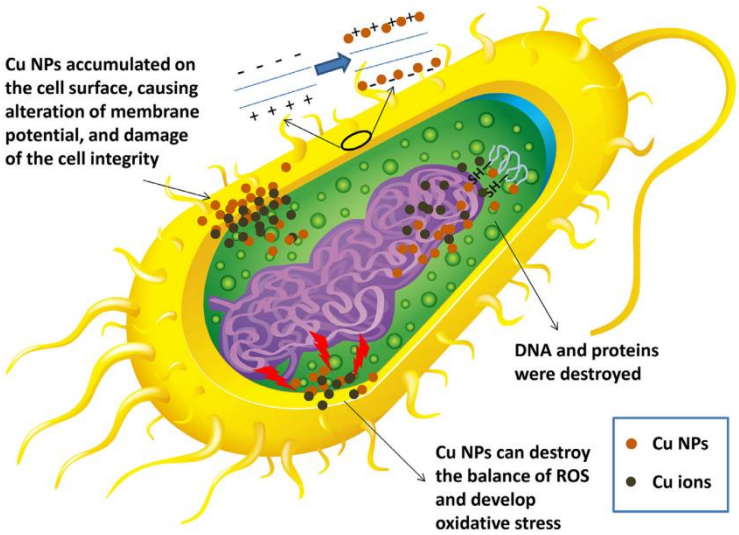

Figure 11: The antibacterial mechanism of copper nanoparticles (NPs) may be perceived as copper nanoparticles aggregating on the bacterial membrane, subsequently disrupting the integrity of the bacterial membrane. The copper nanoparticles release copper ions and trigger the production of reactive oxygen species (ROS), ultimately damaging DNA and proteins (86).

A similar mechanism for producing reactive oxygen species (ROS) has been proposed for ZnO NPs. However, increased zinc ion release in an aqueous environment or direct contact with ZnO can also destabilize the microbial membrane and lead to cell death (88,89).

1.5.3 pH-Responsive Materials

pH-Responsive materials have attracted considerable attention in the world of smart or stimulus-responsive materials due to their unique ability to undergo changes in their properties in response to changes in environmental pH. This ability is derived

from the presence of acidic or basic functional groups within these materials, which can either donate or accept protons depending on the conditions of the ambient pH.

One pivotal component that plays a vital role in the pH responsiveness of certain materials is the amino acid, histidine. Histidine is an essential polyprotic amino acid (90) with unique biochemical and physiological characteristics. It is essential for tissue growth and repair, facilitates the transport of metal elements like copper, and plays a crucial role in regulating the central nervous system (91).

In particular, the characteristic moiety of histidine is the imidazole side chain, which is composed of two tautomers (Nτ-H and Nπ-H) with different properties on its ring: one binds to hydrogen and donates a lone pair to the aromatic ring, while the other contributes only one electron to the aromatic ring, leaving a free lone pair (75).

Depending on the pH in natural systems, the free electron pair of nitrogen atoms in imidazole can coordinate with a wide variety of divalent transition metal ions (Zn, Ni, Cu, Fe, Co, Mn) via one or both of the deprotonated nitrogens (91). Histidine has a first pKa value of ≈ 6.5, which is close to physiological pH and therefore may serve either as general acid in the protonated form, either as a general base at the unprotonated form and bind metals (90) (Figure 12). The histidine residue can also serve to stabilize the folded structures of proteins (92). The previous literature shows that histidine dimer binds well with metal at the Nπ position. Nevertheless, metal cations can interact with both the carbonyl oxygen (C=O) portion of the carboxylic acid, which serves as an electron-rich site, and the nitrogen (Nπ) atom of the imidazole simultaneously (75).

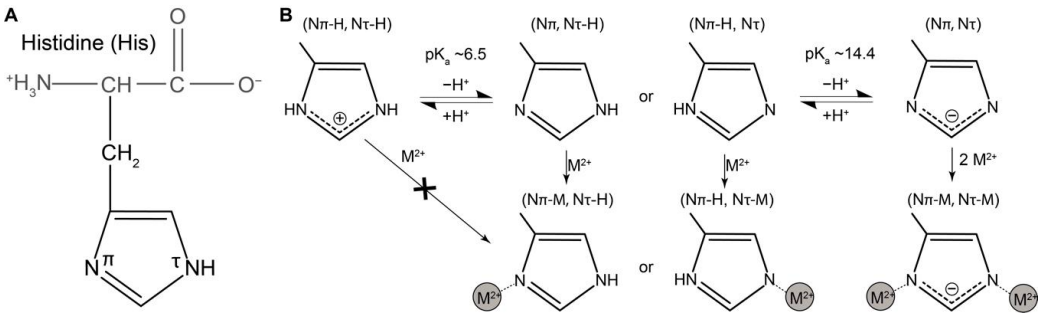

Figure 12: Histidine chemistry and metal binding. (A) Chemical structure of the amino acid histidine (His) under physiological conditions (pH ≈ 7.5). (B) Depending on pH and other

solution conditions, the histidine imidazole side chain can exist in a number of forms. Metal (M^{2+}) binding can only occur when a proton is lost from at least one nitrogen atom (91).

Also, the number of binding ligands, the configuration of the coordination bonding, and the metal–ligand binding affinities are all determined by the metal ions involved, and these factors influence the size, shape, and physicochemical characteristics of the resultant structures (91).

These different configurations significantly influence the role of the complexes, in both catalytic and mechanical conditions. For instance, X-ray crystallography has revealed that proteins containing histidyl binding sites typically exhibit a tetrahedral binding geometry with Zn (II), a square planar conformation with Cu (II), and an octahedral structure with Ni (II) (93,94).

The protonation-deprotonation dynamics of histidine residues highlight their key role in biomedical efforts, particularly in targeted drug delivery. Numerous studies have refined the successful formation of nanocarriers using histidine-bearing polymers, demonstrating their efficacy in releasing drugs, such as doxorubicin (DOX) into the acidic microenvironment of cancer cells (95,96).

Consequently, peptides containing histidine in nanoparticle systems can enhance pH-dependent drug release as well as the precision of drug release in cancer cells. These materials with the unique properties of histidine bring out a synergistic effect, opening up new avenues in materials science and offering the potential for innovative solutions in biomedical applications.

2. Materials and Methods

2.1 Peptide sequences

The peptides Fmoc-Phe-Phe-OH, RGDSGAITIGH and cyclo-(His-Phe)-OH were purchased by Bachem. The synthesis of the peptide sequence Fmoc-(Phe-His) was carried out by Dr. Georgios Landrou under the supervision of Professor Athanasios Coutsolelos at the University of Crete.

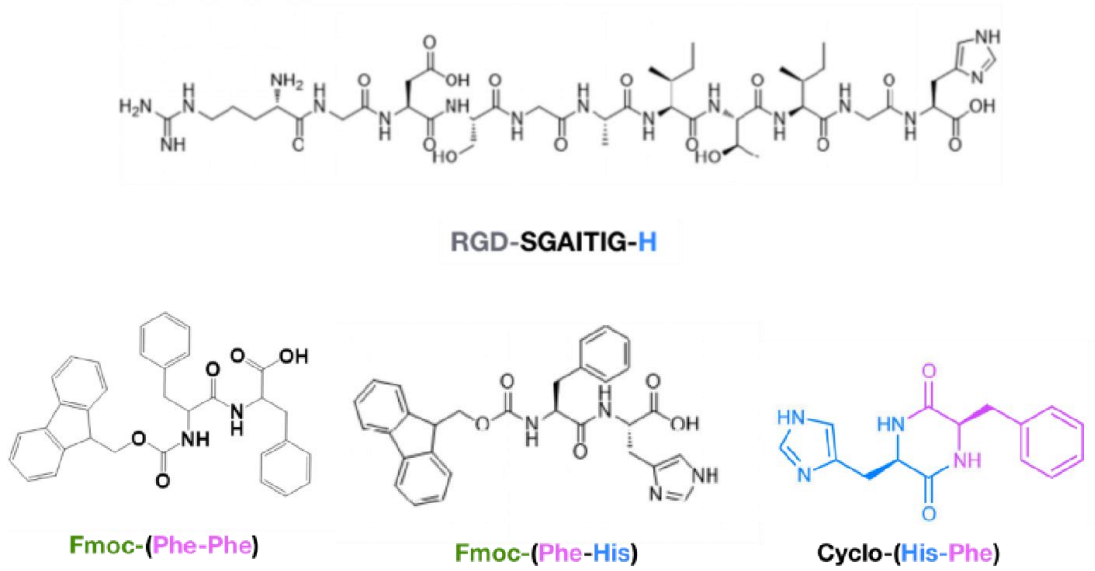

Figure 13: Structures of the peptide sequences that have been probed in this thesis.

2.2 Structural Characterization Methods

2.2.1 Field Emission Electron Microscopy (FE-SEM)

Field-Emission Scanning Electron Microscopy (FE-SEM) is an advanced imaging technique that provides valuable information about the elemental composition and topography of microstructures. This microscopy method was originally developed by Erwin Müller in 1936 (97) and it utilizes an electron gun, which emits a beam of electrons that are accelerated using high voltages ranging from a few kilovolts to tens of kilovolts. The beam is liberated from a tungsten filament, and it is focused and deflected using electromagnetic lenses, following a zig-zag scanning pattern. These primary electrons interact with the atoms on the surface of the sample, resulting in the emission of secondary electrons and other signals. The secondary electrons are collected by a detector, where they are converted into electrical signals. These signals allow the representation of surface topography at varying magnifications, ranging from low to extremely high levels (98).

FESEM microscopy offers additional advantages that make it a versatile tool for analysis. It allows the examination of smaller contamination spots at electron acceleration voltages suitable for energy dispersive spectroscopy (EDX). To observe samples using FESEM, they need to be conductive to the current. This conductivity

can be achieved by coating the samples with an extremely thin layer (1.5-3.0 nm) of a metal like gold or gold palladium. This coating process is typically carried out in a separate device. Additionally, the objects being analyzed must be capable of withstanding the high vacuum conditions and should not release water molecules or gases that could disrupt the vacuum environment.

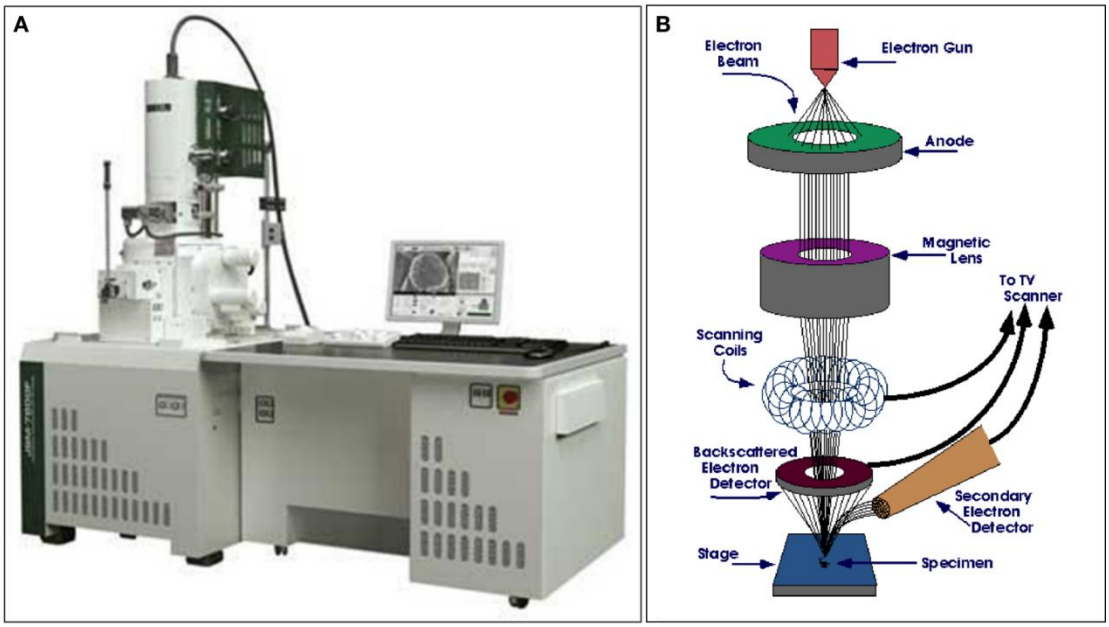

Figure 14: A) Field Emission Scanning Electron Microscope facility at University of Crete B) An illustrative diagram depicting its operational principle (99).

2.2.2 Critical Point Drying

Imaging a biological specimen using SEM or FESEM microscopy requires a specific preparation procedure. The biological samples need to be dried in order to be compatible with the vacuum in the microscope because the presence of water molecules will disturb the vacuum and additionally its evaporation with it could cause collapse or deformation of the structures under investigation (100) . In order to preserve sample morphology, they must undergo fixation, drying, and coating with a thin layer of heavy metal, called critical point drying method.

Since the critical point of water is 228,5 bar at 37,4 °C and it is not sufficiently miscible with CO_2, the samples are first treated in a suitable transitional fluid, such as ethyl alcohol and acetone, which are miscible with both water and CO_2.

Initially, the dehydration process of the samples includes the fixation of them with paraformaldehyde and then, in order serial rinses with alcohol 30%, 50%, 70, 90%, 100%.

After the samples are dehydrated, it follows the next step of the Critical Point Drying (CPD) (Figure 15). The ethanol in which the sample is suspended is replaced with liquid carbon dioxide (CO_2). The temperature rises, along with pressure, and the critical point of the carbon dioxide is reached. The critical point of CO_2 is 73,8 bar and 31°C and at this point, the liquid CO_2 changes to gas, without affecting the density of the specimen. Dehydrated samples were critical point dried with Baltec CPD 030.

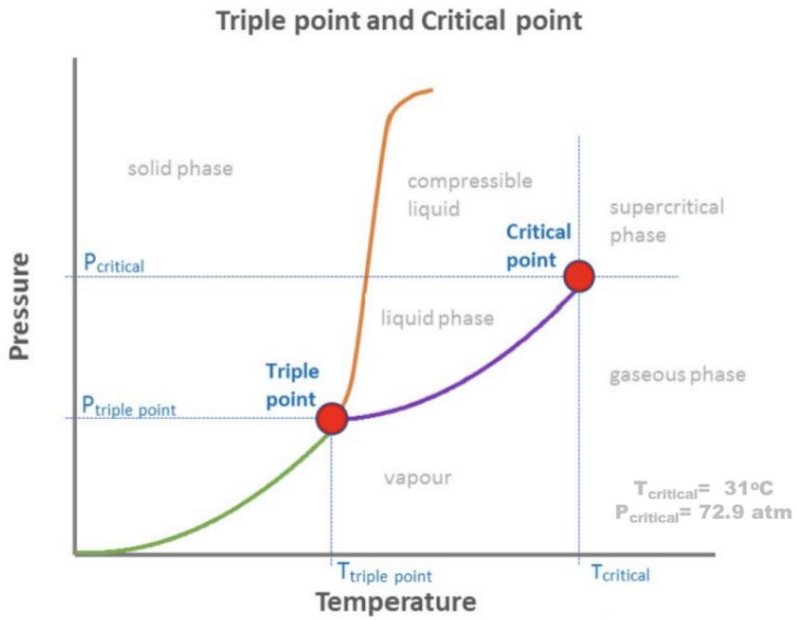

Figure 15: CO_2 phase diagram. At 73 atm and 31 °C the liquid and gas have the same density. Picture [source]

Alternatively, there is a method of chemical drying of biological samples for microscopic observation. The procedure of fixation and dehydration are the same as in the critical point drying. The difference is in the last stage after the 100% ethanol, where the sample is transferred to 100% Hexamethyldisilazane (HMDS) through a graded series of ethanol-HMDS mixtures.

Before the observation, air-dried or critical point-dried samples were rinsed in an argon atmosphere and subsequently gold sputtered with 10 nm gold (SCD 050 Sputter Coater, BAL-TEC AG, Liechtenstein).

2.2.3 Transmission Electron Microscopy (TEM)

Transmission Electron Microscopy (TEM) is a highly effective technique for imaging materials at the atomic resolution level. It originated from the development of the first electron microscope by Knoll & Ruska in 1931 (101) In modern times, TEM is extensively employed for studying various materials, including polymers, inorganic substances, and biological samples.

In TEM imaging, electrons are generated through thermionic emission from a filament located at the top of the microscope, typically made of tungsten or materials like Lanthanum Hexaboride (LaB_6). These electrons travel through a vacuum within the microscope column, and electromagnetic lenses are used to focus them into a narrow beam. The focused electron beam is then directed through the specimen under examination. After passing through the specimen, the electrons are collected on the other side, where they have increased energy, and guided to a fluorescent screen using electromagnetic lenses.

Sample preparation is a crucial step in TEM experiments, as different types of materials require specific techniques to make them thin, transparent, and electron-dense enough for TEM imaging. In the case of biological samples, they are typically transparent, and without staining, it would be challenging to differentiate different components within the sample. To address this issue, specific stains, also known as negative stains, can be applied. One such stain is uranyl acetate, a heavy metal compound that binds to biological samples. When used as a staining agent, uranyl acetate enhances the contrast between different regions within the sample, making it easier to visualize and analyze biological components under TEM. In the described experiment, the sample was prepared by depositing it on a copper grid covered with a thin film of formvar. The grid provided multiple observation areas, each with an approximate size of 60x60 μm. TEM employs electrons with high energy, usually between 30 to 2000 kV, to ensure deep electron penetration and exceptional spatial precision. Using these methods, one can attain a spatial resolution less than an angstrom, which allows for intricate imaging and examination of structures at the atomic level (102).

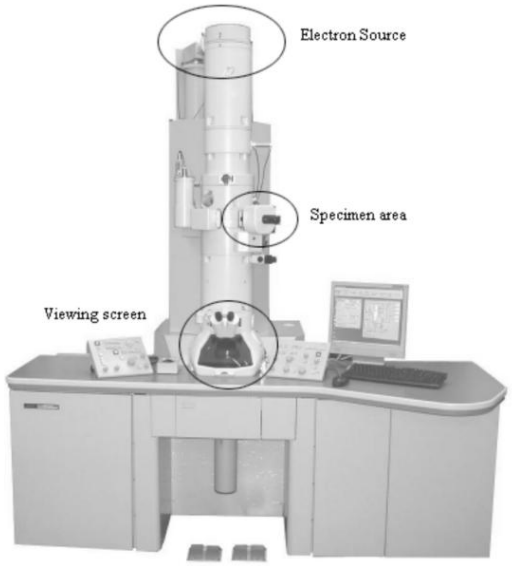

Figure 16: JEOL JEM-2100 Transmission Electron Microscope (JEOL).

2.2.4 Energy-Dispersive X-ray Spectroscopy (EDX)

Energy-Dispersive X-ray Spectroscopy (EDX) was utilized for elemental and compositional analysis in a specimen. It is based on an incident X-ray beam that interacts with the atomic structure of each element, producing distinct peaks in the X-ray spectrum (103).

In particular, the X-ray beam excites an electron in the inner shell of an atom, causing the electron to be ejected from its inner shell and leaving behind a positive electronic hole. Afterward, an electron from a higher-energy outer shell fills this vacancy, and the energy disparity between the two shells is emitted as an X-ray.

The emitted X-rays from the specimen can be detected and their number and energy analyzed using an energy-dispersive X-ray spectrometry (EDS) detector. Subsequently, the obtained signal is processed through a pulse processor and transmitted to an analyzer, typically linked to a computer. By correlating the distinctive energy levels of the X-rays with the atomic structure of the emitting elements, EDX can identify and determine the elemental composition of the specimen.

2.2.5 Congo Red Staining

Congo Red dye (CR) staining is a widely used method for detecting the presence of amyloid structures in protein aggregates. CR was discovered by chemist Paul Böttiger in 1883 during his attempts to synthesize a pH indicator.

In 1922, Bennhold found that CR could be utilized for the identification of amyloid structures both *in vivo* and *in vitro* (104). Molecular docking simulations have played a valuable role in understanding how Congo red (CR) binds to amyloid fibrils and protofibrils. These simulations have revealed that CR binds to specific sites that align parallel to the fibril axis but in an antiparallel orientation to the β-sheets within amyloid structures. The binding of CR to peptides and proteins occurs through a combination of hydrophobic and electrostatic interactions (38) . Notably, CR possesses the unique ability to intercalate vertically between the antiparallel β-sheets of amyloid fibrils. This intercalation results in a distinctive fluorescent yellow or green birefringence when observed under polarized light. The appearance of different colors as the polarizer or analyzer is rotated from the crossed position is due to a combination of light absorption and changes in birefringence. The interplay between these factors contributes to the characteristic optical properties of CR-stained amyloid structures, allowing for their identification and visualization. This property makes CR staining a simple and cost-effective diagnostic tool for the detection of amyloidosis. By observing the unique birefringent patterns, medical professionals can identify and confirm the presence of amyloid structures, aiding in the diagnosis and understanding of this pathological condition.

2.3 Chemical Characterization Techniques

2.3.1 UV-Vis Absorption Spectroscopy

Ultraviolet-visible (UV-Vis) spectroscopy is a valuable technique for characterizing nanomaterials by examining how they interact with light, including absorption and scattering phenomena (105) . Many molecules contain chromophores that can selectively absorb specific wavelengths of ultraviolet (UV) or visible light. UV-visible spectrometers are capable of assessing the light absorbance of a sample, either at a specific wavelength or by scanning a range within the spectrum. The UV region spans from 190 to 400 nm, while the visible region covers 400 to 800 nm.

The light source, consisting of a combination of tungsten/halogen and deuterium lamps, emits visible and near ultraviolet radiation within the range of 200 to 800 nm. The emitted light is focused onto a diffraction grating, which efficiently splits the incoming light into its component colors of varying wavelengths, similar to a prism.

The absorbance (A) of the sample is determined by Beer-Lambert law:

$$A = \varepsilon lc, \text{ where}$$

A = Absorbance, ε = Molar absorption coefficient ($M^{-1}cm^{-1}$), c = Molar concentration (M), l = optical path length (cm).

The Beer-Lambert law states that there is a linear relationship between the concentration and the absorbance of the solution, which enables the concentration of a solution to be calculated by measuring its absorbance.

2.3.2 Fourier-transform infrared spectroscopy (FT-IR)

Fourier Transform Infrared spectroscopy is a highly valuable technique for structural and compositional analysis, widely used in various scientific fields, including chemistry, materials science and pharmaceuticals (106) . It offers valuable insights into the chemical composition, structure, and bonding characteristics of a wide range of materials.

FTIR spectroscopy utilizes a Michelson interferometer to generate a beam of light consisting of multiple frequencies simultaneously. The Michelson interferometer in FTIR spectroscopy splits the incoming infrared radiation beam into two separate paths using a beam splitter. One path consists of the reference beam, while the other path involves passing the beam through the sample. After interacting with the sample, the amount of light absorbed by the sample is measured to construct an interferogram, which serves as the raw signal. To obtain a usable spectrum from the interferogram, a mathematical technique called Fourier transformation is applied. This transformation converts the interferogram from the time domain into the frequency domain. The functional groups within molecules exhibit characteristic vibrations (stretching or bending) when exposed to specific wavelengths of light and the FTIR spectrum represents the intensity of the vibrations expressed in cm^{-1}. The FTIR spectrum is unique for the analysed compounds and is known as the fingerprint region (107) .

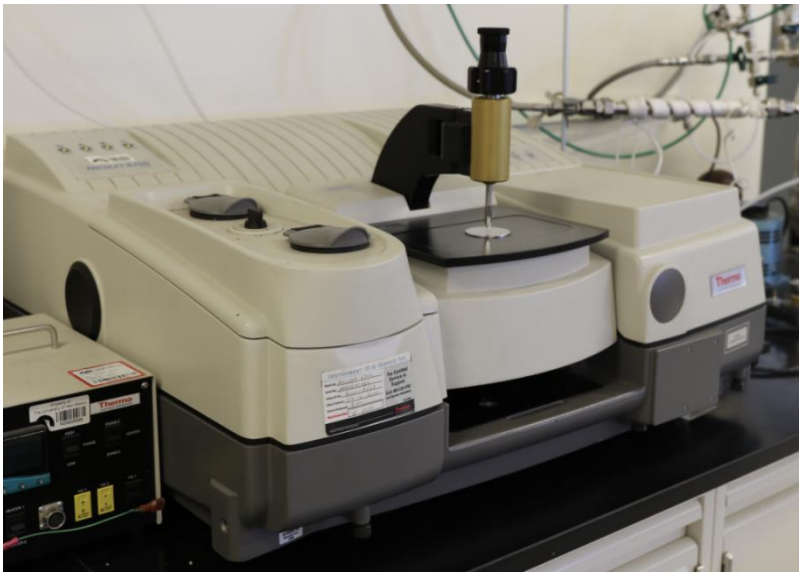

Figure 17: NICOLET 6700 FTIR Instrument [source]

2.4 Evaluation of Mechanical Properties

The mechanical characteristics of a material encompass those factors that impact its mechanical strength and its capacity to be shaped into the desired form. The Young's Modulus (or Elastic Modulus), often denoted as E or Y, is a measure of the stiffness of an elastic material. It describes the material's ability to resist deformation under an applied force. Specifically, it measures the ratio of stress (force per unit area) to strain (proportional deformation) in the linear elastic region of a material (108).

When a material reached a certain stress, the material will begin to deform. It is up to point where the materials structure is stretching and not deforming. However, if you stress the material more than this, the molecules or atoms inside will begin to deform and permanently change the material (109).

Mathematically, Young's modulus is defined as:

$E = \sigma / \varepsilon$, where

- σ is the applied stress (in Pascals, Pa or N/m^2)
- ε is the resulting strain (dimensionless)

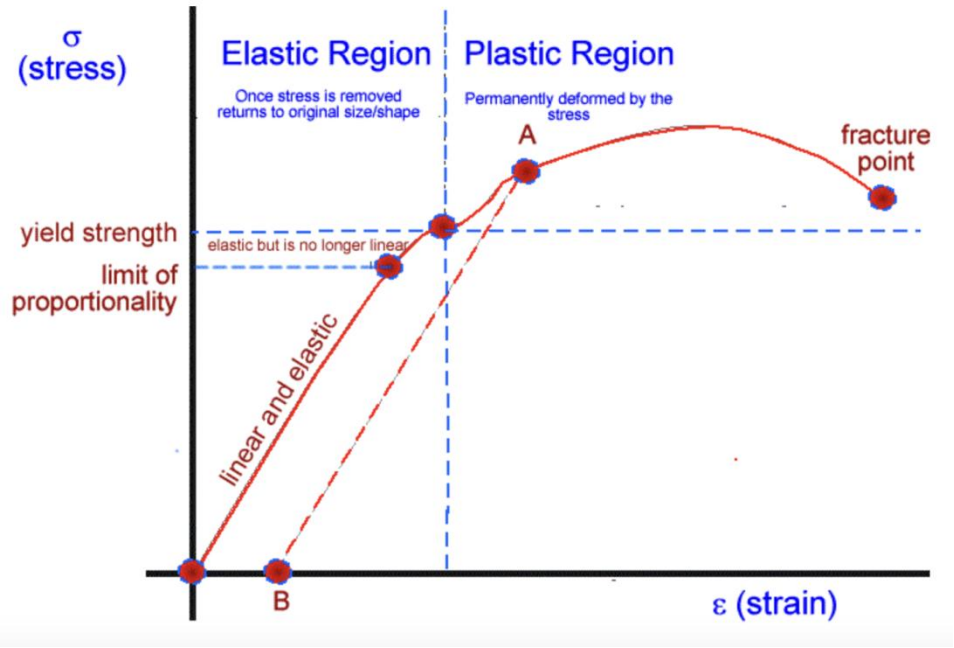

Figure 18: Young's modulus is the slope of the linear part of the stress-strain curve for a material under tension or compression [Source].

Chapter I

3. “Antimicrobial Potency of Fmoc-FF Dipeptide Hydrogels with encapsulated Porphyrin Chromophores: A Promising Alternative in antimicrobial resistance”

3.1 Introduction

Bacterial infections significantly complicate the wound healing processes, with threats stemming from external pathogens and bacteria from the skin’s native microbiota (110) Since the groundbreaking discovery of antibiotics in the 1940s, antimicrobial therapy has been one of the most outstanding achievements of modern medicine in addressing these infections. However, over the years excessive and often indistinct utilization of antibiotics, resulted in antimicrobial resistance (111) . This emerging crisis highlighted the need for innovative wound healing ways endowed with antimicrobial capabilities, steering scientific endeavors towards nanotechnological approaches.

Antimicrobial photodynamic inactivation (aPDI) is a potential alternative therapeutic strategy (112). The molecular mechanism of PDT targets cells or microbes (113,114) by using a photosensitizer, light with specific wavelengths, and molecular oxygen to initiate a reaction (115) . Upon light activation, these photosensitizers initiate a cascade wherein they catalyze peroxidase and oxidase reactions, absorb photons, and generate reactive oxygen species (ROS), mainly singlet oxygen (67) . The oxidative radicals occurring in the cellular environment disrupt of the cell membranes of Gram-positive and Gram-negative strains (70).

Porphyrins have gained interest as promising photosensitizers due to their unique photophysical, photochemical, and electrochemical properties for aPDI (116,117) . These photophysical and structural properties influence their efficiency against various pathogens such as viruses, bacteria, and protozoa (118). Structurally, porphyrins feature delocalized π electrons, a characteristic that can be tailored by

modifying peripheral substitutes, adjusting the central metal atom, or expanding the macrocycle's size (119).

Among these, cationic porphyrins stand out as a mainly researched PS category. They demonstrate comparable efficacy against Gram-positive bacteria as their neutral or anionic counterparts but possess superior efficacy against Gram-negative bacterial strains (120) . Their positive charge facilitates initial damage to the cell surface, promoting photosensitizer penetration. The aPDT efficiency of a photosensitizer depends on the quantity and spatial arrangement of its positive charges, with amphiphilic photosensitizers—characterized by their charge density and distribution—showing enhanced bacterial affinity (118) . Additionally, the porphyrin derivatives modified by metal atom in their core, especially Zn (II) (ZnPs), have gathered interest due to augmented interactions with cell membranes and their chemical stability (112).

Despite these advantages, many porphyrins macrocycles exhibit low solubility, low circulation half-life, and nonspecific selectivity challenges, limiting PTD efficiency (69) . To address this, the researchers have proposed nanoantimicrobials (NAMs), which offer improved delivery and protect the encapsulated drugs (121) . Among all the NAMs, hydrogels have arisen as a prime solution. Especially those that utilize self-assembling peptides like Fmoc-FF have shown great promise due to their structural versatility and compatibility with wound environments (122). The Fmoc-FF hydrogels support cell adhesion and proliferation; they exhibit the ability to encapsulate and release small molecules in a controlled manner (123) . They were, therefore, deemed suitable carriers for biomedical applications like controlled drug delivery (51).

In the present work, we propose the encapsulation of porphyrin derivatives into the self-assembled Fmoc-FF scaffold. Herein, we report one metal-free porphyrin, $H_2T(MePy)P(I_4)$, and its two metalloporphyrin complexes,Zn-$T(MePy)P(I_4)$ and, Zn-$T(MePy)P(Cl_4)$ shown in Figure 20. The metalloporphyrins vary in their counter ions; one carries iodine while the other carries chlorine, which improves their solubility. The choice of porphyrins stemmed from their distinctive characteristics, particularly their photostability, robust absorption capacity, high solubility in water and inherent

ability to produce reactive oxygen species. On the other hand, the Fmoc-protected diphenylalanine dipeptide, or Fmoc-FF, is renowned for forming highly stable hydrogels (122) . Initially, we focused on characterization of the formed peptide hydrogels using Field Emission Scanning Microscopy. Recognizing that encapsulated porphyrins might alter the scaffold Fmoc-FF's mechanical properties, we tested changes in their stiffness and release patterns. To further determine the therapeutic potential of these hydrogels, we tested their antimicrobial efficacy against Gram-positive *S. aureus* and Gram-negative *E. coli* bacteria. Through this work, we aim to find new treatments to overcome antimicrobial resistance and open the way for healing wounds.

3.2 Materials and Methods

3.2.1 Materials

Fmoc-Phe-Phe peptide was purchased from Bachem. The porphyrins $H_2T(MePy)P(I_4)$, $ZnTMePyP(I_4)$ and, $ZnTMePyP(Cl_4)$ were synthesized by Dr. Georgios Landrou under the supervision of Prof. Athanasios Coutsolelos (Department of Chemistry, UoC). The NIH3T3 cell line was cultured at 37 °C, 5% CO_2 in DMEM (Gibco) medium supplemented with 10% fetal bovine serum (Gibco) and 50 μg/mL gentamycin (Applichem). Thiazolyl blue tetrazolium bromide (MTT), isopropanol, dimethylsulfoxide (DMSO), ethanol, hexamethyldisilane (HMDS) and phosphate buffer saline (PBS) were purchased from Sigma-Aldrich. Live/Dead cytotoxicity assay for mammalian cells was purchased from Thermo Fisher Scientific (Waltham, Massachusettes, USA). Tissue culture (TC) inserts with a 0.4 μm pore size were purchased from Sarstedt (Nümbrecht, Germany).

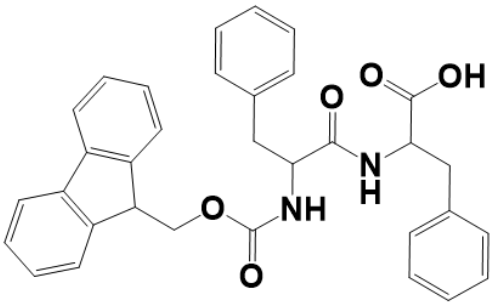

Fmoc FF

Figure 19: Chemical Structure of the peptide Fmoc-Phe-Phe.

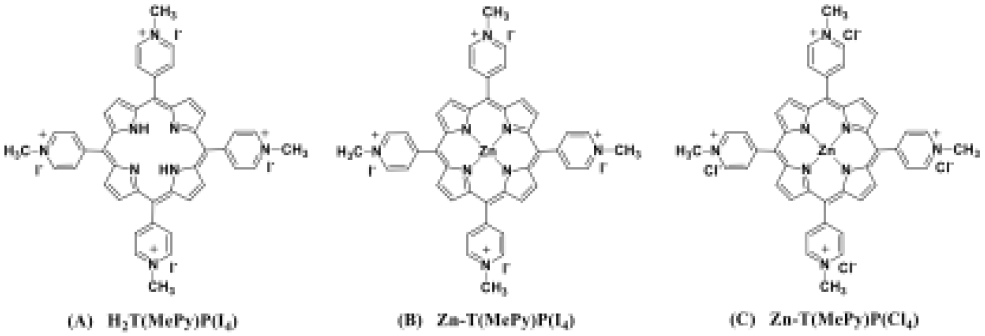

Figure 20: Chemical structures of the three porphyrin-based probes synthesized in this study - $H_2T(MePy)P(I_4)$, Zn-T(MePy)P(I_4) and, Zn-T(MePy)P(Cl_4).

3.2.2 Fabrication of Peptide Hydrogels

Peptide Fmoc-FF was prepared in a solution of Ethanol/H_2O with a ratio 25:75 v/v at a concentration of 5 mg/mL. The peptide powder was dissolved in 250 µL of ethanol under heating at 60 ^oC in a water bath and periodical sonication. 750 µL of sterilized water was added to the dissolved peptide solution to initiate the self-assembly process. The mixture was kept at room temperature for 1 h to allow sufficient time for the completion of self-assembly. For the fabrication of the hydrogels encapsulating the porphyrins, the same protocol was applied. Initially, the peptide powder was dissolved in ethano in 250 µL. Then, porphyrins were dissolved in 750 µL sterile distilled water (final concentration of 310 µM). The ratio of peptide-to-porphyrin was 30 to 1. Finally, the porphyrin solution was mixed with the dissolved peptide solution with smooth pipetting. The self-assembly into fibrils started instantaneously. The mixture was placed at room temperature for 1h to allow the completion of the self-assembly process.

3.2.3 Field-Emission Scanning Electron Microscopy (FE-SEM)

The hydrogel morphology was observed by using Field Emission-SEM (FESEM). Samples for FE-SEM analysis were prepared by depositing 10 μL from each self-assembled hydrogel on a 12 mm cover glass. The sample was left to air-dry overnight. Dried samples were sputter-coated with a 10 nm thick layer of Au (Baltec SCD 050) and observed directly. FESEM experiments were performed using a JEOL JSM 7000F operating at 15 kV.

3.2.4 Mechanical characterization of the scaffolds

Compression testing was conducted by PhD candidate Varvara Platania at Prof. Maria Chatzinikolaidou's laboratory utilizing a compression and tensile strength test unit (UniVert, CellScale, Waterloo, Canada) with a maximum cell load of 50 N. The Young modulus of the scaffolds was measured at velocity of 15 mm/s. In addition, 3 measurements were taken from each scaffold composition. Young modulus at 5–20% was calculated using the following formula: (1) Young modulus:F·LA·ΔL where F is the perpendicular force applied to the surface of the scaffolds, A is the surface, ΔL is the height strain of the scaffolds after the force application and L is the initial height.

3.2.5 Release Evaluation

The hydrogels were prepared as described above. 500 μL of the prepared gels incubated into cuvettes for 24 h at room temperature. Next day, 1 ml of water was placed on top of the gel at 37 ^{o}C and the water was replaced every 6 h hours. The amount of porphyrin released from the hydrogels in the water was quantified using UV–Vis spectrophotometry (UV-1700 PharmaSpec, Shimazdu) measuring the absorption at wavelength of 519 nm for the $H_2T(MePy)P(I_4)$ and at 564 nm for the metalloporphyrins Zn-T(MePy)P(I_4) and Zn-T(MePy)P(Cl_4) porphyrins, respectively. All porphyrins release data were averaged over three measurements. The cumulative drug release was calculated as follows:

$$\text{Cumulative Drug release (\%)} = \frac{drug\ released\ at\ time\ t\ + \text{drug released at previous time}}{\text{initial amount of drug encapsulated in gel}} * 100\%$$

3.2.6 MTT Cell Proliferation Assay

NIH3T3 cells with concentrations of 6×10^4 cells/well were cultured in a 24-well plate for 24 h. 100 μL of Fmoc-FF hydrogel was added into a hanging basket with a filter size of 0.4 μm and it was attached onto the well. 1 mL of DMEM medium was added into the well to ensure sufficient contact with the bottom of the hanging basket. Cells that were not treated with the hydrogels served as control. The well plate with the inserts was incubated for 48 h at 37 ^{o}C. Cell proliferation was measured with the MTT assay. After incubation for 48 h incubation, the careful removal of the medium was followed by the addition of 300 μL of fresh medium and 30 μL of MTT (5 mg/mL) dissolved in PBS 1X. The cells were incubated for 4 h to allow the development of the purple formazan products and the MTT/culture medium was substituted with 300 μL of an isopropanol: DMSO 1:1 solution. The formazan crystals were allowed to dissolve for 15 min at 37 °C. The absorbance was measured at 570 nm in a Synergy HTX BioTEK Plate Reader. Cytotoxicity of the peptide hydrogels encapsulating metalloporphyrins, was not examined with this method since the porphyrins have an inherent absorbance that may interfere with the MTT measuring absorbance.

3.2.7 Fixation and dehydration of cells attached on peptide hydrogel scaffolds

Peptide hydrogels without and with encapsulated metalloporphyrins were added at a quantity of 50 μL on top of a 10 mm circular cover glass which was placed inside a 24-well plate. The hydrogel material was spread to cover the whole area of the glass. $6x10^4$ of NIH3T3 cells were added onto the hydrogel. The plates were incubated at 37 ^{o}C for 48 h. After 48 h the medium was removed and the attached cells were washed twice with 300 μL of PBS. Cell fixation was performed by adding 300μL of 4% paraformaldehyde to each well for 15 min. Parafolmadehyde was removed and the cells were washed again twice with 300 μL of PBS. The cells were further incubated for 5min each time with increasing concentrations of ethanol (30%, 50%, 70%, 90%, 100% dry ethanol) in order to dehydrate the samples. Finally, 200 μL of Hexamethyldisilazide (HMDS) was added on each well and was left to evaporate overnight. The cover glass was removed with a tweezer and placed on top of a carbon tape for further process and observation with FESEM.

3.2.8 Live/Dead cytotoxicity assay

50 μL of the peptide hydrogels were added at the bottom of each well of a 24-well plate. $1x10^5$ NIH3T3 cells were added on top of the solidified hydrogel and the plate was incubated for 24 h at 37 ^oC. The staining solution was prepared by adding 5 μL calcein AM and 20 μL ethidium homodimer-1 to 10 mL of PBS 1X. After the incubation period, the medium was removed and 200 μL of the staining solution was added directly to cells. For efficient staining, the cells were left at RT for 30 minutes. The stained live and dead cells were observed with a fluorescent microscope by using a 494/517 nm filter for Calcein AM for live cells and a 528/617 nm filter for Ethidium homodimer-1 for the dead cells.

3.2.9 Antimicrobial Activity

The samples were prepared as described above into 1 mL syringes. One colony of *E. coli* and *S. aureus* were left to grow in 5 mL Luria Broth at 37 ^oC for 16 hours. Then, 500 μL of the pre-culture was transferred into 50 mL of Luria Broth (LB) and incubated in a shaker (200 rpm) at 37 ^oC until the mid-log phase ($O.D_{600}$= 0.1). Then, the *E. coli* and *S. aureus* cells were diluted 6 times and 600 μL transferred into Eppendorf tubes (2 ml). 100 μL of the prepared gels of Fmoc-FF, Fmoc-FF with $H_2T(MePy)P(I_4)$, Fmoc-FF with $ZnTMePyP(I_4)$, Fmoc-FF with $ZnTMePyP(Cl_4)$ transferred into the tubes with the *E. coli* and *S. aureus*. The samples were incubated for 5 h at 37 ^oC and then, irradiated under the visible light lamp (LED 40W 230V) for one hour under agitation at 100 rpm. Also, samples were prepared and incubated for 6 h at 37 ^oC, without light irradiation. As negative control was taken bacterial strain in LB Broth. After 6 hours, the optical density at 600 nm was measured. As a reference sample was used the LB broth without cells. Next, 100 μL were withdrawn from negative control and the encapsulated gel samples and were plated on Luria-agar plates after serial dilutions. The plates were incubated at 37 °C for 12-16 h, and bacterial colonies were counted to calculate colony forming units per milliliter (CFU/mL).

3.2.10 Statistical analysis

Statistical analysis was performed using ANOVA t-test in the GraphPad Prism version 8.3 software to evaluate the significance of the differences among various scaffold compositions and the control. A p-value (*) <0.05 was considered significant, **p < 0.01, ***p < 0.001, ****p < 0.0001, ns denotes a statistically non-significant difference. Results are presented as mean ± SD. The samples were prepared in triplicates, and the experiment was repeated three independent times.

3.3 Results

3.3.1 Morphological Characterization

The Fmoc-FF peptide mixed with porphyrins rapidly self-assembled into hydrogels of fibrillar morphology. The peptide powder after being dissolved in ethanol solution and heat-treated, is mixed with an aqueous solution of porphyrins. The gel formation happens instantaneously within a few seconds and it is observed by the transition from a clear to a hazy viscous solution and later transits again to a clear solution indicating the completion of the self-assembly. When the hydrogel formation is complete, the vials containing the metallo-porphyrin loaded hydrogels are turned upside down to evaluate the stability and rigidity of the hydrogels. As depicted in Figures 21A and 22A and 23A, the hydrogels are very stable and they remain at the bottom of the vial.

To further evaluate the viscosity of the hydrogels, a portion of a non-self-assembled gel mixture was transferred into a 1 ml syringe. The peptide-porphyrin mixture was left in the syringe to self-assemble into a clear hydrogel and the end of the syringe was removed. The hydrogel was pushed out onto a microscopy slide and the stability of the hydrogel was observed over time. It was concluded that the viscoelastic properties of the hydrogel are excellent and the cylindrical formation of the hydrogel is kept intact (Figure 21C and 22C and 23C).

Moreover, the fibrillar structure of the hydrogels was confirmed by scanning electron microscopy (FESEM) observations. The hydrogels comprise a thick network of fibrils with an approximate width of 10 nm for one fibril, which increases when additional fibrils are stacked together. As the figures show, the metal free porphyrin has dark

purple colour, whereas those combined with metals show different colors based on the particular metal ions they contain (124).

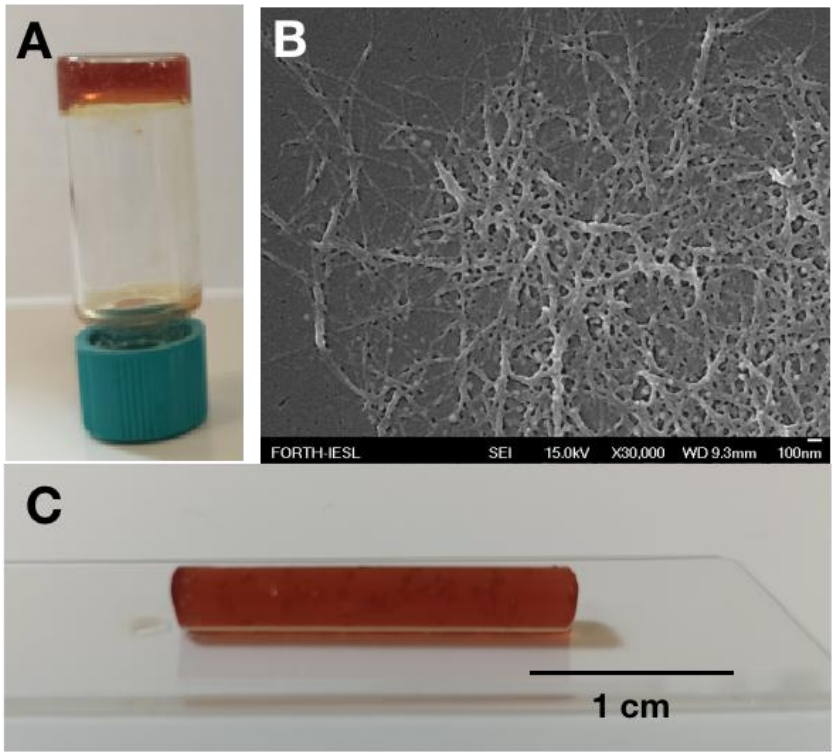

Figure 21: Fmoc-FF hydrogel encapsulating the TMePyP(H_2)(I_4) porphyrin. The hydrogel in a glass vial is placed upside down. B) Fibrillar formation as observed by FESEM (scale-bar:100nm). C) Fmoc-FF with H_2TMePyP(I_4) hydrogel shape stability after being extruded from a syringe.

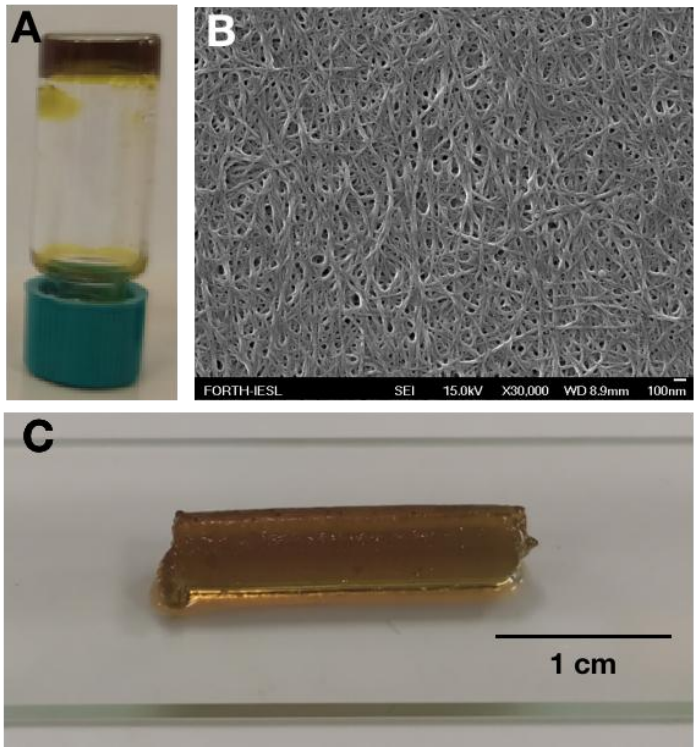

Figure 22: Fmoc-FF hydrogel encapsulating the Zn-T(MePy)P(Cl_4) metallo-porphyrin. A) The hydrogel in a glass vial is placed upside down. B) Fibrillar formation as observed by FESEM (Scale-bar: 100 nm). C) Fmoc-FF-Zn-T(MePy)P(Cl_4) hydrogel shape stability after being extruded from a syringe.

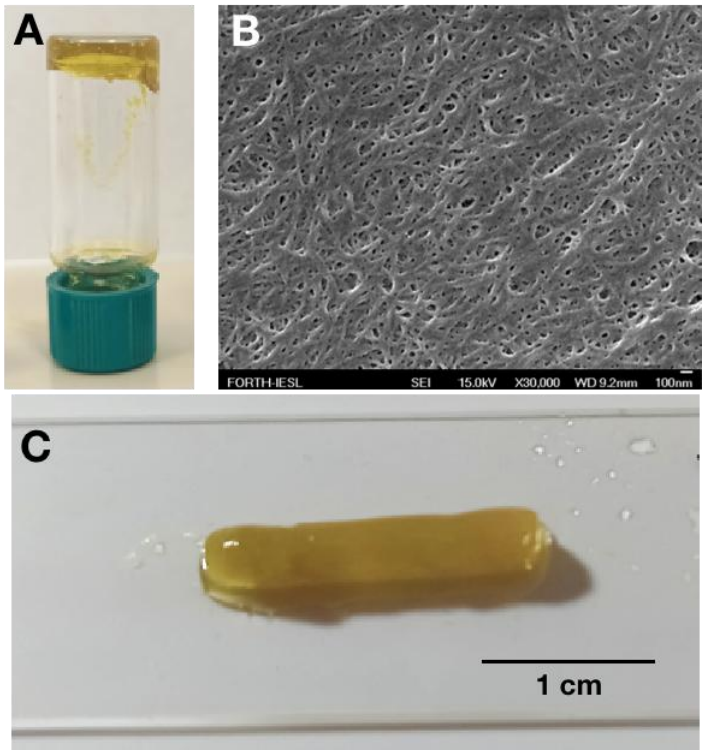

Figure 23: Fmoc-FF hydrogel encapsulating the Zn-T(MePy)P(I_4) metallo-porphyrin. A) The hydrogel in a glass vial is placed upside down. B) Fibrillar formation as observed by FESEM

(Scale-bar: 100 nm). C) Fmoc-FF-Zn-T(MePy)P(I_4) hydrogel shape stability after being extruded from a syringe.

3.3.2 Evaluation of hydrogel mechanical properties

In the field of medical device design, the stiffness of hydrogels plays a crucial role. To assess this characteristic, researchers often employ Young modulus measurements obtained through uniaxial compression or tensile tess (125,126). The Young modulus provides insight into the material ability to resist deformation under stress. Native soft tissues and organs generally exhibit Young modulus values ranging from 0.1 to 1 MPa (127).

The hydrogels made from Fmoc-FF (control) exhibited a Young modulus value of 9.6 kPa, indicating mechanically stable structures. The Fmoc-FF-Zn-T(MePy)P(I_4) hydrogels displayed a similar Young modulus value of 9.5 kPa. The Fmoc-FF-H_2-T(MePyP(I_4) hydrogel demonstrated a significantly lower Young modulus of 2.3 kPa compared to the Fmoc-FF control. These findings suggest that the incorporation of Zn instead of H_2T(MePy)P(I_4) had a substantial impact on the stiffness of the hydrogel, resulting in a stronger material compared to the H_2-derivative. The Fmoc-FF-Zn-T(MePy)P(Cl_4) hydrogel showed a Young modulus value of 6.6 kPa, which was not significantly different from the control (Figure 24).

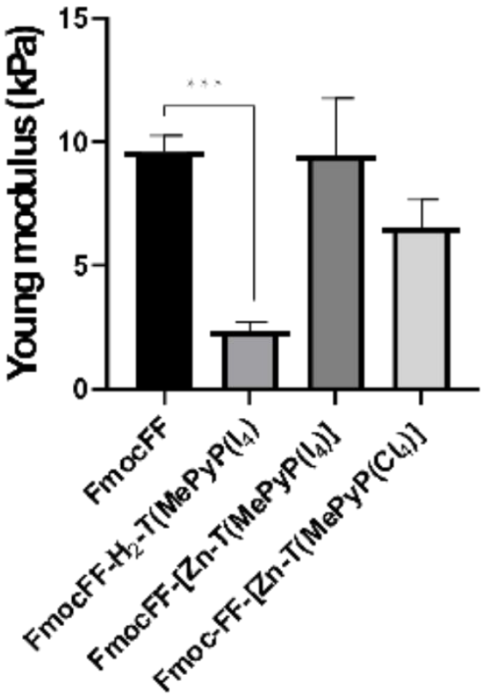

Figure 24: Evaluation of the elastic modulus of the scaffolds at 5–20% strain, at 15 mm/s velocity. Each bar represents the mean ± SD of triplicates (*p < 0.05, **p < 0.01, ***p < 0.001, ****p < 0.0001; ns denotes a statistically non-significant difference).

3.3.3 Evaluation of release properties

The release rate of the $H_2T(MePy)P(I_4)$, Zn-T(MePy)P(I_4), and Zn-T(MePy)P(Cl_4) porphyrins, which were encapsulated within the Fmoc-FF hydrogel scaffolds, was studied at the physiological temperature of 37 °C. In all examined cases, there has been an initial release burst of porphyrin derivatives during the first two hours, followed by a gradual release. The initial burst is attributed to the rapid hydrogel swelling which favors the diffusion of porphyrin. Focusing first on the Fmoc-FF hydrogel scaffold, we observed that the release rate of the the $H_2T(MePy)P(I_4)$ and Zn-T(MePy)P(Cl_4) porphyrins was about 8% being released within 24 h that corresponds to 20 and 25 μM respectively. Interestingly, the increased release of 13% of the Zn-T(MePy)P(I_4) correlates with 41 μM.

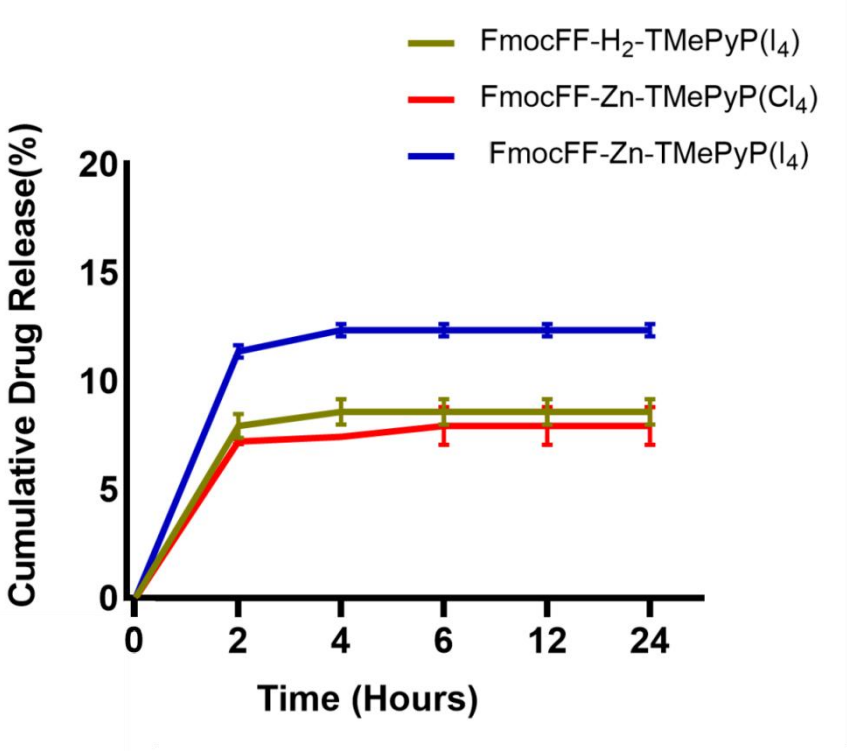

Figure 25: Cumulative release (%) of the $H_2T(MePy)P(I_4)$, Zn-T(MePy)P(I_4) and Zn-T(MePy)P(Cl_4) porphyrins from the Fmoc-FF scaffold at 37 °C.

3.3.4 Cytotoxicity Test

For a hydrogel to be suitable for therapeutic applications, it's imperative that it remains non-toxic to mammalian cells. Indeed, the peptide hydrogels encapsulating porphyrins are not toxic to mammalian cells. The cytotoxicity of the Fmoc-FF loaded with porphyrins was tested for their biocompatibility with mammalian cell lines and the subsequent capability of being used as therapeutic agents. Initially, the cytotoxicity of the peptide hydrogel Fmoc-FF without any loaded porphyrin was tested with the MTT assay in the NIH3T3 mouse skin fibroblast cell line. There are various studies referring to the absence of cytotoxicity of the peptide Fmoc-FF (128). In our study, it was important to evaluate whether the combination of the solvents used for dissolving the peptide powder and for the self-assembly of the fibrillar hydrogel, provide a safe and non-cytotoxic combination.

The Fmoc-FF hydrogels were formed inside a TC insert and were placed on top of a 24-well plate, where NIH3T3 cells were cultivated for 24h. The gel was in indirect contact with the cells through the media buffer, as depicted in Figure 26. This method is applied in order to evaluate whether the contents released from the hydrogels are toxic to the cells. The hydrogels were incubated with this setup for 48 h at 37 ^{o}C, showing no cytotoxic action to the fibroblast cell line (Figure 26B).

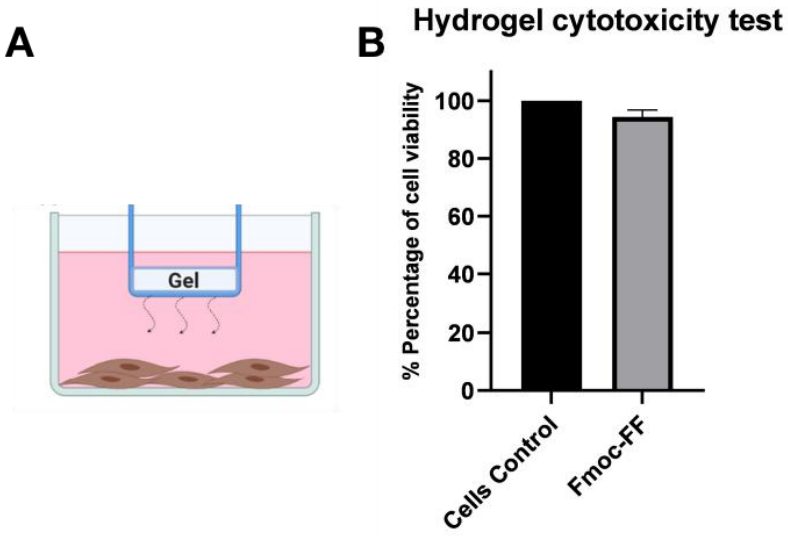

Figure 26: A) Experimental setup for the cytotoxic evaluation of the hydrogels through an indirect contact with the cells. 100 μL of either Fmoc-FF was placed into a TC insert. The hydrogel was in contact with the cell media through the 0.4 μm porous membrane of the insert. NIH3T3 fibroblasts were previously incubated for 24 h at 37 ^{o}C at the bottom of the well. B) MTT cytotoxicity assay results.

On a more direct approach, Fmoc-FF hydrogel encapsulating the $H_2T(MePy)P(I_4)$ porphyrin was added at the bottom of a 24-well plate. NIH3T3 fibroblasts were added on top and the samples were incubated at 37 ^oC for 48h to evaluate the cell proliferation on the hydrogels (Figure 27A). After incubation, the samples were fixed with parafolmaldehyde, dehydrated and placed for FESEM observation. It is concluded from the pictures obtained that hydrogels are biocompatible and allow cell proliferation. (Figure 27B1). Starting from pictures with lower to higher magnification it is obvious that the hydrogels provide a biocompatible environment and cells are multiplying while being able to attach and spread on top of the hydrogel (Figure 27B2). At higher magnifications of 1 μm-100 nm, the thick and fibrillar network of the hydrogel that acts as a scaffold for the fibroblast cells can be observed (Figure 27B3 and 27B4). The same experiment was performed for all the combinations of the metallo-porphyrin loaded hydrogels, resulting in a similar outcome (results not shown).

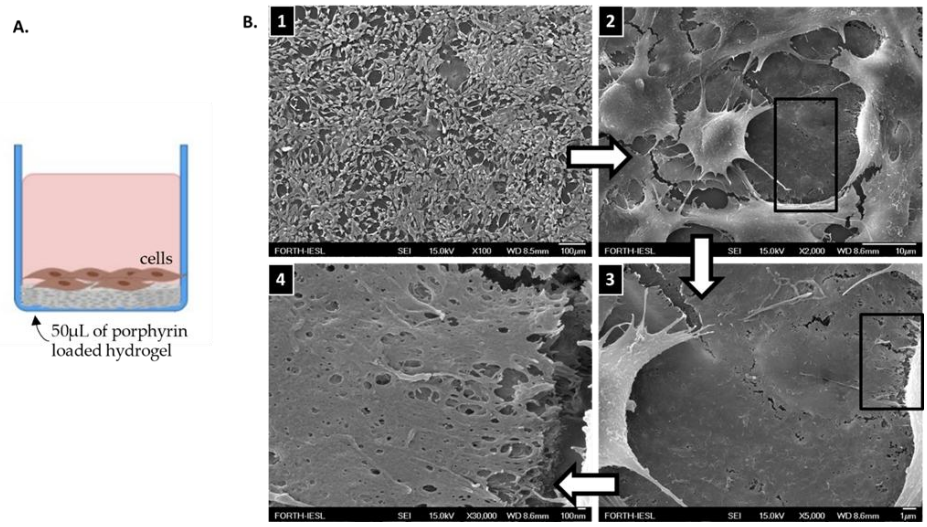

Figure 27: A) Experimental setup of the direct method of testing the biocompatibility of the metallo-porphyrin loaded hydrogels. A portion of **$H_2T(MePy)P(I_4)$** loaded Fmoc-FF hydrogel was added at the bottom of a 24-well plate and cells were added on top for a 48 h incubation. B) FESEM observations of the cell proliferation on top of the porphyrin loaded hydrogels. The same area is scanned with increased magnification. The black rectangles indicate the area that was further magnified. Scale bars for the pictures B1: 100 μm, B2: 10 μm, B3: 1μm, B4: 100 nm.

The Live/Dead cytotoxicity test was also employed to test the peptide hydrogel biocompatibility. A portion of the self-assembled peptide hydrogel was added into a 24-well plate which already contained attached NIH3T3 cells (Figure 28A). After a

24 h incubation, the cells were stained with calcein-green to detect the alive cells and with ethidium homodimer-1 to detect the dead cells. Results confirm the non-cytotoxicity of the peptide hydrogels since the vast majority of the cells produced an intense green color when the filter of calcein was used (alive cells) in comparison to the faint red color produced when the Ethidium homodimer-I filter was used (Figure 28B).

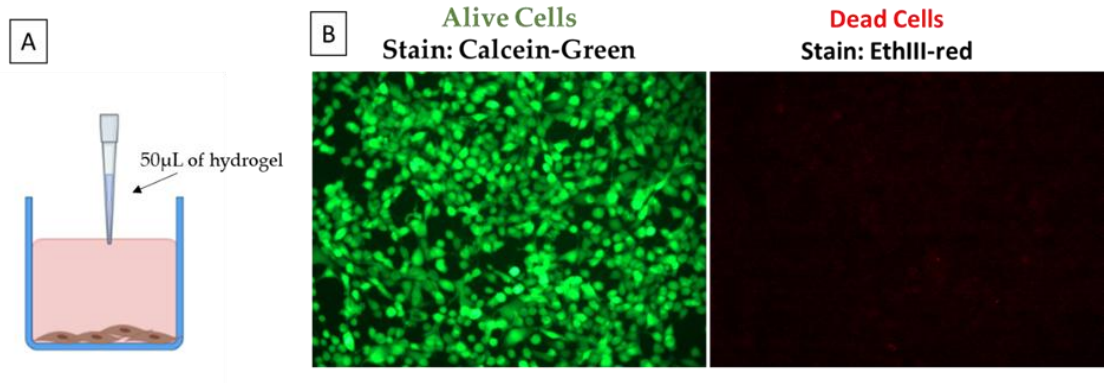

Figure 28: A: Experimental setup for the Live/Dead cytotoxicity assay. The peptide hydrogel was directly added to pre-incubated NIH3T3 cells. B) Cell-Hydrogel samples were stained and observed under a fluorescence microscope.Left: Exc 494/Em517nm (green) for the Calcein-Green filter which detects alive cells and Right: 528/617 nm filter for Ethidium homodimer-1 for the dead cells.

3.3.5 Antibacterial photodynamic activity *in vitro*

The efficiency of the antimicrobial system is based on its higher antimicrobial activity, along with low cytotoxicity. Demonstrating the negligible cytotoxic impact of all the formed Fmoc-FF hydrogels, our investigations shifted to examining *in vitro* the antibacterial effects of the $H_2T(MePy)P(I_4)$, Zn-$T(MePy)P(I_4)$, and Zn-$T(MePy)P(Cl_4)$ porphyrins against *E. coli* and *S. aureus,* facilitated by the light activation.

We observed that the peptide alone (i.e., without encapsulated porphyrins - hence serving as control group), once exposed to *E. coli* cultures, caused significant inhibition to the bacterial survival with and without light irradiation. In particular, the sole Fmoc-FF peptide reduced the surviving population by 30%, without light irradiation. Exposure to visible LED light (40 W 230V, 1 hour) yielded a further reduction of around 13%, strengthening the observation that the Fmoc-protected dipeptide has a significant effect on bacterial survival.

The encapsulated porphyrins $H_2T(MePy)P(I_4)$, Zn-$T(MePy)P(I_4)$, and Zn-$T(MePy)P(Cl_4)$ into the Fmoc-FF scaffold reduced the survival rate to 50 %, in the dark. In comparison, the $H_2T(MePy)P(I_4)$ porphyrin showed a further decrease of 9 %, under visible light. Similarly, the metalloporphyrin Zn-$T(MePyP(Cl_4)$ further reduced the survival rate of *E. coli* by an additional 12%. The similarly mild effect of the porphyrins $H_2T(MePy)P(I_4)$ and Zn-$T(MePy)P(Cl_4)$ into the Fmoc-FF is explained by the fact that they followed the same release kinetics, according to which a large fraction remains trapped in the hydrogel. Interestingly, the additional ~5% porphyrin release by Zn-$T(MePyP(I_4)$, (with respect to the other two porphyrins; Figure 25) is reflected in an additional 15% reduction in survival rate.

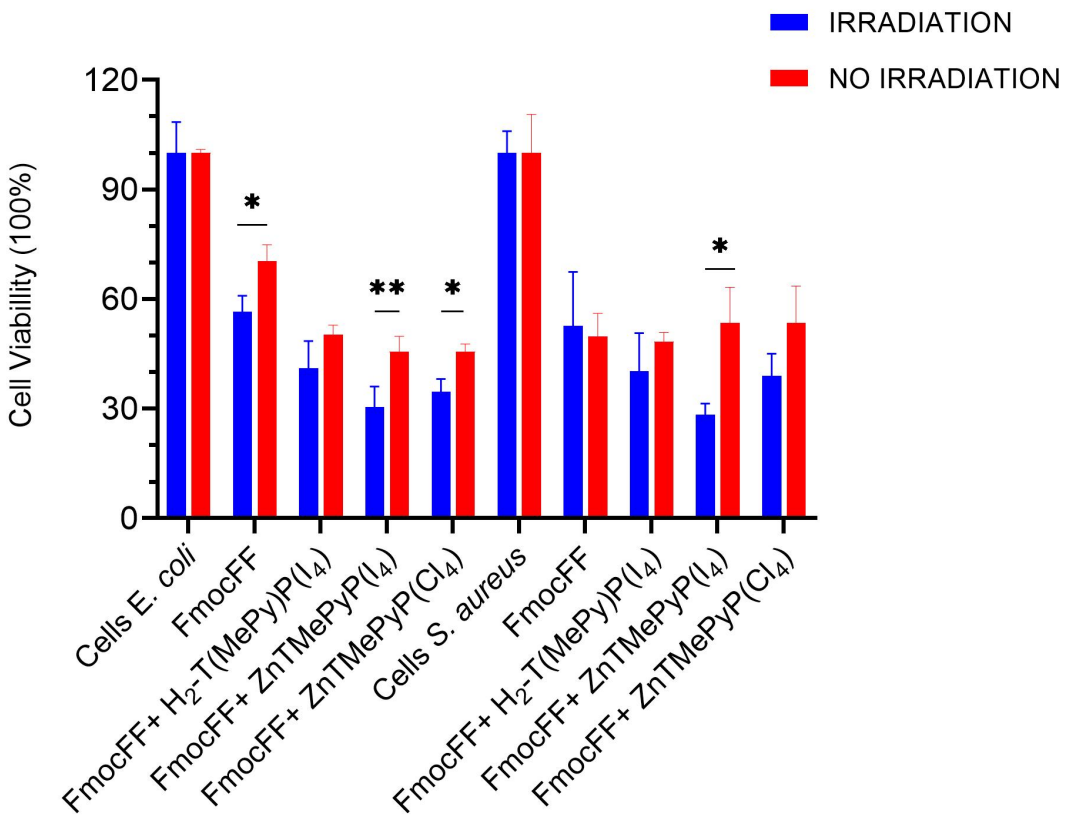

Figure 29: Diagram of the cell viability of *E.coli* and *S. aureus* incubated with the Fmod-FF hydrogel and the Fmoc-FF with encapsulated porphyrins H_2-T(MePy)P(I_4), Zn-T(MePy)P(I_4) and Zn-T(MePy)P(Cl_4), with and without light irradiation. *p≤0.05, **p≤0.01, ***p ≤0.001, ****p<0.0001. Two-way ANOVA. The experiments were carried out 3 times in triplicates.

In experiments similar to those conducted with *E. coli,* the peptide Fmoc-FF by itself led to a significant 50 % reduction in *S. aureus* survival, both with and without light exposure. When *S. aureus* cells were treated with the Fmoc-FF scaffold encapsulating the $H_2T(MePy)P(I_4)$ porphyrin, a comparable 45-50% decrease in survival was noted,

regardless of light conditions. These findings suggest that the modest amount of the $H_2T(MePy)P(I_4)$ porphyrin released into the medium does not significantly amplify its activity upon light exposure and exhibits similar efficacy against both microbial strains.

Interestingly, Zn-$T(MePy)P(Cl_4)$ reduced the survival rate to 50 % in the dark, mirroring the effect of the Fmoc-FF peptide alone. When exposed to light, there was an enhanced reduction compared to the simple porphyrin $H_2T(MePy)P(I_4)$. Given that the release amount of the porphyrin remains consistent, the superior efficacy of the zinc-centered porphyrin becomes evident. However, its overall effect on *S. aureus* remains limited. Notably, the additional ~5 % release of Zn-$T(MePy)P(I_4)$ relative to the other two porphyrins (as depicted in Figure 29) corresponds to the 35% survival rate observed for *S. aureus*.

3.4 Discussion

Antimicrobial resistance poses a significant global health risk, due to the inappropriate usage of antibiotics (129) . This work sought to engineer a multi-functional gel combining antimicrobial and wound-healing properties.

In particular, our research focused on the encapsulation of porphyrins into peptide hydrogels to impart them with light responsiveness. We selected the Fmoc-FF dipeptide as a scaffold for its biocompatibility, and the porphyrin $H_2T(MePy)P(I_4)$ and its metallo analogs as photosensitizers.

Initially, the Fmoc-FF peptide was combined with porphyrin derivatives and the experiments confirmed instantaneous self-assembly into hydrogels. It is well-known that the encapsulation of chromophores influences the self-assembly process of the peptides, potentially affecting the final hydrogel properties (130) . However, as FESEM microscopy confirmed, the fibrillar formation of the hydrogels remains similar, suggesting that the porphyrin derivatives did not disturb the inherent structure of the Fmoc-FF hydrogel (131). Although the 3D structure of the hydrogels is stable, the mechanical properties change due to the adding of porphyrin. The highest decrease in Young modulus was observed with the Fmoc-FF-$H_2T(MePy)P(I_4)$, while the Fmoc-FF-Zn-$T(MePy)P(Cl_4)$ exhibited minimal effect. These observations suggest that Fmoc-FF-$H_2T(MePy)P(I_4)$ can be applied when a softer material

hydrogel is required, while the metallo-analogues may indicate its suitability for applications where stiffer hydrogels are needed.

In hydrogels, the typical mesh sizes range from 5 to 100 nm (132), and these sizes play a pivotal role in determining the release rate. Beyond the mesh size, factors such as the concentration of the encapsulated photosensitizer, size of the dye, and molecular weight are influential. Moreover, dyes with larger dimensions and greater molecular weights tend to have a limited release rate. Given these insights, it is evident that these parameters can tailor the release rate, underscoring the potential of these hydrogels in drug delivery applications (133).

Our work recorded a relatively weak cumulative release rate of the porphyrins, ranging from 7 to 13 %. However, we observed a burst release within the first two hours, similar to Elkihel, who investigated the release of porphyrins from xylan-cross-linked hydrogels (134). This result indicates strong electrostatic interactions between the cationic porphyrins and the hydrogel scaffold, consisting of aromatic rings, and probably due to the free carboxy-termini of the Fmoc-FF.

Importantly, these releases (20 to 40 μM) did not show any cytotoxic effect on the NIH3T3 fibroblast cell line without light irradiation. Likewise, Yegorov and colleagues illustrated that in the absence of light, cationic porphyrins exhibit negligible cytotoxicity even at higher concentrations exceeding 50 μM (135). Yet, these porphyrins demonstrated pronounced antimicrobial activity against tested bacterial strains. The mechanism underlying this antimicrobial efficacy is well-studied and depends on the generation of reactive oxygen species (ROS). This mechanism is influenced by factors including the number of positive charges on the porphyrin, their spatial arrangement at the peripheral positions of the photosensitizer (PS), and the incorporation of highly hydrophobic aromatic side groups (118).

Prior studies have proved that the Fmoc-FF peptide can exhibit antimicrobial potency against multiple bacterial strains due to its aromaticity and surfactant properties (136). Our data corroborated the Fmoc-FF peptide's pronounced antimicrobial efficiency, displaying superior efficacy against *S. aureus*.

Cationic porphyrins, such as TMPyP, are potent photosensitizers, effectively photo-inactivating diverse bacterial strains (112). The 5,10,15,20-tetrakis (*N*-methylpyridi-

nium-4-yl) porphyrin has already been tested in several photoinactivation studies and has presented good PDI results (137) . Interestingly, in the absence of light, the porphyrin H_2-TMePyP(I_4) displayed negligible impact on bacterial viability. Yet, upon irradiation, it showcased substantial efficacy against Gram-positive and Gram-negative bacteria, aligning with Nitzan's findings (138) . The cytotoxicity of these cationic compounds, even without light exposure, might be due to their quaternary ammonium charge, which is known to impair the integrity of bacterial cells (139).

Prior research indicates that metallic constituents can modulate the stability and photophysical properties of the porphyrin macrocycle (134). Specifically, Zn (II)-metalloporphyrin complexes might exhibit heightened efficiency compared to their free base counterparts. Even under dark conditions, no significant changes in efficiency are observed between *E .coli* and *S. aureus* though there are some fluctuations with light activation. Both Zn-T(MePy)P(I_4) and Zn-T(MePy)P(Cl_4) exhibit higher bactericidal efficiency compared to H_2-T(MePyP(I_4).

Notably, these compounds show the highest levels of aPDI inactivation against *E. coli*. The superior efficiency of Zn-T(MePy)P(I_4) might be attributed to a more significant release of porphyrin from its scaffold. These observations confirm that Gram-negative bacterial cells, like *E. coli*, tend to be more resistant to these compounds (141).

3.5 Conclusion

This study focuses on the potential of Fmoc-FF dipeptide hydrogels encapsulating with porphyrin chromophores, offering innovative solutions to the pressing challenge of antimicrobial resistance. Our research confirms these hydrogels' effective self-assembly and mechanical adaptability based on the chosen photosensitizer. The irradiated porphyrins exhibited significant efficacy against bacteria, highlighting their antimicrobial capabilities. Notably, metallic porphyrins, particularly Zn(II)-metalloporphyrin complexes, display enhanced bactericidal efficiency. Of note, we have recently encapsulated the porphyrin H_2T(MePy)P(I_4), (A) in Figure 20 into Fmoc-FF hydrogels as described above; their delivery through the self-assembling hydrogel accelerated the healing of experimental skin defects *in vivo*. These studies were carried out by Prof. Ismene Dontas's group in the Veterinary Medicine, Laboratory of the Musculoskeletal system at the School of Medicine, of the National

and Kapodistrian University of Athens and resulted in a joint publication (142) . Therefore, these hydrogels present a promising alternative for both wound care and combating bacterial infections in the face of growing AMR concerns.

Chapter II

4. “Peptide Labeling through Metallochelate Coupling with Porphyrin-Nitrilotriacetic Acid Dyads”

The following study was published in ACS omega with the title “Design and Synthesis of Porphyrin−Nitrilotriacetic Acid Dyads with Potential Applications in Peptide Labeling through Metallochelate Coupling” (143) . My contribution to this paper consisted of the study of the formed probes. Field-Emission Scanning Microscopy was used for the characterization of the formed probes, and then UV-Vis absorption experiments were conducted to verify the successful coordination of the peptide-porphyrin-NTA hybrids with the oligopeptides. Finally, the peptide-porphyrin-NTA hybrids were tested for their ability to enter into HeLa cells.

4.1 Introduction

Proteins play a critical role in numerous biological processes, including biocatalysis, molecular recognition, metabolism, and cell signaling. While extensive studies have been conducted on proteins in vitro, recent research focuses on investigating them under more biologically relevant conditions.

For tracking biomolecules (proteins, antibodies, amino acids, and peptides), labeling with a reporter or sensor is commonly employed. Currently, there are various labeling methods available, including radioactive tracers, isotope markers (144), colorimetric biosensors, photoswitchable biomaterials, photochromic compounds (145) electrochemical sensors (146), and fluorescent labels (147). Among these methods, fluorescent labeling stands out as a prominent choice due to its non-destructive nature and high sensitivity (140). The field of fluorescence techniques has witnessed considerable progress in both instrumentation and the synthesis of new fluorophores, including semiconductor nanocrystals, fluorescent proteins, and organic molecules (149).

The most commonly employed technique involves attaching fluorescent proteins (FPs) such as green fluorescent protein (GFP), to the proteins of interest (POIs), enabling their visualization in live cells or animals. However, the large size of fluorescent molecules may have adverse effects on the natural functions of POIs and they have limited utility as fluorescent markers in bioimaging studies. To address these limitations and provide a more reliable protein labeling approach, many research groups have proposed peptide-based recognition tags as an appealing alternative for protein labeling (150).

In this approach, the POI is genetically fused to the N- or C- terminal with a short peptide that binds specifically to a synthetic fluorescent probe (151). The tag-labeling technique offers the advantages of high labeling specificity and minimal disruption to protein folding and function (150).

The coordination of the hexahistidine sequence (His_6-tag) with nitrilotriacetic acid (NTA) through transition metal ions (Zn^{2+}, Ni^{2+}, Co^{2+}, or Cu^{2+} has emerged as a valuable method for live cell imaging. This approach offers an excellent opportunity to observe various cellular events while causing minimal disruption to the function and spatial arrangement of the protein of interest (POI). Additionally, it has found widespread use in molecular biology and biotechnology, especially in affinity chromatography-based protein purification.

Porphyrins and metalloporphyrins represent a class of compounds, which appears to be a very promising labeling tool due to their unique spectroscopic and luminescent properties. There are several publications where porphyrin-based fluorophores were employed in peptide labeling (152,153). However, to the best of our knowledge, there is only one report in the literature where porphyrin derivatives bearing NTA groups have been employed in the labeling of various peptides and proteins that possess the His_6-tag (80). More specific, metallochelate coupling was applied to produce several oligopeptide- and polypeptide-based phosphorescent probes. Notably, the coordination of the porphyrin derivative with the polypeptide had minimal effect on the photophysics of the porphyrin moiety.

In our investigation, we deliberately selected two distinct peptide sequences that incorporate histidine (His) residues as identification tags. Our aim was to showcase their capability to effectively coordinate with fluorescent probes via the NTA group.

The peptide sequences Fmoc-FH and RGDSGAITIGH were selected, cause they have a remarkable propensity for self-assembly, leading to the creation of diverse nanostructures. Additionally, due to the presence of a histidine residue within their molecular structure, they can serve as models for emulating the His6-tag.

By integrating lysine-NTA units, the designed fluorescent probes were intended for use in metallochelate coupling chemistry to label target biomolecules. The linkage of TPP-Lys-NTA was established through an amide bond, while in the case of TPP-CC-Lys-NTA, a triazine ring was strategically chosen as the connecting linker. The Py3P-Lys-NTA features three pyridyl groups, a modification anticipated to enhance the hydrophilicity of the final dyad.

Based on the hydrophilicity of the porphyrin derivatives, the peptide sequence Fmoc-FH was chosen to coordinate with the TPP-Lys-NTA. The fluorenylmethoxycarbonyl group (Fmoc) is a well-known protecting group, that is used widely in peptide chemistry due to its anti-inflammatory properties (53). The Fmoc–dipeptides can self-assemble into well-ordered architectures owing to the π–π interactions, between the aromatic electrons of the fluorenyl rings and the formation of hydrogen bonds. Based on many studies that have proven the capability of the peptide FF to self-assemble into these well-ordered nanostructures (154), an analog dipeptide FH with the residue histidine in C terminus in order to coordinate with the porphyrin via NTA moiety has been proposed.

On the other hand, for the studies of the water-soluble dyad Py3P-Lys-NTA, the designed entecapeptide RGDSGAITIGH (RGD_H) was selected as a probe. The RGD (Arg-Gly-Asp) tripeptide is one of the most preserved motifs throughout the evolution as well as the most commonly present on the surfaces of various proteins of the extracellular matrix (ECM) such as fibronectin, vitronectin, osteopontin, and fibrinogen (155). In particular, the RGD motif is recognized by, and bound to, a major class of transmembrane glycoproteins called as integrins that main role is to adhere the cells and facilitate cell matrix, as well as cell aggregation (156) Specifically, computational studies have proven that the RGD motif is exposed and it could probably possess the adhesion to the cells (157) . Moreover, according to computational and experimental studies, the GAITIG sequence is a β-amyloid forming motif of the adenovirus fiber shaft, and it represents an innovative tool for the

synthesis of new multi-purpose biomaterials with a large variety of applications, either biomedical or technological (158) . Both peptides RGD_H and RGD_F are highly ordered and well-aligned β-sheet states and the residues histidine and phenylananine in the C-terminus are exposed to coordinate. The RGDSGAITIGF (RGD_F) oligopeptide, which lacks the histidine residue, was used as a control peptide. Both peptides RGD_H and RGD_F are highly ordered and form well-aligned β-sheet states. The residues in their C-terminus site (histidine and phenylalanine, respectively) are exposed outside the self-assembling GAITIG core and therefore are prone to coordination.

4.2 Materials and Methods

4.2.1 Materials

RGDSGAITIGH and RGDSGAITIGF were purchased by Genecust. The purity of the peptides was 77% and 78%, respectively. The porphyrin derivatives were synthesized by Coutsolelos lab, at the Department of Chemistry, University of Crete. The NIH3T3 cell line was cultured at 37 ^{o}C, 5% CO_2 in DMEM (Gibco) supplemented with 10% fetal bovine serum (Gibco) and 50 μg/mL gentamycin. DAPI was purchased from ThermoFisher Scientific.

4.2.2 Preparation of the Solutions for the Metallochelate Coupling Studies

For the water-insoluble hybrid TPP-LysNTA, the following procedure was used: A stock solution (1.9×10^{-2} M) of TPP-Lys-NTA was prepared by dissolving 0.86 mg in 50 μL of HFIP, while for the $NiSO_4$ stock solution (4×10^{-3} M), we dissolved 0.5 mg in 800 μL of HEPES pH 7.4. Then, to a solution of the Fmoc-FH peptide (0.3 mg) in 15 μL of HFIP, we added 15 μL from TPP-Lys-NTA and 70 μL from $NiSO_4$ stock solutions. The final concentration of both TPPLys-NTA and $NiSO_4$ was 2.85×10^{-3} M in this solution (solution 1). Moreover, the following control samples were prepared: Solution 2: 0.3 mg of Fmoc-FH dissolved in 30 μL of HFIP and then diluted with 70 μL of HEPES pH 7.4. Solution 3: 15 μL from the stock solution of TPP-Lys-NTA porphyrin was diluted with 15 μL of HFIP and 70 μL of HEPES pH 7.4. Solution 4: 15 μL from the stock solution of TPP-Lys-NTA porphyrin was diluted with 15 μL of HFIP and then 70 μL from the $NiSO_4$ stock solution was introduced.

Solution 5: 0.3 mg of Fmoc-FH dissolved in 15 μL of HFIP and then 15 μL from the stock solution of TPP-Lys-NTA porphyrin and 70 μL of HEPES pH 7.4 were introduced. For the water-soluble Py3P-Lys-NTA derivative, the following procedure was applied: A stock solution (4.6×10^{-3} M) of Py3P-Lys-NTA was prepared by dissolving 0.5 mg in 120 μL of HEPES pH 7.4, while for $NiSO_4$, a stock solution of 4.6×10^{-3} M concentration was also prepared. Peptides RGDSGAITIGH (4.6×10^{-3} M) and RGDSGAITIGF (4.6×10^{-3} M) were dissolved in HEPES pH 7.4 and incubated for 3 days at room temperature to self-assemble. Then, equimolar quantities of Py3P-Lys-NTA and $NiSO_4$ were mixed and left at room temperature for 30 min. Twenty-five microliters from the above Py3P-Lys-NTA-Ni^{2+} solution were added to 25 μL of the RGDSGAITIGH (solution 6) and RGDSGAITIGF (solution 7) peptide stock solutions. The final concentration of the porphyrin was 1.15×10^{-3} M and that of the peptides was 2.3×10^{-3} M in both cases. Moreover, the following control samples were prepared: Solution 8: 25 μL from the Py3P-Lys-NTA-Ni^{2+} stock solution was diluted with 25 μL of HEPES pH 7.4. Solution 9: 25 μL from the RGDSGAITIGH stock solution was mixed with 12.5 μL from the Py3P-Lys-NTA stock solution, and then 12.5 μL of HEPES pH 7.4 was introduced. Solution 10: 25 μL from the RGDSGAITIGF stock solution was mixed with 12.5 μL from the Py3P-Lys-NTA stock solution and then 12.5 μL of HEPES pH 7.4 was introduced. For the solid-state absorption experiments, 10 μL from each solution was transferred to quartz slides 2×2 cm^2 and left to dry overnight.

4.2.3 Field-Emission Scanning Electron Microscopy (FESEM)

Samples for FESEM analysis were prepared by depositing 10 μL from each peptide solution on a 12 mm coverglass and leaving to dry overnight. Then, the samples were covered with 10 nm Au sputtering and observed directly. FESEM experiments were performed using a JEOL JSM 7000F (FESEM) operating at 15 kV.

4.2.4 Cell Lines and Culture Conditions

Human epithelial cervical carcinoma cells (HeLa) were grown in Dulbecco's modified Eagle's medium (DMEM) growth medium (pH 7.4) supplemented with 10% fetal bovine serum (FBS) and 50 μg· mL^{-1} gentamycin at 37 °C in a 5% humidified CO_2 incubator.

4.2.5 Confocal Microscopy Studies with Cells

In total, 8×10^4 HeLa cervical carcinoma cells were seeded for 24 h in a 24-well plate after the addition of a 13 mm tissue culture coverslip at the bottom of the well and allowed to attach overnight. The following day, the culture medium was removed, 5 μL from solutions 1, 3, 5, and 7 were added to 495 μL of fresh DMEM, and the mixture was subsequently added to the cell culture. Cells were incubated with the added solutions for 4 h at 37 °C. Afterward, the cells were washed two times with PBS 1X for 5 min, fixed with 4% formaldehyde for 15 min, and washed twice with 1× PBS. Cells were further treated with a drop of the DAPI nuclear staining dye. After that, a 13 nm coverslip was placed on top, and the internalization of the metallochelate conjugation system was assessed using a Leica SP8 inverted confocal microscope. The excitation wavelength for porphyrin Py3P-Lys-NTA was 514 nm and that for DAPI was 405 nm. To avoid un-specific excitation of the porphyrin, the TPP-LysNTA hybrid was excited at 405 nm, but without DAPI nuclear staining. Considering these limitations in the latter case, pictures with no fluorescence filter were also taken to delimit the cells.

4.3 Results

4.3.1 Metallochelate Coupling Studies

Solid-state absorption spectroscopy studies were performed to investigate the metallochelate coupling between porphyrin−NTA hybrids, nickel (Ni^{2+}) ions, and the histidine-bearing peptides. The spectra were recorded in the solid state since the peptides that were used have the ability to self-assemble and form water insoluble aggregates. In the case of TPP-Lys-NTA, the Fmoc-FH dipeptide was employed, while for the water-soluble Py3P-Lys-NTA dyad, the RGDSGAITIGH oligopeptide was employed as a mimic of the His_6-tag. In all these experiments, the ratio of the porphyrin hybrid relative to the corresponding peptide was 1:2. The solid-state UV−vis spectrum of TPP-Lys-NTA (solution 3) displayed the characteristic porphyrin features with the Soret band at 430 nm. After the addition of Ni^{2+} ions (solution 4), the spectrum remains intact without any significant shift of the peaks. This result suggests that there are no noteworthy electronic interactions between the porphyrin chromophore and the Ni^{2+} ions. Additionally, the control sample that contained only

TPP-Lys-NTA and Fmoc-FH (solution 5) did not present any significant differences. However, the solid-state spectrum that contains all of three components (TPP-Lys-NTA, Ni^{2+} and Fmoc-FH) presented several differences. More specifically, the characteristic porphyrin maxima were red-shifted and significantly broadened. These changes can be attributed to the binding of the TPP-Lys-NTA hybrid with the Fmoc-FH peptide via the metallochelate coupling with the NTA moiety. Concerning the hydrophilic Py3P-Lys-NTA derivative, the histidine-containing peptide RGDSGAITIGH was applied as the His_6-tag mimic. Moreover, the RGDSGAITIGF peptide, which replaced the histidine residue by phenylalanine, was employed as a "control" molecule.

As illustrated in Figure 30, the spectrum of Py3P-Lys-NTA Ni^{2+} (solution 8) changes significantly after the addition of the RGDSGAITIGH peptide (solution 6). More specifically, all of the porphyrin absorption peaks were blue-shifted up to 14 nm.

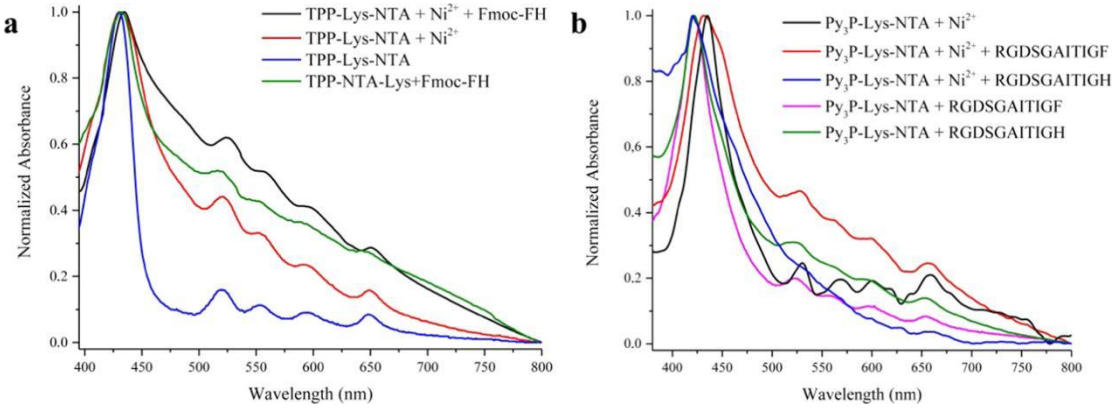

Figure 30: Solid-state absorption spectra of TPP-Lys-NTA (solution 3, blue line), the complex of TPP-Lys-NTA + Ni^{2+} (solution 4, red line), the control sample TPP-Lys-NTA + Fmoc-FH (solution 5, olive line), and the complex TPP-Lys-NTA + Ni^{2+} + Fmoc-FH (solution 1, black line). (b) Solid-state absorption spectra of Py3P-Lys-NTA + Ni^{2+} (solution 8, black line), after the addition of RGDSGAITIGH (solution 6, blue line), after adding RGDSGAITIGF (solution 7, red line), the control sample RGDSGAITIGH + Py3P-Lys-NTA (solution 9, olive line), and the control sample RGDSGAITIGF + Py3P-Lys-NTA (solution 10, magenta line).

Table 1: Absorption Peak Values of All of the Studied Compounds in Solution and in the Solid State

compound	soret band λ_{max} (nm)	Q bands λ_{max} (nm)
TPP-Lys-NTA solution	418	514, 548, 590, 646
Py_3P-Lys-NTA solution	416	512, 546, 587, 643
TPP-Lys-NTA	430	519, 553, 594, 648
TPP-Lys-NTA + Ni^{2+}	431	521, 553, 593, 649
Fmoc-FH + TPP-Lys-NTA	432	518, 553, 592, 645
Fmoc-FH + TPP-Lys-NTA + Ni^{2+}	435	524, 555, 594, 651
Py_3P-Lys-NTA + Ni^{2+}	434	530, 568, 601, 658
RGDSGAITIGF + Py_3P-Lys-NTA	422	521, 557, 599, 652
RGDSGAITIGH + Py_3P-Lys-NTA	422	522, 558, 597, 650
RGDSGAITIGF + Py_3P-Lys-NTA + Ni^{2+}	431	527, 562, 600, 654
RGDSGAITIGH + Py_3P-Lys-NTA + Ni^{2+}	420	

On the other hand, the introduction of the control RGDSGAITIGF oligopeptide (solution 7) did not alter significantly the absorption features of the porphyrin (the Soret band was blue-shifted by only 4 nm). Interestingly, the control samples that contained the Py3P-Lys-NTA porphyrin and the oligopeptides RGDSGAITIGH or RGDSGAITIGF without the Ni^{2+} ions (solutions 9 and 10, respectively) presented also significantly blue-shifted spectra. The recorded absorption maxima were similar to the sample containing RGDSGAITIGH + Py3P-Lys-NTA + Ni^{2+} (solution 6). These unexpected results indicate that the Py3P-Lys-NTA porphyrin interacts strongly with both oligopeptides, even without the contribution of Ni^{2+} ions. Most likely, the carboxylic groups of the NTA moiety can form hydrogen bonds with the amino groups of the oligopeptides. However, this interaction is possible only in the absence of Ni^{2+} ions since in the sample with RGDSGAITIGF + Py3PLys-NTA + Ni^{2+} (solution 7) we did not observe this process.

4.3.2 Field-Emission Scanning Electron Microscopy (FE-SEM)

To provide additional evidence for the ability of porphyrin−NTA hybrids to coordinate with histidine-bearing peptides in the presence of Ni^{2+} ions via metallochelate coupling, FE-SEM observatios were performed. TPP-Lys-NTA derivative was able to self-assemble and formed flake-shaped nanostructures, while

the addition of Ni^{2+} ions altered the self-assembly mode of the porphyrin and resulted in spherical architectures with a size of 100−200 nm (Figure 31). This observation verifies the ability of the NTA part to coordinate with the Ni^{2+} ions. On the other hand, the Fmoc-FH dipeptide could assemble into a fibrillar network. Interestingly, in the sample containing both Fmoc-FH and TPP-Lys-NTA, the two components self-assemble independently and form fibrillar nanostructures covered with spheres, verifying that there is no significant interaction between them. Finally, the combination of FmocFH with TPP-Lys-NTA-Ni^{2+} resulted also in the formation of more well-defined spherical nanostructures with significantly increased diameters (100−500 nm). These modifications can be attributed to the coordination of the TPP-Lys-NTA hybrid with the Fmoc-FH through metallochelate coupling Similar observations by FE-SEM studies were also detected for the water-soluble Py3P-Lys-NTA derivative. The Py3P-LysNTA hybrid after the addition of Ni^{2+} ions showed undefined structures (Figure 32). However, after the addition of the RGDSGAITIGH peptide, the self-assembly mode was modified completely and the formation of a porous fibrillar network was observed. On the other hand, the addition of the control RGDSGAITIGF peptide resulted in the formation of thinner fibrils, and smaller pores were detected between the nanostructures. The divergences that were noticed in these images before and after the addition of the oligopeptides indicate that metallochelate coupling takes place. Remarkably, RGDSGAITIGH and the control RGDSGAITIGF, after the addition of the Py3P-Lys-NTA hybrid without Ni^{2+} ions, could also assemble into well-defined fibrillar networks. These results are in accordance with the absorption studies where we observed that Py3P-Lys-NTA interacts with both oligopeptides even in the absence of Ni^{2+} ions.

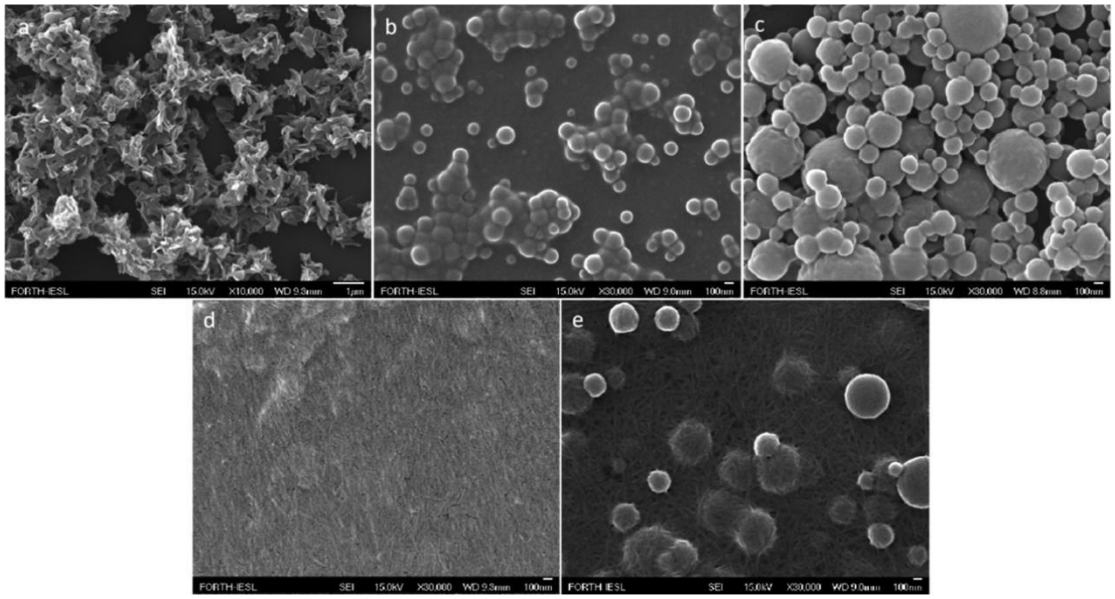

Figure 31: Field-emission SEM (FE-SEM) pictures of (a) TPP-Lys-NTA (solution 3), (b) TPP-Lys-NTA and Ni^{2+} (solution 4), (c) Fmoc-FH and TPP-Lys-NTA with Ni^{2+} (solution 1), (d) Fmoc-FH (solution 2), and (e) Fmoc-FH and TPP-Lys-NTA (solution 5). All of the above samples were prepared in hexafluoroisopropanol/4-(2-hydroxyethyl)-1-piperazine ethanesulphonic acid (HFIP/HEPES) 50 mM pH 7.4 (3:7, v/v) solvent mixture.

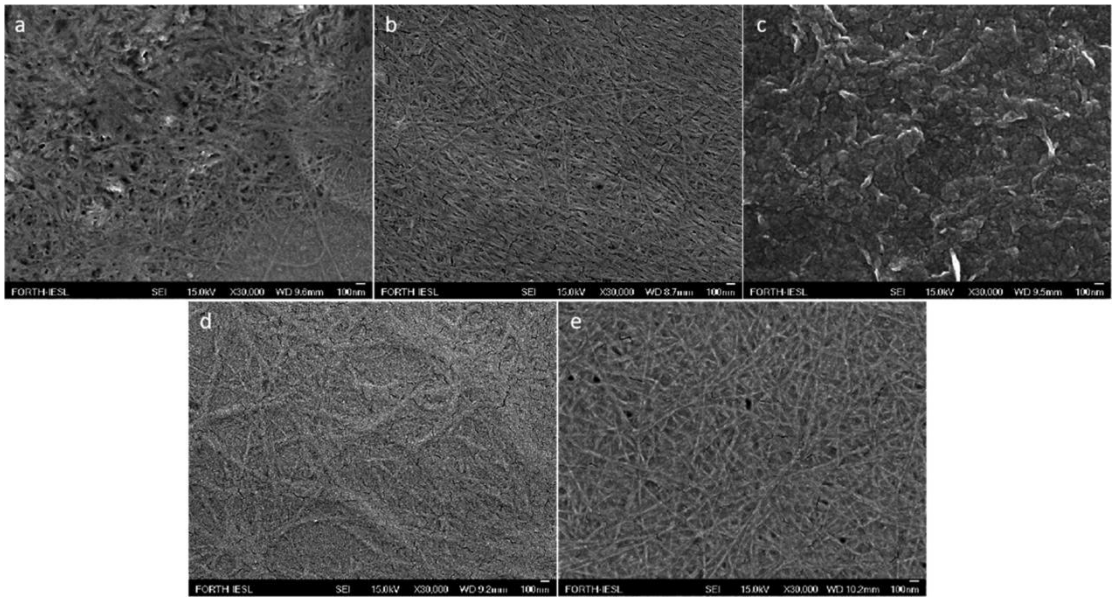

Figure 32: Field-emission SEM (FE-SEM) pictures of (a) RGDSGAITIGH + Py3P-Lys-NTA + Ni^{2+} (solution 6), (b) RGDSGAITIGF + Py3PLys-NTA + Ni^{2+} (solution 7), (c) Py3P-Lys-NTA + Ni^{2+} (solution 8), (d) RGDSGAITIGH + Py3P-Lys-NTA (solution 9), and (e) RGDSGAITIGF + Py3P-Lys-NTA (solution 10). Time of incubation: 7 days.

4.3.3 Confocal Microscopy Investigation with HeLa Cells

Based on the above encouraging results, which verified the ability of the porphyrin−NTA hybrids to coordinate with the histidine-containing peptides, we additionally performed internalization experiments into mammalian cells to study the

capability of the final complexes to penetrate the cells. For these studies, solutions 1, 4, 6, and 8 were employed. Confocal microscopy experiments demonstrated that the porphyrin TPP-Lys-NTA alone and the complex of TPP-LysNTA with the peptide Fmoc-FH entered efficiently into the HeLa cells and accumulated into the cytoplasm. There is no evidence of accumulation in the nucleus (Figure 33). The fluorescence signal was calculated and compared for both the porphyrin and the peptide−porphyrin complex with ImageJ software. The emitted fluorescence was similar for each sample with no statistical difference between them. Similar studies were performed with the hydrophilic porphyrin Py3P-Lys-NTA before and after its complexation with the peptide sequence RGDSGAITIGH. Moreover, to facilitate the examination of the cell internalization propensity of the complexes, the 4′,6-diamidino-2-phenylindole (DAPI) nuclear staining assay was employed. DAPI is a blue- fluorescent DNA staining dye commonly used to distinguish the cell nucleus location. The porphyrin gives a strong fluorescent signal around the nucleus, as shown in (Figure 34). In both cases (with or without the RGDSGAITIGH peptide), the porphyrin seems to internalize in the cell and localize in the cytoplasm.

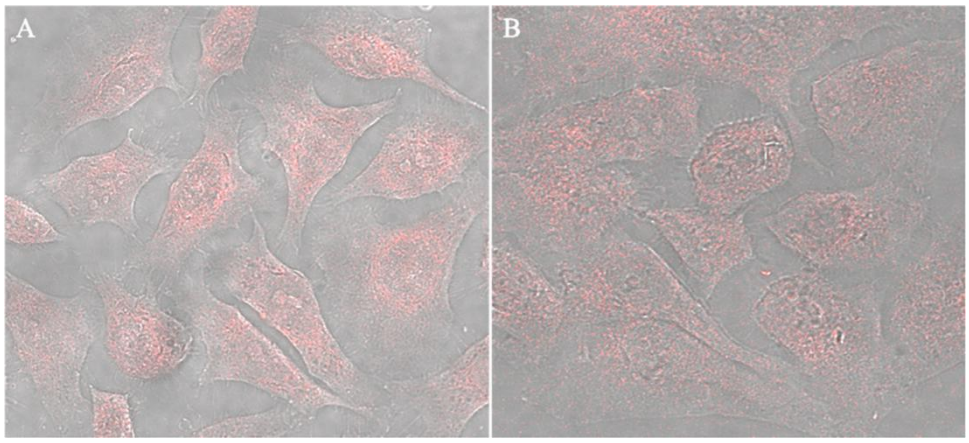

Figure 33: Confocal microscopy pictures correspond to cellular uptake of (A) TPP-Lys-NTA + Ni^{2+} and (B) TPP-Lys-NTA + Ni^{2+}+ Fmoc-FH. HeLa cells were exposed to 5 μL of solutions 1 and 3, followed by 24 h incubation. The bright-field illumination form was applied additionally to circumscribe the limits of the cell membranes.

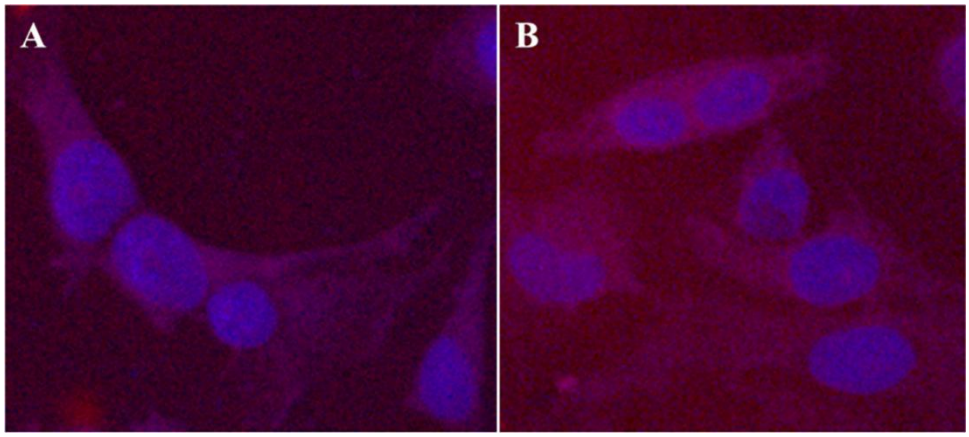

Figure 34: Confocal microscopy pictures correspond to the cellular uptake of (A) Py3P-Lys-NTA + Ni^{2+} and (B) Py3P-Lys-NTA + Ni^{2+}+RGDSGAITIGH. HeLa cells were exposed to 5 μL of solutions 5 and 6 followed by 24 h incubation. Cells were washed and stained with DAPI nuclear staining for confocal microscopy observations.

4.4 Discussion & Conclusions

This observation can be rationalized based on the work of Hiyama and his group, which demonstrated that exogenous porphyrin could be recognized by the heme carrier protein receptors HCP-1 since the porphyrin structure is virtually the same as heme. These receptors are overexpressed into the cancer cells, and as a result, the uptake of porphyrin increases (159). Moreover, the RGD motif can be recognized by the integrin receptors on the cell membranes, so this can further facilitate the penetration of the bound porphyrin complex into the cell matrix (154).

Small therapeutic molecules like porphyrins usually exhibit a lack of tissue targeting ability, poor pharmacokinetics, and poor stability. Although porphyrin molecules alone can independently internalize the cells, the complexation with a peptide containing the RGD motif could greatly enhance the internalization ability and porphyrin accumulation in the cells. RGD is widely used in drug delivery applications and especially for tumor-targeted purposes due to the increased overexpression of integrins on cancerous cells, as described before (160). It is known that the RGD motif located in the N-terminus of the chelator can be recognized specifically by 7−8 integrins, such as the a5b1, avb5, and αvβ3 (161).

Moreover, in various tumor cells, there is overexpression of some RGD specific integrin receptors (162). The HeLa cells could overexpress at least 2−3 receptors,

including the integrin avb3 (163) . Since porphyrins are also commonly used for photodynamic therapy (PDT) for anticancer treatment, this combination of the RGD peptide bound with a porphyrin molecule could hold great potential for antitumor applications. Furthermore, it should be noted that for this kind of theranostic molecule, sustaining blood retention is of great importance. Previous studies demonstrated the importance of the RGD motif as a blood circulation-prolonging (BCP) peptide (164). Usually, the endogenous ligands in the bloodstream compete with the drug delivery vectors for binding to the tissue target. The presence of a target motif, like the RGD motif for tumor cells, greatly enhances the receptor uptake of cells in contrast to the nontargeted vectors (165) . Based on our observations and having in mind the advantages of the RGD motif, one could consider that the coordinated Py3P-Lys-NTA with the RGDSGAITIGH peptide could extend the retention time and the accumulation quantity of the porphyrin in the cells. More experiments i*n vivo* are needed to testify this potential use of porphyrin.

The exploitation of functional organic molecules for the decoding of biological functions within organisms has been of great importance in the past few decades. Complexation of appropriately bound chromophores through chelate bonding with metals and amino acids, known as metal−chelate binding, can boost the research in the field of labeling and imaging. In this work, three new porphyrin−NTA dyads, TPP-LysNTA, and Py3P-Lys-NTA connected to a nitrilotriacetate metal−chelate ligand through different bridging groups, were successfully synthesized and spectroscopically analyzed. According to fluorescence measurements, complexation of each dyad with Ni^{2+} ions is possible, making them good candidates as potential probes. Alterations in the periphery groups of the porphyrin ring as well as the distance between the chromophore and the chelator can overcome the solubility issues and the quenched emission of the fluorophores after their interaction with Ni^{2+} ions. The synthesized hybrids can coordinate with histidine-containing oligopeptides through metallochelate coupling. Histidine-containing peptides are particularly appropriate for intracellular delivery of labeling and imaging chromophores or other types of cargo. The imidazole group of histidine, with a pK of around 6, protonates in intracellular conditions, especially within the endosomes in increasingly acidic conditions. This results in endosomal lysis and release of the chromophore or other

types of cargo in the cytoplasm (166) . Consequently, chemically differentiated porphyrin derivatives may contribute to the increase of new and efficient probes for labeling and other biological applications, both *in vitro* and *in vivo.* At this direction, further experiments with peptides and the aforementioned porphyrin−NTA compounds are foreseen.

Acknowledging the critical role of the histidine residue in forming metal complexes essential for bioimaging applications, our research progressed to emphasize cyclic peptides containing histidine. Compared to their linear counterparts, cyclic peptides offer notable advantages. Their conformational rigidity, combined with an enhanced affinity for metal binding, puts them as promising subjects for in-depth investigation, especially concerning metal coordination with cyclic histidine peptides. Moreover, their inherent responsiveness to pH changes further accentuates their potential in this realm.

Chapter III

5. “A study on the biological activity of the histidine-containing diketopiperazine, cyclo-(His-Phe) & its metal complexes”

5.1 Introduction

In the area of nanotechnology, transition metal nanoparticles (Me-NPs) have garnered considerable attention due to their potential applications in fields ranging from catalysis and medicine to electronics and photonics (167).

Recently, biomolecules, particularly peptides (168) , have emerged as an exciting avenue for nanoparticle synthesis and stabilization (169,170) . These bio-inspired approaches offer a “green” alternative to traditional methods and provide exceptional control over nanoparticle size, morphology, and functionality (167) . The increased attention to the peptides is primarily comes from their bio-compatibility and the diverse range of physicochemical advantages they confer (168). Moreover, compared to linear counterparts, the cyclic peptides display more excellent stability, significantly influencing the production of nanoparticles, both in size and shape (171) This characteristic underscores their potential for more intricate applications.

Delving deeper into the mechanism, the formation of peptide metal conjugates (PNCs) is initially dependent on the ionic bond between metal (Me) ions and amino acid residues (172) . For a successful formation of nanoparticles, the “ideal peptides” should contain amino acids that possess a balanced binding affinity for both metal ions and resultant metal particles. Amino acids like histidine (H), cysteine (C), and methionine (M) have the ability to form strong complexes with metal ions, making them promising candidates for this purpose (172).

In particular, histidine plays a significant role in the synthesis and stabilization of nanoparticles (NPs) due to its unique chemical properties. The imidazole group in the side chain of histidine can directly interact with and bind with metals (91), whereas it can facilitate the reduction of metal ions to form metal nanoparticles (172). Moreover, histidine can serve as a capping agent, ensuring the stability of the formed

nanoparticles. Its capability to chelate metal ions prevents aggregation, thus maintaining the size and distribution of the nanoparticles (173). Most importantly, it possesses a pH-responsive behavior, making it an attractive candidate for fabricating a pH-sensitive drug delivery system (174).

The HF peptide, comprising histidine with its metal-chelating imidazole group and phenylalanine (F) with its hydrophobic aromatic side chain, represents an intriguing molecular combination that can provide both reduction and stabilization in the nanoparticle formation process (175).

Amongst the metals, copper (Cu) and zinc (Zn) nanoparticles have generated considerable interest due to their multifaceted applications in biomedicine, electronics, and catalysis.

Copper is the third most abundant metal-tracing element after zinc in our bodies and plays a crucial role in fostering biological processes. The favorable characteristics of biological cells associated with copper predominantly rely on the metal's ability to transition between its +2 and +1 oxidation states. The oxidation states of copper play a crucial role as catalytic cofactors in the enzymatic functions of soluble redox proteins (176). Since copper can be oxidized easily in the presence of oxygen, forming Cu NPs is a common challenge, because they must be stored under inert atmosphere (Ar, N_2) or in solution to prevent rapid oxidation (177). Copper Oxide nanoparticles called Cupric Oxide, include two well-known oxides: tenorite (CuO) and cuprite Cu_2O (178). Copper Oxide Nanoparticles are as the most extensively researched nanoparticles due to their anti-microbial and anti-cancer properties (179).

Zinc is a fundamental component in many proteins and enzymes, actively shaping their structure and facilitating catalytic reactions. In addition, zinc is pivotal in the immune system's biological function; and consequently, its deficiency inhibits cell growth and promotes the development of diseases and potentially cancerous conditions (180). Zinc possesses strong reduction properties and readily oxidizes to zinc oxide (181). Among many transition metal oxides, ZnO is the most promising inorganic material with many applications (182).

Metal oxide nanoparticles, especially CuO and ZnO, have been proposed as new metal-based drugs (MBD) for their potent anticancer properties (183), to overcome platinum-based drugs (PBD) chemoresistance cancer (184). It is well known that the commercially available PDBs, such as cisplatin and oxaliplatin, are known to induce intrinsic and acquired chemoresistance due to their enhanced ROS production (185). When ROS production surpasses a certain threshold in cancer cells, it can be a target for oxidative therapy (89). Metal nanoparticles CuO and ZnO are proposed as alternatives for cancer treatment because they can induce cell death by producing oxidative stress (ROS) inside the cells (186).

The tumor microenvironment (TME), characterized by an acidic pH, elevated levels of glutathione (GSH), and hydrogen peroxide (H_2O_2), presents a unique therapeutic challenge and opportunity (187) NPs containing histidine, like cHF, respond dynamically to these pH fluctuations. The tumor's acidity prompts the protonation of pH-sensitive moieties in the NPs. The changes in the pH disrupt the hydrophilic-hydrophobic balance of the histidine NPs, leading to structural changes and the release of its therapeutic content (174). Then, an excess of copper or zinc ions converts the hydrogen peroxide (H_2O_2) to hydroxyl radicals (·OH), which triggers lipid peroxidation in the cell and results in cell damage, leading to cell death (188) (Figure 35).

Currently, research has focused on investigating the potential of zinc-histidine complexes as therapeutic agents against osteosarcoma cells (176) Osteosarcoma (OS) is the most common bone malignancy, particularly prevalent in children and adolescents. It is typically treated with surgical resection of the tumor tissue, followed by long-term chemotherapy to prevent recurrence (189).

Moreover, the NPs of metal oxide stand out in the field of antimicrobial compounds by their catalytic inhibition activity (190). The rapid rise of bacterial resistance, even among potent antibiotics, is increasingly posing a significant barrier to the effective use of antibiotics in fighting infectious diseases (191). Metallic nanoparticles, like silver, gold, copper, titanium, and zinc oxide, are the most potent antibacterial

inorganic materials (192). Various factors can influence the antibacterial activity of metal oxide nanoparticles such as particle size, surface area, crystallinity, capping/stabilizing agent, morphology, concentration/dosage, pH of the solution, and the nature of the microorganisms (182).

Similar to cancer cells, many researchers have proposed that the antimicrobial activity of copper and zinc NPs is probably due to the reaction of metal ions with endogenous H_2O_2 to produce reactive oxygen species (ROS) through Fenton-type reactions (193).

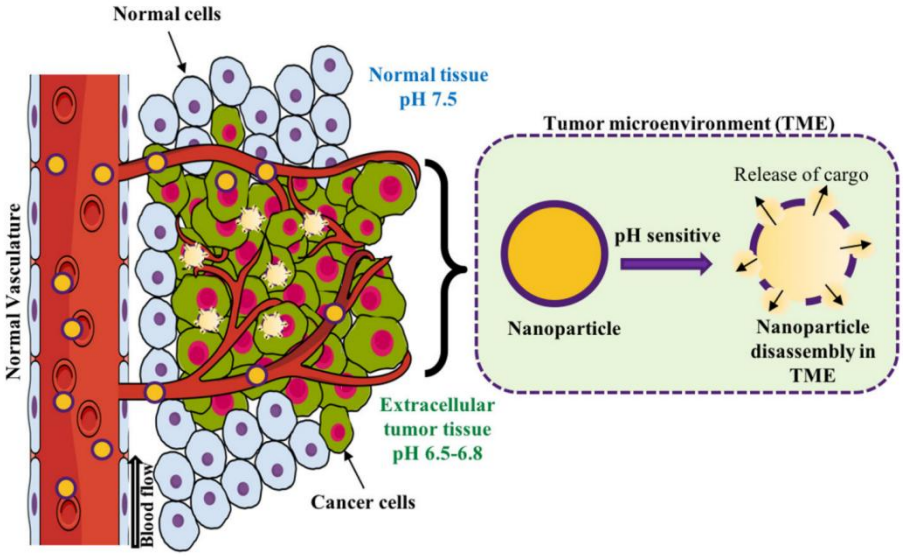

Figure 35: Schematic illustration of TME (174).

In this work, we attempt to delve deeper into the role of cyclic-HF peptides in forming Zn and Cu nanoparticles. By studying the NPs morphology by FESEM, TEM and FTIR, our objective is to decipher the therapeutic efficacy of these nanoparticles, particularly in the fields of cancer and infectious diseases. This exploration highlights the innovative use of cyclic peptides in nanoparticle research and paves the way for their potential applications as anticancer metal-based drugs and antibiotics.

5.2 Materials and Methods

5.2.1 Materials

Cyclo-(His-Phe) peptide powder was purchased by Bachem. The purity of the peptide was over 95%. The fibroblasts L929 and osteosarcoma MG-63 cell lines were cultured at 37 ^{o}C, 5% CO_2 in DMEM (Gibco) supplemented with 10% fetal bovine serum (Gibco) and 50 µg/mL gentamycin. Sodium borohydrite, Phosphate Buffered

Saline 10X, Thiazolyl blue tetrazolium bromide (MTT) and Congo red were purchased from Sigma-Aldrich.

- Methods

5.2.2 Sample Preparation

Initially, 1.3 mg of cyclo-(His-Phe) peptide powder was weighed and dissolved in 1 mL PBS 1X under heating at 40 ^{o}C and sonication for 20 min. When the samples were transparent, we added an appropriate amount of zinc or copper chloride to a volume of 1 ml (Stock Solutions Zinc & Copper Chloride 0.1 M). The samples were incubated for 70 min at room temperature and centrifuged at 7,000 rpm for 10 min. Then, the supernatant was removed and the pellet redissolved in 1 mL of water. Freshly prepared reducing agent $NaBH_4$ (0.25 M) was added in a molar ratio of metal to a reducing agent of 1 to 1. Followed incubation for 45 minutes at 80 ^{o}C and then at room temperature overnight. The next day, the samples were centrifuged at 7,000 rpm for 15 minutes, the supernatant was discarded, and the pellet was redissolved in 1 mL of water. We repeated this step twice. In the last step, the procedure was repeated by redissolving the peptide in 1 mL of pure ethanol. After centrifugation, the pellet was left at 80 ^{o}C to dry and stored in the refrigerator. Before each experiment, the samples were redissolved in PBS 1X, so the final concentration was 5 mM and sonicated in a bath at room temperature for 5 min. Also, the samples were exposed to ultraviolet light for 15 minutes before exposure to cell cultures to avoid bacterial contamination.

5.2.3 Morphological Characterization by FE-SEM

10 µL of each peptide sample was deposited on a cover glass and was air-dried overnight. Dried samples were covered with 10 nm of Au sputtering. Observation experiments were performed using a JEOL JSM-7000F microscope operating at 15 kV.

5.2.4 Morphological Characterization by TEM

8 µL of the aqueous solution containing the sample (dilution 1:10) was deposited for 2 minutes on the shiny side of the carbon-formvar grid. The excess fluid was removed

with the edge of an absorptive paper. The samples were ready for further investigation under JEOL JEM-2100 TEM.

5.2.5 Congo Red Staining

Each peptide solution (20 μL) was thoroughly mixed with 5 μL of a fresh Congo Red assay solution (10 mM Congo Red, 2.5 mM NaOH in 50% ethanol). A drop of the mixture was deposited onto a glass coverslip and was examined before or after drying at room temperature, with a Zeiss Stemi 2000-C microscope with and without the use of a crossed polarizer.

5.2.6 Fourier-transform infrared spectroscopy

Fourier transform infrared (FT-IR) spectra of the cyclo-(His-Phe) and its complexes, cyclo-(His-Phe) - Cu^{2+} and cyclo-(His-Phe) - Zn^{2+} were collected in order to analyze the chemical structure of these compounds. The FT-IR spectra were collected in the wavenumber range of 400–4,000 cm^{-1}. Spectra were collected with 4 cm^{-1} resolution and 128 scans. Fourier transform infrared (FT-IR) measurements were performed with a NICOLET 6700 FT-IR spectrometer.

5.2.7 MTT Cell Proliferation Assay

Cell viability in the presence of the peptides was studied by monitoring the conversion of thiazolyl blue tetrazolium bromide reagent (MTT) into formazan by the mitochondrial dehydrogenases of the living cells. L929 and MG-63 cell lines with concentrations of 10^4 cells/well were cultured in a 96-well plate. After 24 h of incubation, the medium was removed and then, the cHP - Cu^{2+} and cHP – Zn^{2+} complexes were added in a total volume of 100 μL of culture medium. As control, untreated cells were used. After an incubation period of 24 and 48 h, the medium was carefully removed and replaced with 100 μL of fresh medium and 10 μL of MTT (5 mg/mL) dissolved in PBS 1X. The cells were incubated for 4 h to allow the development of the purple formazan products and the MTT/culture medium was substituted with 100 μL of an isopropanol–DMSO 1:1 solution. The formazan crystals were allowed to dissolve for 15 min at 37 ^{o}C. The absorbance was measured at 570 nm in a Synergy HTX BioTEK Plate Reader.

5.2.8 Fixation and dehydration of cells MG-63 treated with cyclo-(His-Phe) and its complexes

MG-63 osteosarcoma cells were seeded on top of a circular cover glass of 10 mm inside a 24-well plate for 24 h. The next day, the cell medium was removed, and 100 µL of the cyclo-(His-Phe), and its complexes were added on top. The plates were incubated at 37 °C for 24 h. After 24 h the medium, where the complexes were diluted, was removed and the attached cells were washed twice with 300 µL of SCB 0.1 M. Cell fixation was carried out by adding 300 µL of 4% paraformaldehyde to each well, allowing it to incubate for 30 minutes. After removing the paraformaldehyde, the cells underwent two additional washes with 300 µL of SCB 0.1 M. Subsequently, the cells were subjected to successive 5-minute incubations with increasing concentrations of ethanol (30%, 50%, 70%, 90%, and 100% dry ethanol) to facilitate sample dehydration. Finally, 300 µL of HMDS was added to each well and left to evaporate overnight. The cover glass was removed and positioned on carbon tape for further processing and examination by FESEM.

5.2.9 Preparation of bacterial suspension

The bacterial strains of gram-negative *Escherichia coli* and gram-positive *Staphylococcus aureu*s bacteria were inoculated and cultivated in the Luria Bretani Broth and incubated at 37 ^{o}C for 18–20 h at 200 rpm. The concentration of bacterial suspension was then determined by the optical density at 600 nm using a UV-Vis spectrophotometer and diluted for further tests. All bacterial strains were maintained as glycerol stocks at -80 ^{o}C.

5.2.10 Antimicrobial Testing

One colony of *E. coli* was left to grow in 5 mL Luria Broth at 37^{o}C for 16 hours. Then, 500 µL of the pre-culture was transferred into 50 mL of Luria Broth (LB) and incubated in a shaker (200 rpm) at 37 ^{o}C until the mid-log phase ($O.D_{600}$=0.1). The bacterial cell number was diluted in the broth, and then, 90 µL was added to triplicate wells of a 96-well, to a final concentration of 10^5 CFU/mL. Each sample was redissolved in 100 µL PBS 1X and then, 10 µL was added to each well containing the bacteria suspension. The plates were incubated overnight at 37 ^{o}C and then, 10 µL of

each well was serial diluted and plated in Luria Broth agar plates. Incubated overnight at 37 ºC and colonies were counted. The results are presented as mean of triplicates of three independent experiments (n = 9).

5.2.11 Statistical Analysis

Statistical analysis was performed using ANOVA t-test in the GraphPad Prism version 8.3 software to evaluate significance of the differences among various scaffold compositions and the control. A p-value (*) <0.05 was considered significant, **p < 0.01, ***p < 0.001, ****p < 0.0001, ns denotes a statistically non-significant difference. Results are presented as mean ± SD.

5.3 Results

5.3.1 Formation of cyclo-(His-Phe)

Initially, FESEM and TEM observations demonstrated the ability of the the cyclo-(His-Phe) to assemble into fibrils (Figure 36 A, B). Furthermore, the addition of Congo Red stain to the incubated peptides revealed the amyloid characteristics of the fibrils, due to the yellow-green birefringence observed under a crossed polarizer (Figure 36).

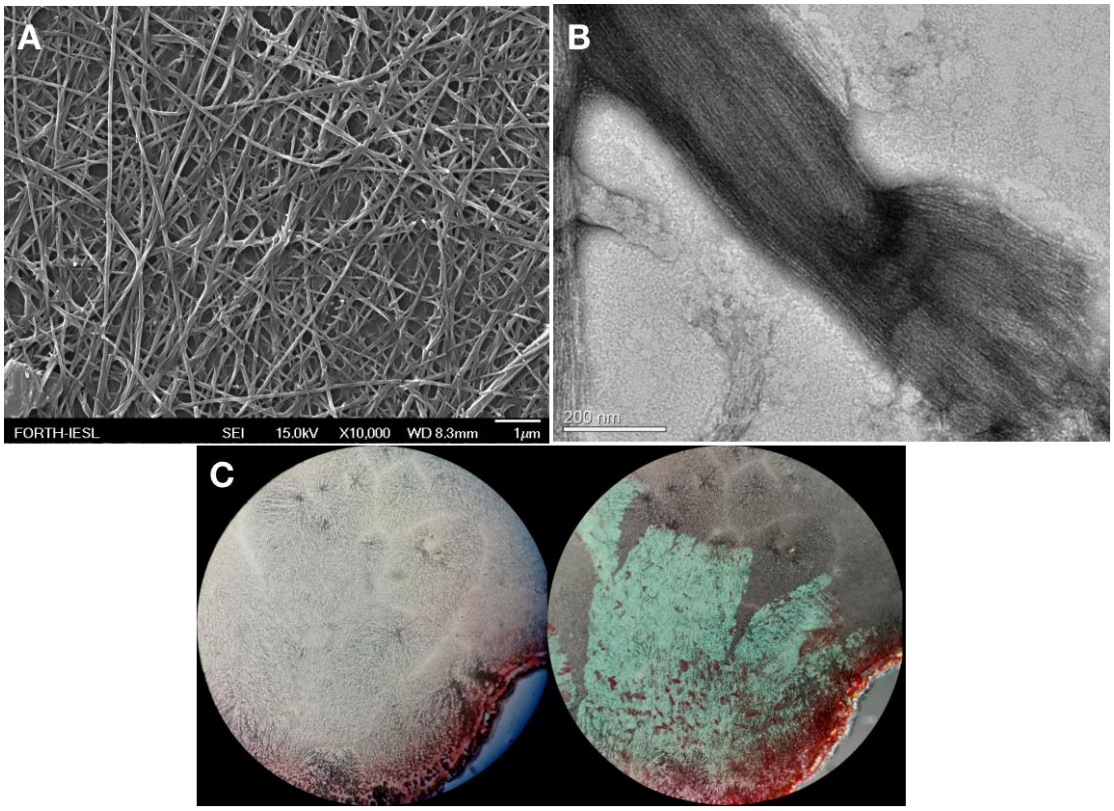

Figure 36: Images of cyclo-(His-Phe) at the concentration of 5 mM in PBS 1X, under A) FESEM microscopy, B) TEM microscopy, C) Congo red images without polarizer (left), under cross polarizer (right).

5.3.2 Formation of cyclo-(His-Phe) NPs

The formation of cHF-CuO NPs was observed with a color change from blue to brown due to the excitation of surface Plasmon resonance, indicating the synthesis of CuO NPs.

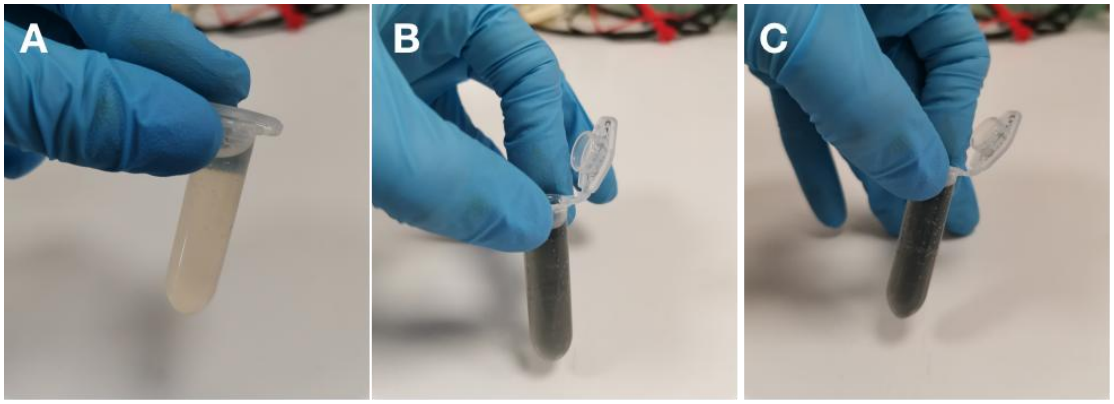

Figure 37: Progressive change of color during the formation of cHF-CuO NPs (5 mM).

To assess the binding affinity of metal ions (Cu^{2+} or Zn^{2+}) with the cHF peptide, we investigated its structural modifications before and after adding the reducing agent sodium borohydride using Field-Emission Scanning Microscopy.

Starting our investigation with copper metal, we witnessed the formation of remarkable structures from nanospheres measuring a diameter of 10 μm to flower-like structures with high surface-to-volume ratios.

Specifically, we noted that upon the addition of 0.5 mM $CuCl_2$, the formed fibrils exhibited a reduction in thickness and increased condensation. However, upon the addition of $NaBH_4$, substantial spherical structures (with diameters exceeding 10 μm) formed, composed of multiple rectangular segments (Figure 38).

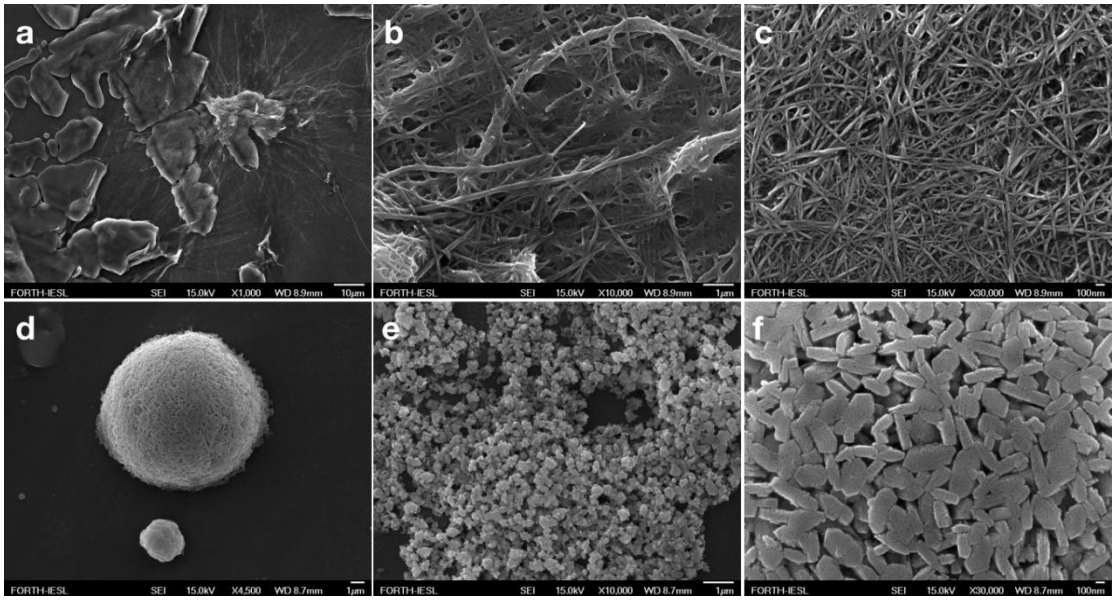

Figure 38: FESEM images of cyclo-(His-Phe) at the concentration of 5 mM in PBS 1X. a, b, c) with 500 μM $CuCl_2$ (eq. 0.1) Time of incubation: 7 days. d,e,f) after the addition of $NaBH_4$.

Upon the addition of 1 mM of copper ions, the sheet-like structure was apparent (Figure 39). Likewise, the addition of 2.5 mM $CuCl_2$ led to the formation of these "flower-like" structures comprised of nanosheets giving the appearance of petals. Upon reduction, the arrangement of nanosheets appears denser and more organized (Figure 40).

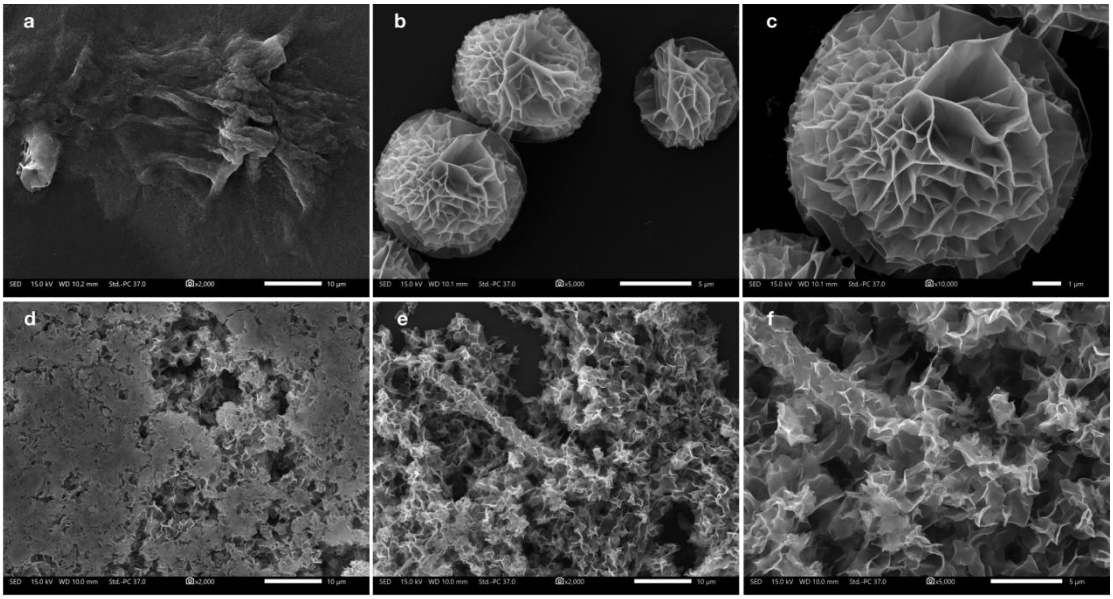

Figure 39: FESEM images of cyclo-(His-Phe) at the concentration of 5 mM in PBS 1X. a, b, c) with 1 mM $CuCl_2$ (eq. 0.2) d,e,f) after the reduction.

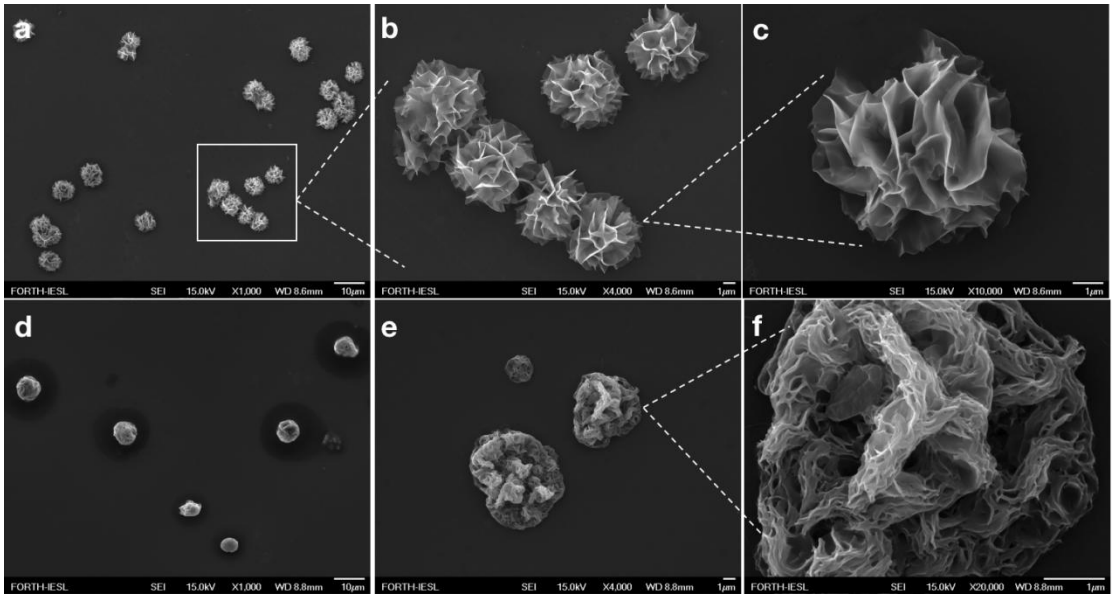

Figure 40: FESEM images of cyclo-(His-Phe) at the concentration of 5 mM in PBS 1X a,b,c) 2.5 mM $CuCl_2$ (eq. 0.5). Time of incubation: 7 days. d,e,f) after the addition of $NaBH_4$. Time of incubation: 24 hours.

When the concentration of $CuCl_2$ reached 5 mM, we noted the formation of fibrils that assembled into networks or flower-like structures across various sections of the sample. Additionally, upon introducing the reducing agent $NaBH_4$, there emerged substantial spherical structures, seemingly comprised of sheet-like components.

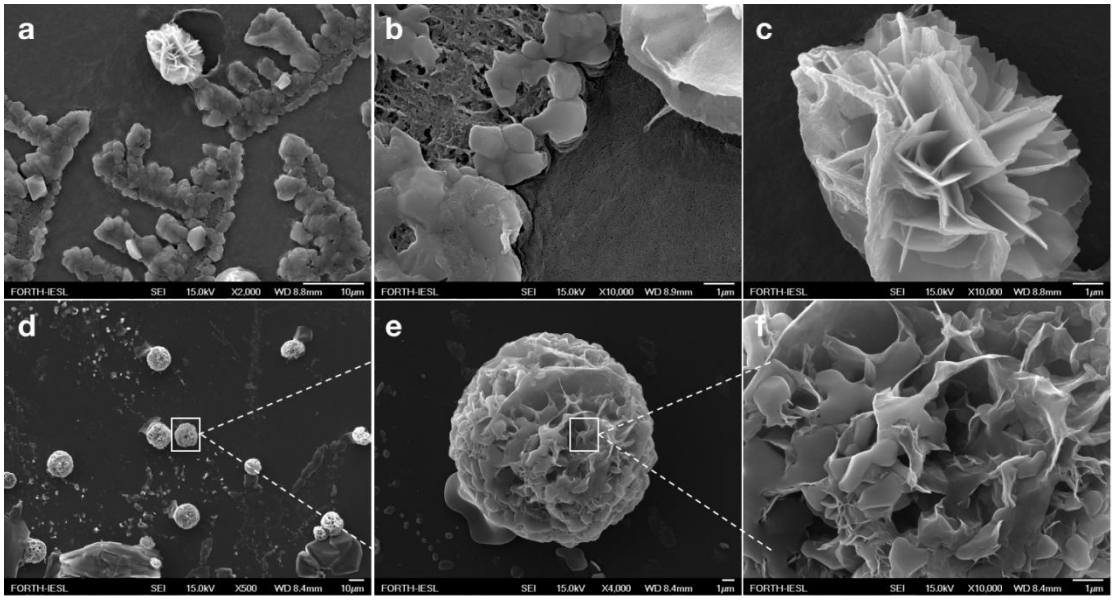

Figure 41: FESEM images of cyclo-(His-Phe) at the concentration of 5 mM in PBS 1X a,b,c) 5 mM $CuCl_2$ (eq. 1). Time of incubation: 7 days. d,e,f) after the addition of $NaBH_4$. Time of incubation: 24 hours.

Through a thorough investigation of these conditions and the careful observation of the alterations in the cyclic peptide's structure, we documented substantial structural modifications suggesting that these were induced by the binding of the metal to the peptide molecules.

To provide additional validation for our hypothesis, we present the following supporting data. Very low copper concentrations were tested (50 µM and 5 µM) and demonstrated no impact on the initial fibril formation of the cyclic peptide, although finer fibrils were formed with 50 µM copper (Figure 42).

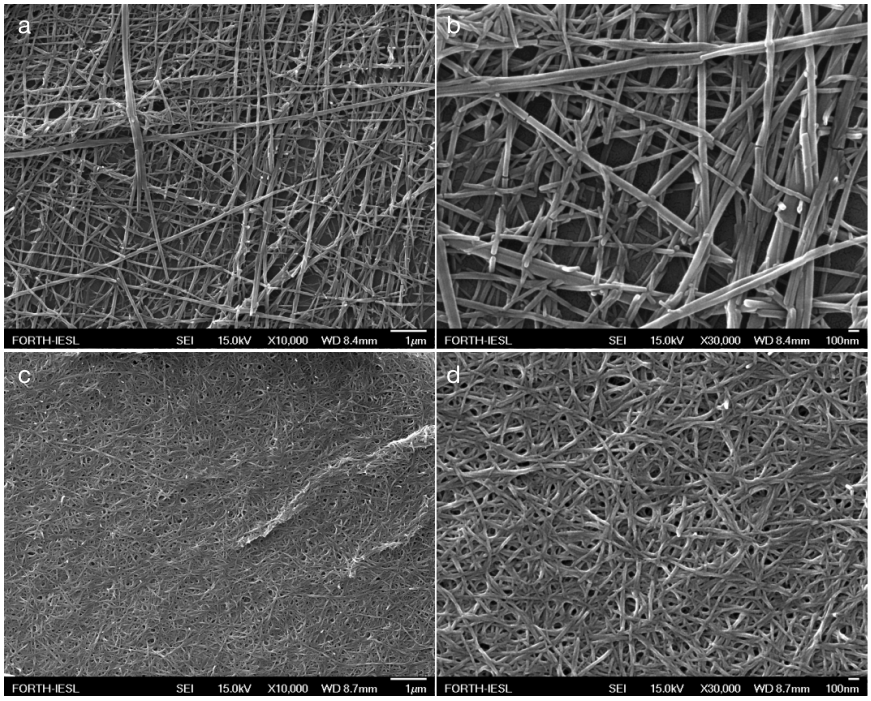

Figure 42: FESEM images of cyclo-(His-Phe) at the concentration of 5 mM in PBS 1X a, b) with 50 μM $CuCl_2$ (ratio 1:100) c, d) after the reduction.

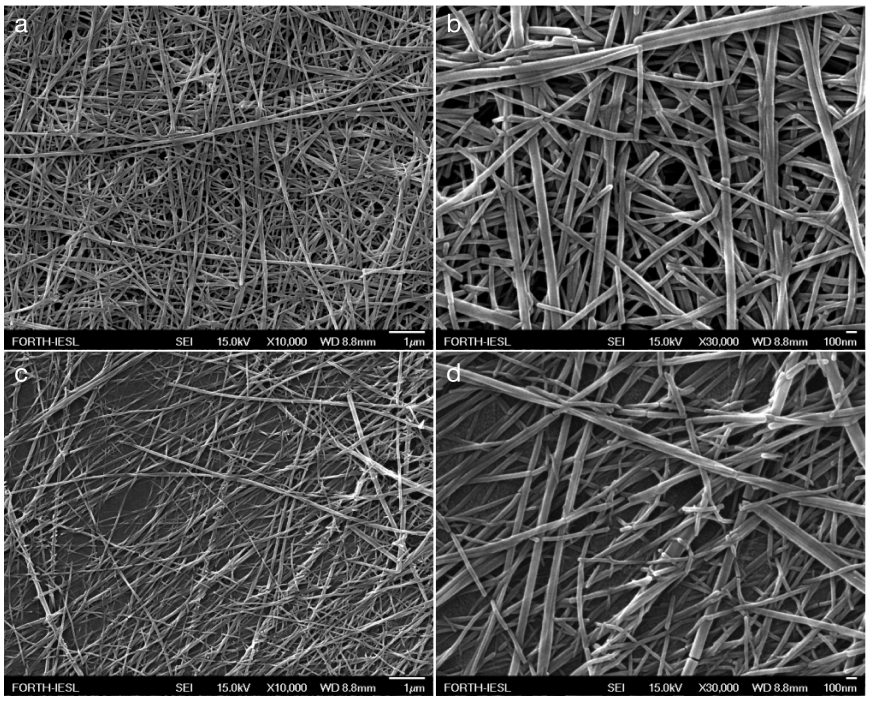

Figure 43: FESEM images of cyclo -(His-Phe) at the concentration of 5 mM in PBS 1X a, b) with 5 μM $CuCl_2$ (ratio 1:1000) c, d) after the reduction.

At the outset, noticeable morphological alterations of the cyclo-(His-Phe) peptide were detected upon the addition of the zinc chloride, both prior to and following reduction. These observations confirm our initial hypothesis that the coordination of the peptide with zinc ions is feasible, similar to the one observed with copper. A

predominant characteristic of all structures obtained from the presence of zinc is spherical formations. Even the lowest amount of zinc (0.5 mM), is clearly responsible for the appearance of spherical nanostructures alongside the presence of fibrils (Figure 44).

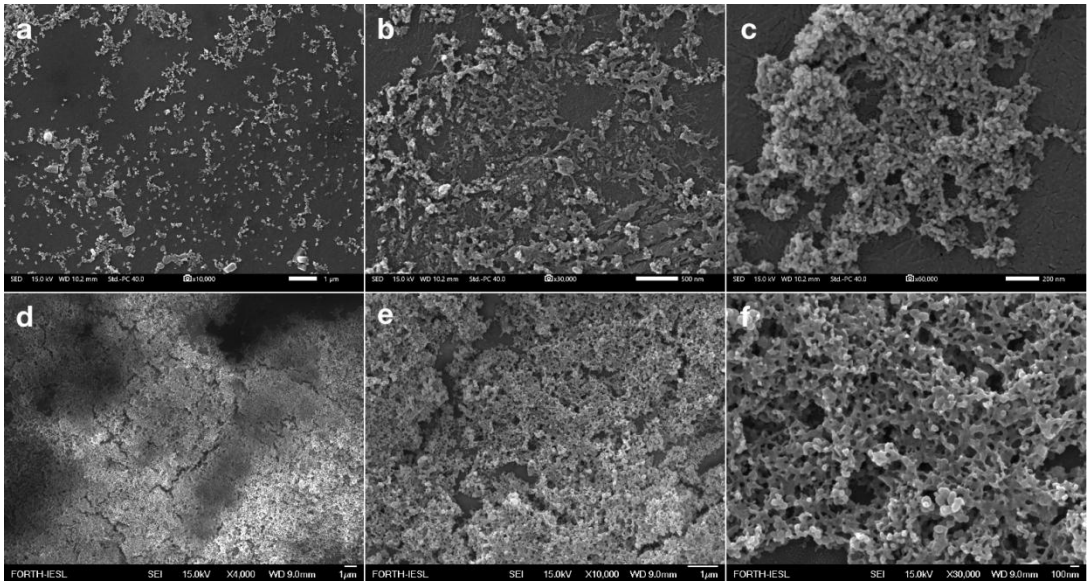

Figure 44: FESEM images of cyclo-(His Phe) at the concentration of 5 mM in PBS 1X a, b, c) 0.5 mM ZnCl2, d, e, f) after the reduction.

Similarly, a small concentration increase (1 mM) continues to exhibit limited influence on the morphology, although more well-defined spherical structures start to emerge in the absence of fibrillar arrangements.

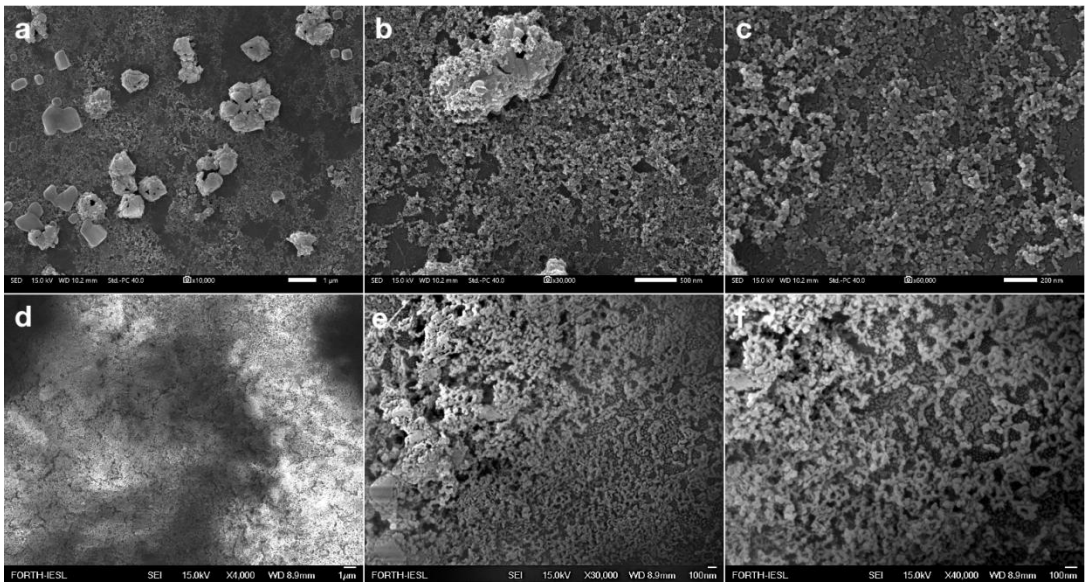

Figure 45: FESEM images of cyclo-(His-Phe) at the concentration of 5 mM in PBS 1X a,b,c) 1 mM $ZnCl_2$ d,e,f) after the reduction.

Nevertheless, when the addition is gradually increased to 0.5 and 1 ratio of the peptide, less structured nanoforms become apparent. It's noteworthy that the addition of the reducing agent sodium borohydride improved the structural formation, resulting in the emergence of significantly more well-defined spherical structures.

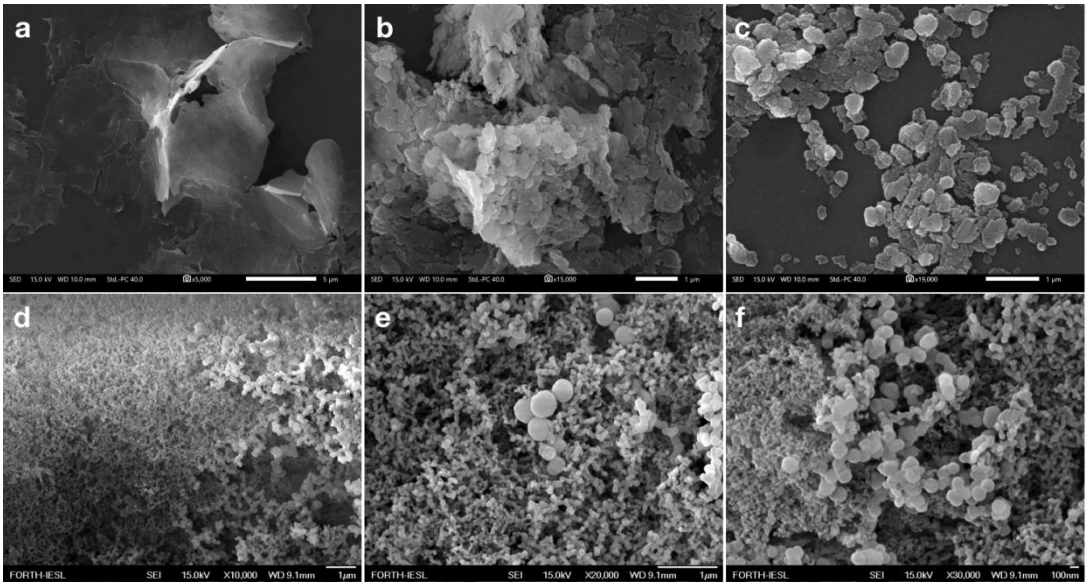

Figure 46: FESEM images of cyclo-(His-Phe) at the concentration of 5 mM in PBS 1X a, b, c) 2,5 mM Zinc (Ratio Peptide: $ZnCl_2$ 2:1) before $NaBH_4$ d, e, f) after the reduction.

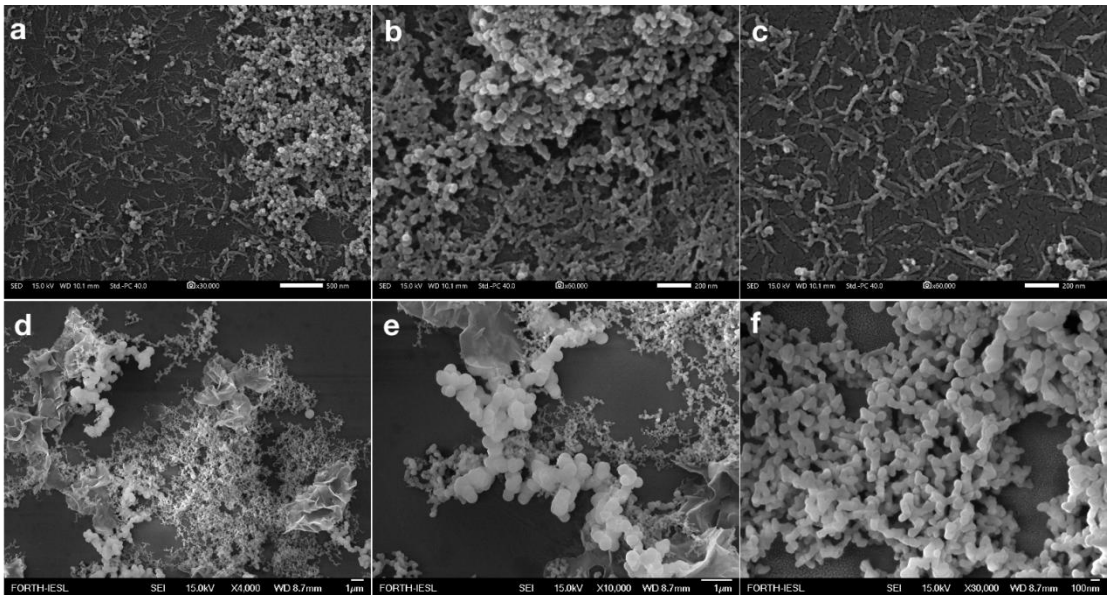

Figure 47: FESEM images of cyclo-(His Phe) at the concentration of 5 mM in PBS 1X a, b, c) 5 mM $ZnCl_2$, d, e, f) after the reduction.

Furthermore, in order to verify the active role of the peptide to the formation of NPs, we conducted TEM microscopy observations. In the Figure 48 (a,b) the Zn NPs at the concentration of 1 mM zinc appeared smaller and predominantly amorphous,

while the figures 48 (c, d) confirmed the active role of cHF peptide in the formation of the NPs as an outer layer of the structrures..

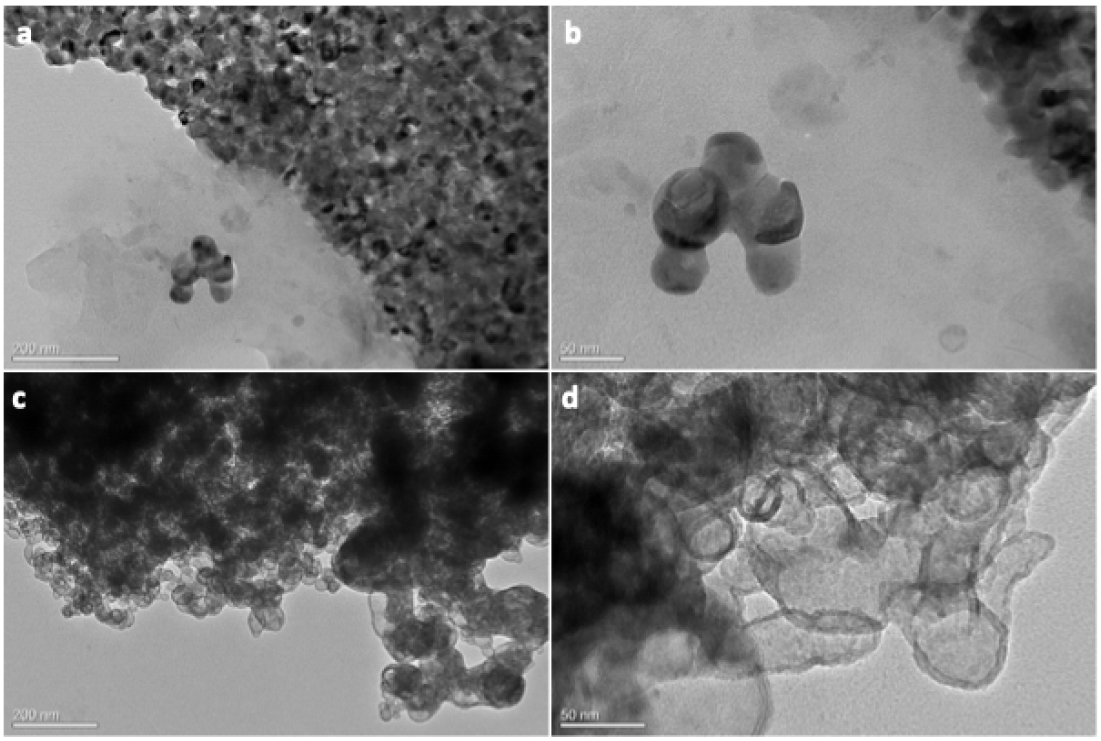

Figure 48: TEM images of a,b) ZnO NPs at the concentration of 1 mM without peptide, c,d) cycloHF-ZnO at the concentration of 1 mM.

5.3.3 EDX Analysis

After conducting microscopic examinations of our samples, we proceeded with EDX (Energy-Dispersive X-ray Spectroscopy) analysis to confirm the presence of metal ions in our synthesized cHF-NPs. Figures 49 (upper) depict the regions where EDX was performed, revealing pronounced peaks corresponding to the Copper (Cu) and Oxygen (O) elements that constitute the inorganic phase. Figures 49 (bottom) shows the image where the EDX was taken and highlights the intense peaks of Zinc (Zn) and oxygen (O) elements.

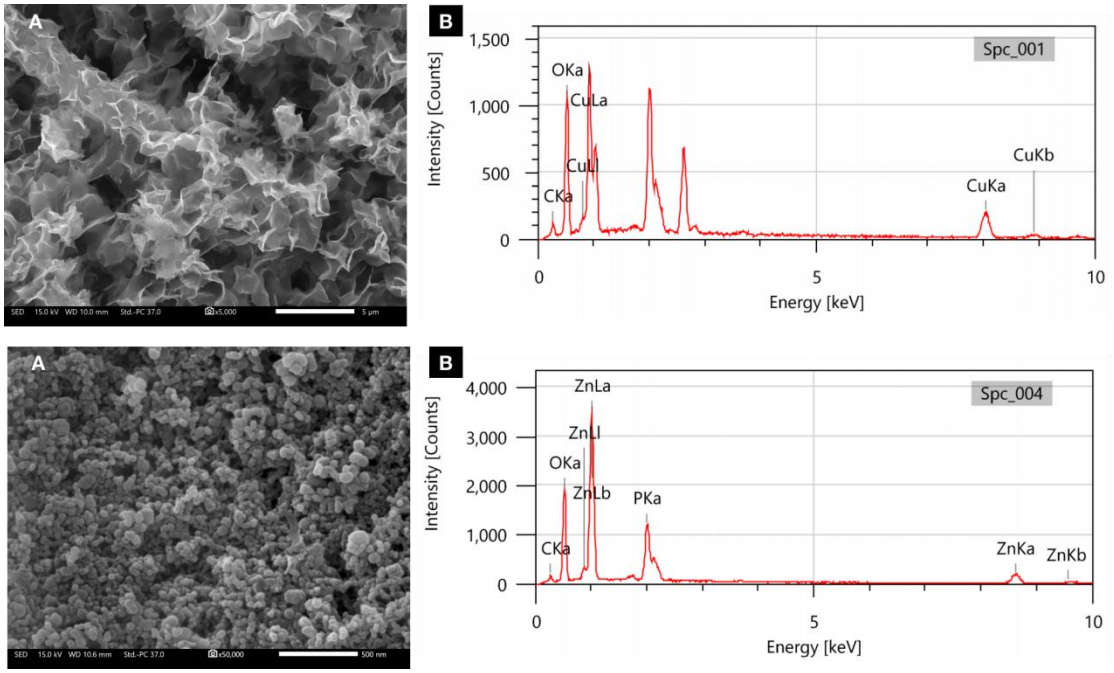

Figure 49: A) Area of EDX analysis of cyclo–(His-Phe) in PBS 1X B) EDX analysis spectra. Upper image: cHF-Cu^{2+} NPs of 1 mM, Bottom Image: cHF-Zn^{2+} NPs of 1 mM.

5.3.4 Fourier transforms infrared spectroscopy (FTIR) analysis of cHP NPs.

The coordination of the cyclo-(His-Phe) peptide with copper and zinc ions and the subsequent formation of NPs was analyzed by solid-state Fourier transform infrared (FTIR) spectroscopy. The spectra were recorded from 5000 to 400 cm^{-1}.In particular the stretching mode of the C=O groups in the amide I region of the peptide backbone can be highly diagnostic for different types of secondary structure, such as α-helices and β-sheets (194). A comparison between FTIR spectra of peptide powder cyclo-(His-Phe) and the self-assembled cHF after lyophilization is shown in Figure 50. For the peptide powder (orange line), the maximum of the amide I band is at 1658 cm^{-1}. In contrast, the self-assembled cHF (blue line) produces a red-shifted band at ~1668 cm^{-1}, indicating the peptide's assembly into a well-organized structure.

.

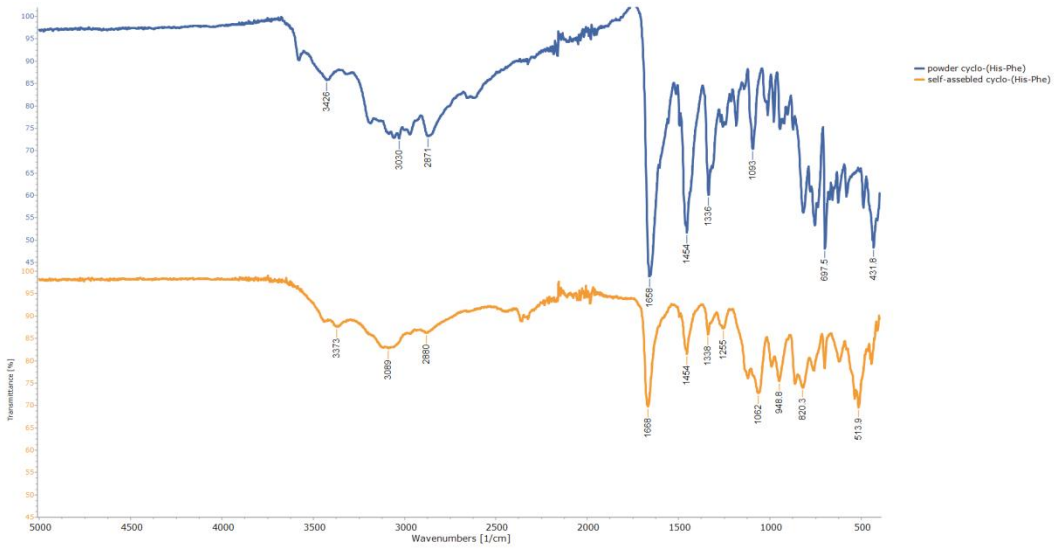

Figure 50: FTIR spectra of cyclo-(His-Phe). Blue line corresponds to peptide powder and orange line corresponds to self-assembled peptide.

The FTIR spectrum of the self-assembled peptide cyclo-(His-Phe) present a band around 3373 cm^{-1} corresponding to the N-H stretching vibration, and the band at 3089 cm^{-1} can be attributed to the C-H stretching vibration of the imidazole ring of histidine amino acid. The amide I band between the wavenumbers 1700 - 1600 cm^{-1} is attributed to the carbonyl (C=O) stretching vibration of the peptide bond. Therefore, it is the diagnostic region for peptide secondary structure, and the peak at 1668 cm^{-1} can be attributed to forming a beta-sheet structure (195,196). Moreover, the bands at 1454, 1338, 1255, and 1062 cm^{-1} correspond to the imidazole group's C-N stretching and N-H bending modes, as Celik described. Additionally, the band at 513 cm^{-1} corresponds to the bending vibration of the N-H group (197).

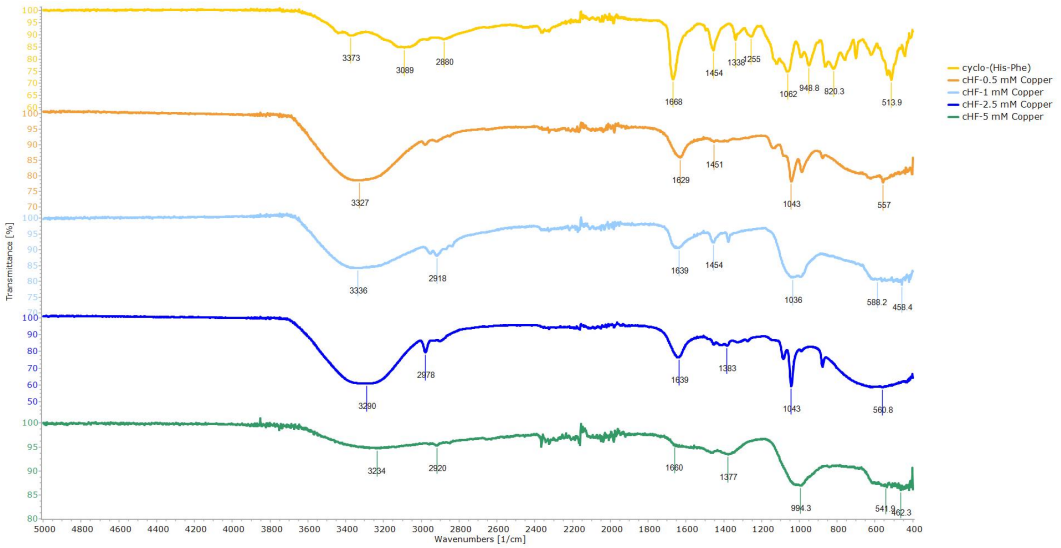

Figure 51: FTIR spectra of cyclo-(His-Phe)-CuO NPs.

The increased addition of copper and zinc ions (0.5, 1, 2.5, and 5 mM) shifts the 3373 cm^{-1} band of the cHF at 3327, 3336, 3290, 3234, and 3350, 3317, 3353, and 3257 cm^{-1}, respectively. This shift indicates the coordination of the metals to the histidine amino acid and, that higher metal concentrations cause a more considerable shift (around 100 to 130 cm^{-1}) (198). In both cases, the peak between 3350 to 3200 cm^{-1} presented broader after the addition of metal ions. This is caused by the O-H group of H_2O on the surface of the nanostructures and, subsequently, the formation of NPs (199).

Moreover, the band at 1668 cm^{-1} was shifted to 1640, 1642, 1642, 1654 $cm^{-1,}$ and 1629, 1639, 1639, and 1660 cm^{-1}, respectively, with increasing copper and zinc ion concentrations. Noteworthy is that the addition of low ion concentration (0.5 mM) shifts the amide I band toward lower frequency, reflecting an increase in hydrogen bonding due to the rise in ordered secondary structure (200). However, the increased amounts of metal ions do not shift the wavelength significantly, meaning that they do not give rise to more packed beta-sheets but contribute to the observed spherical formations. We validated the configuration modifications via our observations using FESEM microscopy. As an example, the addition of a small quantity of copper ions led to the formation of a more refined and compact fibril network (as depicted in Figure 42 c,d). Conversely, an excessive amount produced spherical formations (as evidenced in Figure 38 c,d,e). Also, the shift or the absence of the bands 1454, 1338, and 1255 cm^{-1} might indicate the contribution of the cHF as a stabilizing agent and its modification during the formation of metal particles. Lastly, the formation of metal complexes caused the band shifts at 1062 cm^{-1} between 20 to 60 cm^{-1} (198). The shift of the sharp peak at 513 cm^{-1} indicates the coordination of histidine with Cu and Zn because it corresponds to N-H vibration. Additionally, the band becomes broader and weaker in high concentration of metals. Moreover, the increased amount of zinc ions led to a new broad peak at 563 cm^{-1}, which can be attributed to the stretching/vibration of the metal–oxygen bond in Zn–O due the formation of ZnO NPs (190,201).

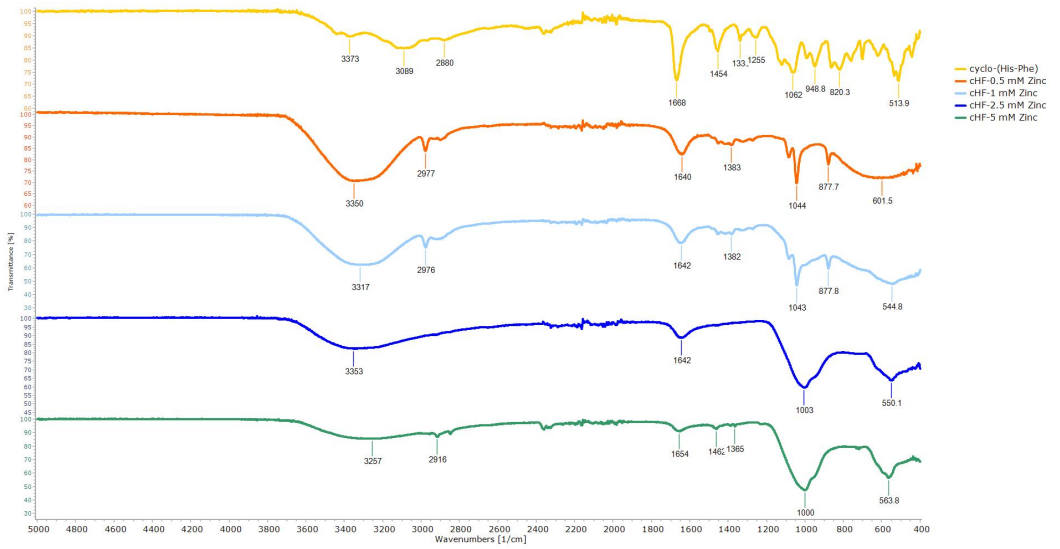

Figure 52: FTIR spectra of cyclo-(His-Phe)- ZnO NPs.

5.3.5 Antibacterial activity of the cHF peptide based-metal nanoparticles

The FTIR method confirmed the ability of the cyclo-(His-Phe) to coordinate successfully with the histidine, leading to the efficient formation of Cu and Zn complexes.

The cyclic dipeptide cyclo-(His-Phe) and its cyclo-(His-Phe) - Cu^{2+}, and cyclo-(His-Phe) - Zn^{2+} NPs were tested against the Gram-negative bacteria *E. coli* and Gram-positive bacteria, *S. aureus*. In both cases, the cHP peptide didn't show any antimicrobial effect. However, the antimicrobial effectiveness of these ions can be affected, when they form complexes with the peptides (202).

The antimicrobial efficiency of cHF-metal NPs showed a concentration dependence.

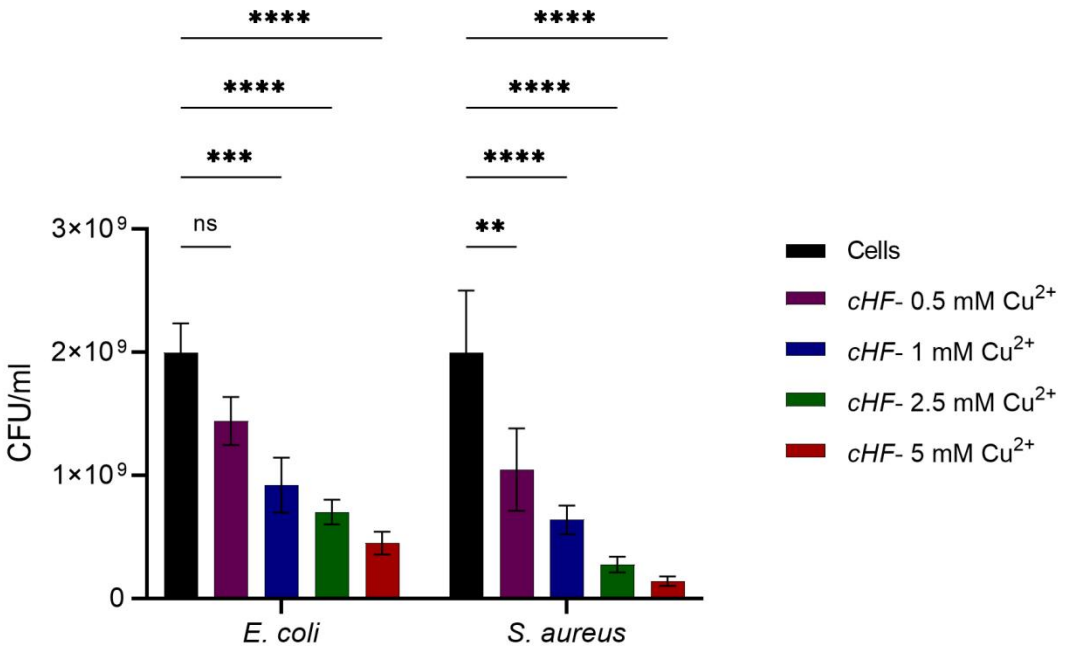

Figure 53:The CFU/mL diagram of *E. coli* and *S. aureus* treated with the cyclo-(HF)-Cu^{2+} NPs. *p≤0.05, **p≤0.01, ***p ≤0.001, ****p<0.000. The values represent means ± standard deviations of triplicates of three independent experiments (n = 9). Two-way ANOVA.

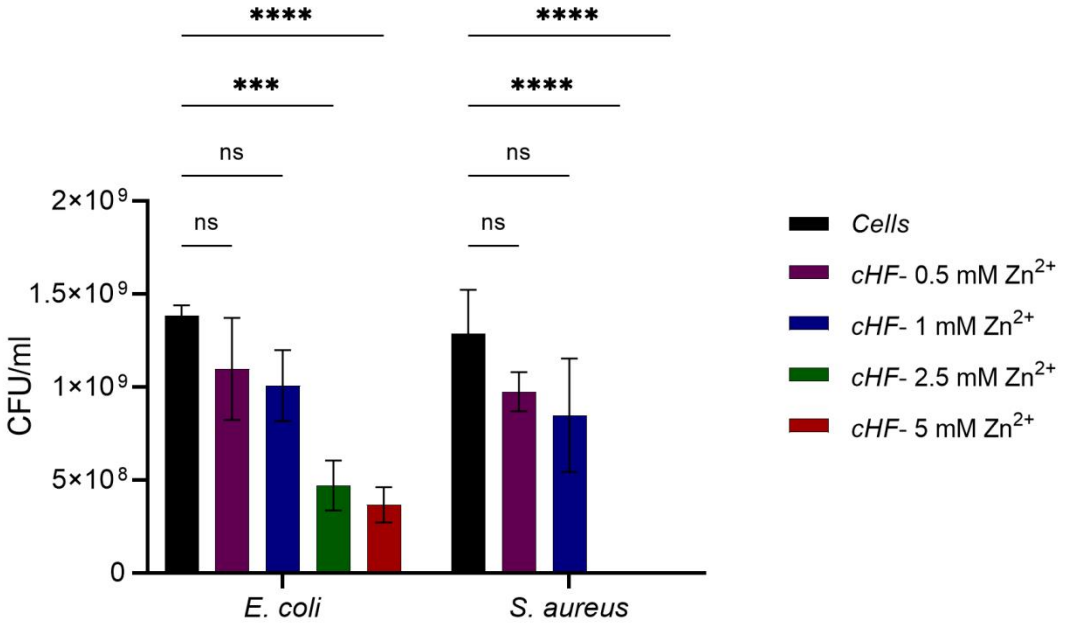

Figure 54: The CFU/mL diagram of *E. coli* and *S. aureus* treated with the cyclo-(HF)-Zn^{2+} NPs. *p≤0.05, **p≤0.01, ***p ≤0.001, ****p<0.0001. The values represent means ± standard deviations of triplicates of three independent experiments (n = 9). Two-way ANOVA.

5.3.6 *In vitro* cytotoxicity

The low cytotoxicity of nanoparticles (NPs) on human cells is a crucial requirement for employin NPs in antibacterial applications. Hence, we carried out cytotoxic activity tests on the human fibroblast L929 cell line to evaluate the biocompatibility of the CuO NPs and ZnO NPs with mammalian cell lines. This assessment will determine their potential use as therapeutic agents with antimicrobial activity.

The peptide cyclo-(His-Phe) does not affect the cell viability of the fibroblast L929 cell line. However, in the presence of 1 and 0.5 equivalent of Cu^{2+} or Zn^{2+} at the formed cHF-Cu^{2+} and cHF-Zn^{2+} NPs, there is high cytotoxicity and no survival rate (the data not shown). As we speculate, their increased cytotoxicity is a result of H_2O_2 production. However, the addition of the cHF-Cu^{2+} and cHF-Zn^{2+} NPs (eq. 0.1 and 0.2) at lower metal concentrations did not affect statistically significantly the survival of L929 cell line at 24 h and 48 h (Figure 55). It is worth noting that the observed slightly increased viability of the cells at the 48 hours, maybe suggests that there is a partial release of the metals within the first 24 hours, and therefore the cells are less exposed to the effect of the metal (Figure 56).

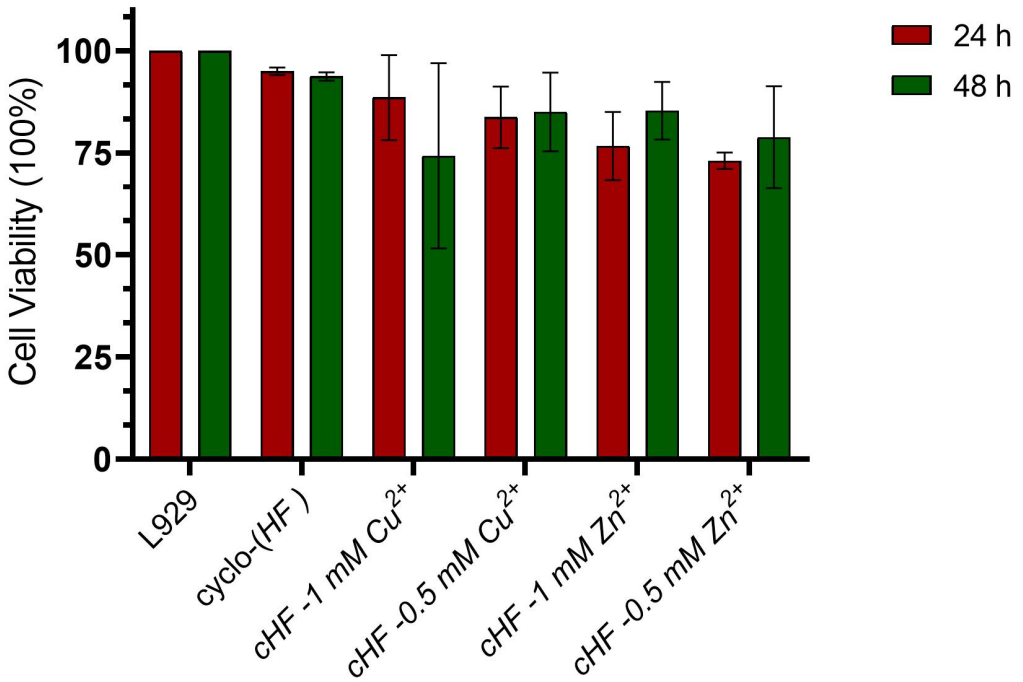

Figure 55: Thiazolyl blue tetrazolium bromide (MTT) cell viability assay results of the cHF peptide, cHF-CuONPs and cHF-ZnO NPs incubated for 24 h and 48 h in the L929 fibroblasts.

The values represent means ± standard deviations of triplicates (n = 9). *p≤0.05, **p≤0.01, ***p ≤0.001, ****p<0.0001. Two-way ANOVA.

5.3.7 Anti-cancer activity of the metal NPs capped with cHF

Many studies have shown that there is a strong link between copper or zinc ions and cancer cells. The cHF-Cu^{2+} and cHF-Zn^{2+} NPs represent a promising addition of a new class of compounds as metal-based drugs. Next, we carried out cell viability experiments on the MG-63 osteosarcoma cell line, in order to study the anticancer properties of the prepared metal NPs.

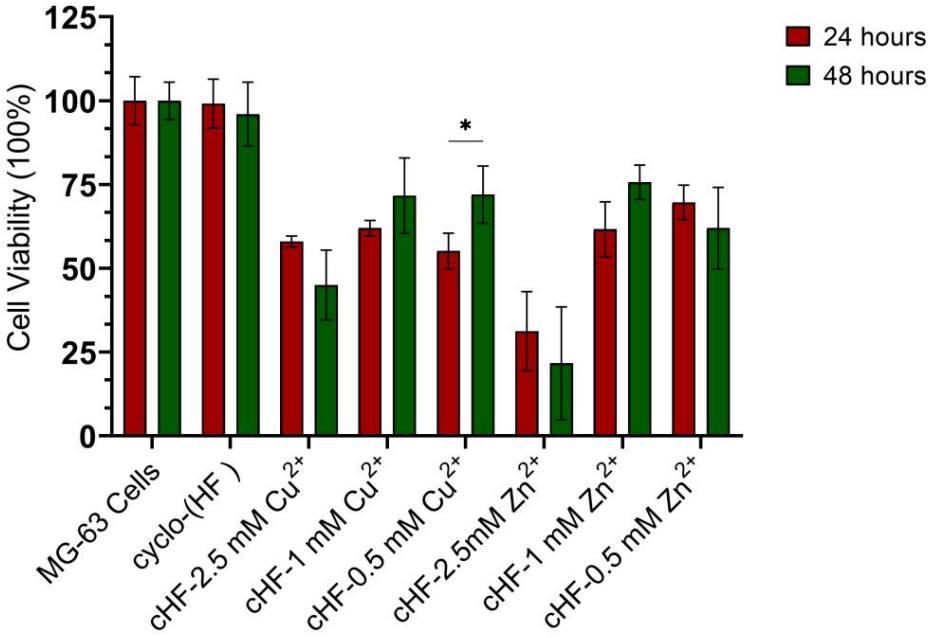

Figure 56: Thiazolyl blue tetrazolium bromide (MTT) cell viability assay results of the cHF peptide, cHF-CuO NPs and cHF-ZnO NPs incubated for 24 h and 48 h in MG-63 osteosarcoma cells at pH 7.4. The values represent means ± standard deviations of triplicates of two independent experiments (n = 6). *p≤0.05, **p≤0.01, ***p ≤0.001, ****p<0.0001. Two-way ANOVA

The *in vitro* anticancer efficacy of the cHF-CuO NPs and cHF-ZnO NPs was studied in MG-63 osteosarcoma cancer cells at pH 7.4 with the MTT assay. Cyclo-(His-Phe) peptide by itself does not affect the cell viability of the MG-63 cell line. However, the cHF- Cu^{2+} and cHF - Zn^{2+} NPs affect the cell viability in a certain way. In the presence of 1 equivalent of Cu^{2+} or Zn^{2+}, there is no cell survival at 24 and 48 hours (data not shown). Although decreasing the Cu^{2+} or Zn^{2+} equivalents two fold, we noticed a difference in the survival depending on the metal ion. The cHF- Zn^{2+} complex has shown a more potent effect against the MG-63. The presence of cHF-

Zn^{2+} NPs reduced the cell survivability by 28 %, while the presence of cHF–Cu^{2+} NPs 58 %. However, our results show that the difference is minor when the complexes with 0.5 and 1 mM of Cu^{2+} or Zn^{2+} were tested. In particular, the survival of the cells in all cases was around 60% within the first 24 hours. Interestingly, the survival rate did not change significantly at 48 h, in most concentrations similar to our tests on fibroblast cells. This observation further supports our hypothesis that the metal ions must be fully released within 24 hours.

Our *in vitro* conditions fail to replicate the conditions of tumor microenvironment, like acidosis, and hypoxia (184). Therefore, to mimic the requirements of a cancerous environment in vitro, we decreased the pH to 6.4. Under acidic conditions, the imidazole ring of histidine in the peptide's backbone gets protonated; thus, the release of metal ions is higher. At physiological pH, all the studied complexes with equivalents of metals 0.1 and 0.2 (0.5 and 1 mM) reduced the survival rate to 52 to 60% within 24 hours. Surprisingly the survival rate decreased by an additional 40% when the cells were treated with cHF-Cu^{2+} NPs (0.5 mM), while the survival rate decreased to 10% after the treatment with cHF-Zn^{2+} (1 and 0.5 mM).

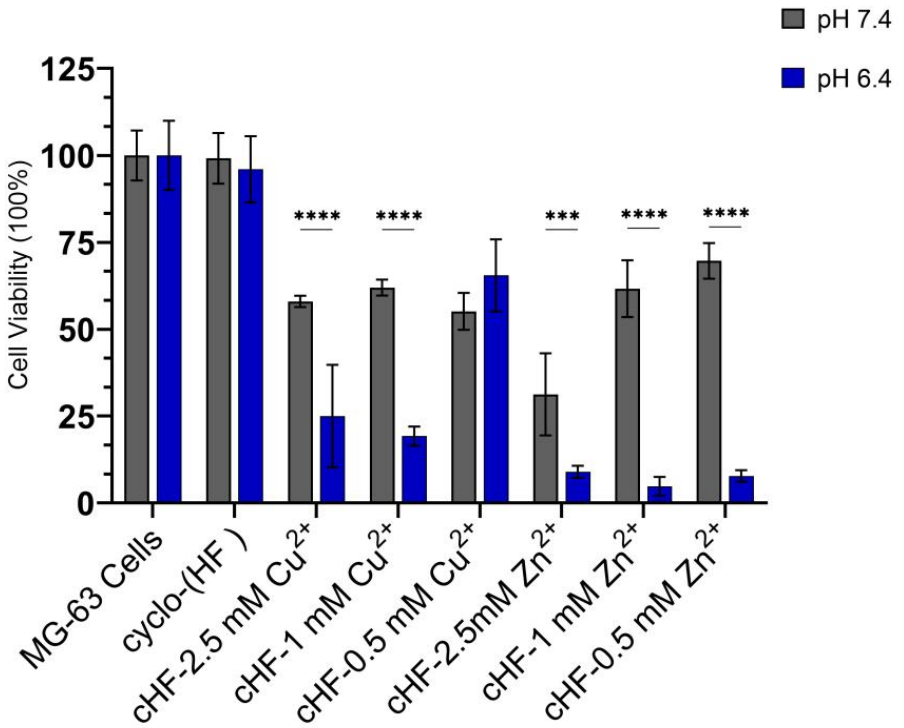

Figure 57: Thiazolyl blue tetrazolium bromide (MTT) cell viability assay results of the cHF and cHF-complexes incubated for 24 h in **MG-63** osteosarcoma cells at at pH 6.4 compared to the ones incubated at pH 7.4. Results are expressed as a percentage value of control cells cultured without the addition of peptides (control = 100%). *p≤0.05, **p≤0.01, ***p ≤0.001, ****p<0.0001.Two-way ANOVA

On a more direct approach, MG-63 osteosarcoma cells were seeded for 24 h at 24-well plate at pH 6.4 before the cHF NPs were added. The cells were incubated at 37 °C for 24 h to evaluate the effect of the complexes on the cells (Figure 58a). After incubation, the samples were fixed with paraformaldehyde, dehydrated, and placed for FESEM observation. The images show that the cHF–CuO NPs and cHF –ZnO NPs (1 mM) led to a decrease in the number of cells on the cover slip. Furthermore, these cells appeared highly distorted, suggesting cell damage or death (Figure 58c, d).

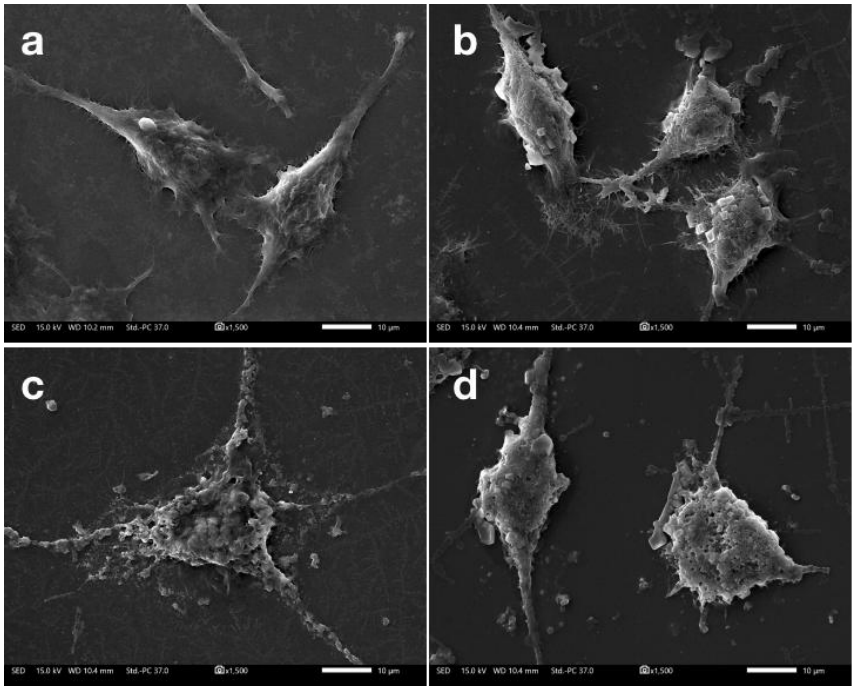

Figure 58: FESEM Images of the MG-63 cell line at pH 6.0 a) untreated, b) cyclo-(His-Phe) c) cyclo-(His-Phe) – 1 mM Cu^{2+} d) cyclo-(His-Phe) – 1 mM Zn^{2+} complexes.

Alongside the FESEM observations, we performed EDX analysis to detect metal ions on the cells, indicating the cause of the cell damage to the cell. Indeed, as shown in Figure 59, it has confirmed the presence of metal ions on the cell surface, indicating that metal ions are responsible for the disrupted cell membranes.

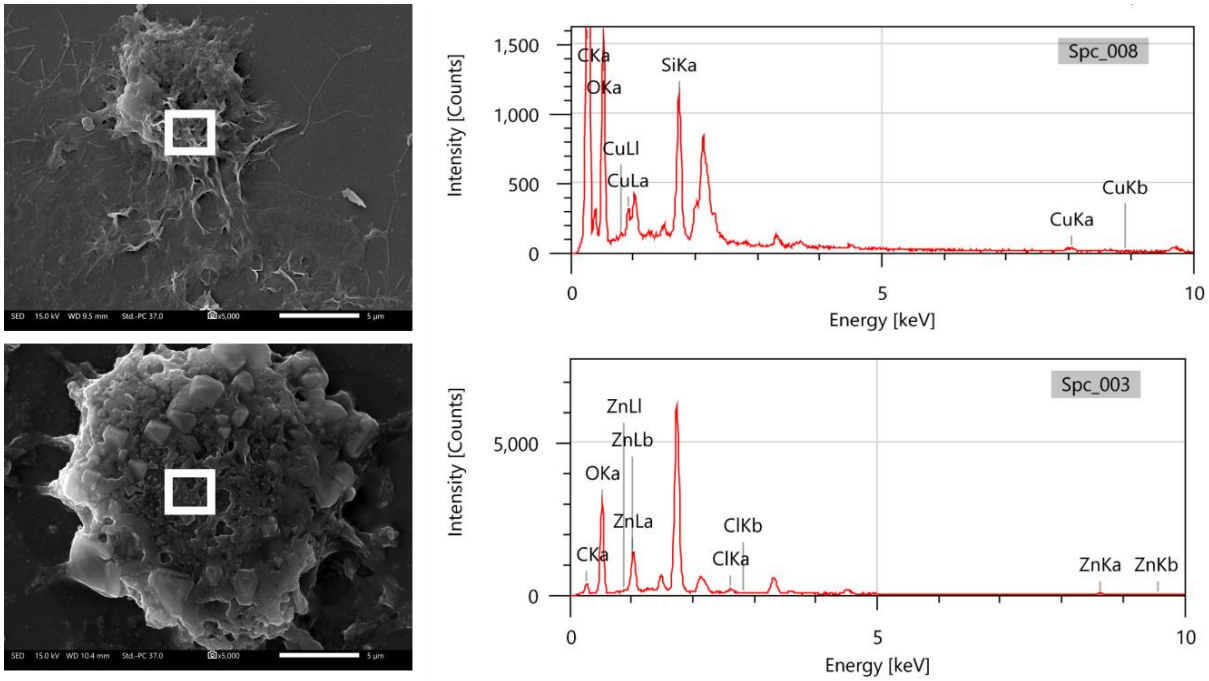

Figure 59: EDX analysis on the MG-63 osteosarcoma cells after they were treated with cHF-Cu $^{2+}$ (1 mM) (upper line) cHF-Zn $^{2+}$ (1 mM) (bottom line).

5.4 Discussion

The pursuit of understanding the interaction of peptides with metal ions, particularly within the context of cyclic peptides, has evolved into an exciting domain that still needs to be explored. Our focus on the cyclic-peptide sequence, specifically cyclic-(His-Phe), was driven by its intrinsic propensity, owed to the histidine residue, to engage in high-affinity binding with metal ions like Cu (II) and Zn (II) as well as by the previously reported antitumor and antimicrobial activity of the cyclic-(His-Phe) itself (203).

The cHF exhibits a fibrillar morphology upon its dissolution in PBS 1X, where FESEM and Congo Red staining assessed the characteristic amyloid fibrils. Our subsequent experiments affirmed the peptide's ability to chelate metal ions, specifically zinc, and copper, leading to the successful synthesis of CuO NPs and ZnO NPs. Through FESEM imaging, it was discrete that the capping with the cHF exerts a modulatory effect on morphology, particle size and distribution (201).

Many morphologies involving structures such as nanoparticles, nanorods, nanotubes, nanobelts, nanoplates, nanorings, and even intricate designs like nanoflowers have been described in recent years (204).

Intriguingly, the cHF-CuO NPs have led to the formation of flower-like structures consisting of thin nanosheets. Such configurations of Copper Oxide Nanostructures have previously been synthesized by Siddiqui et al., employing “green” chemistry (192) . In contrast, the cHF-ZnO NPs showed spherical morphologies with heterogeneous size distribution, where increased concentrations of zinc ions led to enlarged sphere diameter. Furthermore, we completed the characterization of cHF-ZnO NPs and cHF-CuO NPs by FTIR spectroscopy

As previous studies suggested, these morphological variations can substantially influence the antimicrobial activity of nanoparticles (59) . Several studies, including one by Nejad, have indicated that the particle's shape and size can influence the antibacterial activity of copper NPs (59). Among these, the flower-like Cu/CuxO NPs proved to be the most potent due to their larger surface area and different crystal structure, which can affect various cellular components of microbial cells (205).

Indeed, the flower-like structured cHF-CuO NPs displayed a concentration-dependent bacteriostatic activity. Specifically, against *E. coli,* the bacteriostatic activity ranged from 20% to 70%, while against *S. aureus*, it varied between 5% to 50%. These results demonstrate that as the concentration of these nanoparticles increased, their antibacterial efficacy also increased. Likewise, the antimicrobial effectiveness of CuO nanoparticles in the 100 to 5000 mg/ml concentration has also been confirmed against *S. aureus* and *E. coli* by Ren (206). Moreover, prior research has indicated that copper nanoparticles exhibit higher efficacy against Gram-positive than Gram-negative, due to the cell wall compositions (179) . The Gram-positive bacterium possesses a thick peptidoglycan layer, which may allow easier penetration by Cu ions. In contrast, the Gram-negative bacterium has an outer membrane covering the thin layer of peptidoglycan on the outside, acting as a barrier against Cu ion penetration (207).

Similar to CuO NPs, the cHF-ZnO NPs are more active against gram-positive bacteria (192). Hence, the particle size is a crucial factor influencing the antimicrobial efficiency (181). In fact, the ZnO NPs (eq. 1 and 0.5), with a similar mean size of 18 nm, showed a bacteriostatic action against *E. coli* and a notable bactericidal response against *S. aureus*. In contrast, at lower concentrations of cHF-ZnO NPs (mean size 9

nm), both bacterial strains exhibit approximately 70% cell viability. *Gudkov et al*., suggested that

the ZnO NPs, when synthesized using "green" chemistry methods, exhibit optimal antimicrobial activity against both E. *coli*, and *S. aureus,* when the nanoparticle size is about 100 nm (181) . Therefore, the increased size combined with the increased ion concentration of NPs may explain the influence on microbial strains.

Finally, we reported that the peptide cyclo (His-Phe) did not show a notable antibacterial effect against *E. coli* and *S. aureus*. On the contrary, McCeland and his teamwork, following the Kirby-Bauer disc-diffusion method, showed that cyclo-(His-Phe) exhibits higher effectiveness against Gram-negative bacteria and less activity against Gram-positive at the concentration of 250 μg/hole (203) . Furthermore, the cHF-ZnO NPs and the cHF-CuO NPs must demonstrate biocompatibility *in vitro* for therapeutic applications. ZnO and CuO NPs (5 and 2.5 mM) led to fibroblast cell line L929 cell death at high concentrations. However, cHF-NPs exhibit a cell viability of 75% after 48 hours of exposure, which makes them suitable for antimicrobial applications.

Concluding, while both NPs at higher concentrations of metal ions (5 mM and 2.5 mM) showcase high efficacy against bacterial strains, their pronounced cytotoxicity excludes them from therapeutic applications. On the other hand, cHF-ZnO NPs (1 and 0.5 mM) and cHF-CuO NPs (0.5 mM) may be biocompatible but lack significant antimicrobial potency. Remarkably, the cHF-CuO NPs (1 mM) strike a balance, exhibiting both biocompatibility and antimicrobial efficiency. This positions them as promising candidates for further *in vivo* investigations.

Over the past decade, nanocarrier-based drug delivery systems have been the subject of exhaustive research, presenting novel avenues for therapeutic interventions. Specifically, in the context of osteosarcoma (OS), these carriers have the potential to revolutionize treatment methods by enhancing drug targeting, improving treatment efficacy, and potentially reducing side effects (208).

In line with these advancements, we embarked on the experimental journey to assess the capabilities of our formed nanoparticles. Initially, the fibrillar structure of the cHF did not affect the cell viability of the MG-63 cancer cell line. In contrast, other studies showed a significant reduction in the growth of the cancer cell lines of HeLa, MCF-7,

WHCO3 at 1 mM (193). CuO NPs have demonstrated anticancer potential against various malignancies, but only one study has explored the application of chitosan-capped Cu NPs against osteosarcoma. Our findings indicated a comparable cell viability rate at a corresponding concentration. ZnO NPs decreased cell viability by around 60 % at physiological pH. The results highlighted a modest reduction in cell viability.

Notably, our experiments with CuO and ZnO NPs showed a pronounced effect when the pH of the cell culture decreased to 6.4 mimicking the TME. The CuO NPs significantly decreased the cell survival by an additional 30%, while ZnO NPs reduced the survival rate to 10%. This significant difference between Cu and Zn could be attributed to the higher solubility of ZnO NPs in cell culture media (Dulbecco), as Reed and his colleagues observed (209). Summarizing, the cHF peptide responds to environmental pH changes due to its imidazole group and releases increased amounts of metals on the target cells, highlighting the importance of responsive materials in anticancer treatments.

5.5 Conclusions

In summary, the study of cyclic peptides and their interaction with metal ions has revealed promising therapeutic potentials. Our research was focused on cyclic-(His-Phe) and evealed its capacity to bind with metals, leading to the synthesis of stable CuO and ZnO nanoparticles with distinct morphologies that influence antimicrobial and anticancer activity. While their potential against bacterial strains is evident, their cytotoxicity at higher concentrations challenges their eventual therapeutic use. Among our findings, cHF-CuO nanoparticles at concentration of 1 mM, emerge as a promising candidate, demonstrating the subtle balance between biocompatibility and antimicrobial potency, underscoring the need for further exploring the optimal conditions towards biomedical applications.

6. General conclusions and Outlook

This dissertation provides a detailed investigation of the field of smart biomaterials, in particular peptides, and their responsiveness to various external stimuli such as light,

pH, and metals. The study highlights the importance of peptides due to their intrinsic ability to self-assemble, which makes them favorable for developing materials with adaptive responses.

In our research, we suggest the aromatic dipeptide Fmoc-FF as a promising light-responsive delivery system that showcases the potential of such peptide-based materials. This peptide has the ability to form hydrogels encapsulating specific chromophores, particularly cationic porphyrins, and thus induce antimicrobial properties. Our findings presented a possible approach for antimicrobial treatments applying a photodynamic way. Further research could expand the field of photodynamic therapy. For example, the influence of different wavelengths of light on these peptide-based hydrogels and the subsequent effects on cellular environments need to be studied. This research might pave the way for targeted and more efficient PDT applications.

In the next chapter, we synthesized fluorescent probes using histidine-containing peptide sequences, exploring the field of bioimaging. The successful coordination of peptide-porphyrin hybrids and their ability to penetrate HeLa cancer cells highlights the significant benefit of these fluorescent tracers in optical sensing and potentially improved therapeutic approaches for cancerous conditions. Subsequent studies could explore a broader range of peptide sequences that could be even more effective at entering cells. These peptides could be tested in multiple cancer cell lines, evaluating their efficacy in different cancers.

In the last chapter, the assembly of biocompatible nanoparticles, particularly those incorporating copper and zinc ions using cyclic-HF peptide, has opened avenues for effective antimicrobial and anticancer applications. The distinctive morphologies observed during the formation of these nanoparticles, combined with their demonstrated efficiency against bacterial strains and tumor environments, make a promising future for composite peptide-nanoparticle-based therapies. Observations of the distinct morphologies of nanoparticles formed with cyclic-HF peptide indicate a potential to manipulate their structures for specific therapeutic effects. Controlled studies focusing on altering the conditions and sequences for desired shapes and therapeutic outcomes are recommended.

Concluding, future studies could focus on the antimicrobial effects of the synthesized materials against select Gram-positive and Gram-negative bacterial strains, and a comprehensive study spanning a broader range of pathogens, including fungi and

viruses, could be undertaken. Finally, after the *in vitro* studies, *in vivo* experiments provide a more accurate representation of the therapeutic potentials of the developed materials, considering factors like bioavailability, metabolism, and excretion.

Summarizing these results not only highlight the versatility and potential of peptide-based smart biomaterials but also paves the way for the development of more targeted and effective biomedical applications in the future. This work will serve as an inspiration for further exploration and innovation in the exciting field of smart materials.

7. References

1. Du Z, Fan B, Dai Q, Wang L, Guo J, Ye Z, et al. Supramolecular peptide nanostructures: Self-assembly and biomedical applications. Giant. Elsevier B.V.; 2022;9
2. Alberts B, Johnson A, Lewis J, Raff M, Roberts K, Walte P. The Shape and Structure of Proteins. In: Molecular Biology of the Cell. 4th edition. New York: Garland Science; 2002.
3. Griffith EC, Vaida V. In situ observation of peptide bond formation at the water-air interface. PNAS. 2012;109(39):15697–701.
4. Sieber SA, Marahiel MA. Molecular mechanisms underlying nonribosomal peptide synthesis: Approaches to new antibiotics. Chem Rev. 2005;105(2):715–38.
5. Palomo JM. Solid-phase peptide synthesis: An overview focused on the preparation of biologically relevant peptides. Vol. 4, RSC Advances. 2014. p. 32658–72.
6. Hamley IW. Introduction to Peptide Science. John Wiley & Sons; 2020. 1–240 p.
7. Bouayad-Gervais S, St-Cyr DJ, Courcelles M, Bonneil É, Gohard FH, Thibault P, et al. Head-to-tail cyclization of side chain-protected linear peptides to recapitulate genetically-encoded cyclized peptides. Peptide Science. 2022 May 1;114(3).
8. Li X, Craven TW, Levine PM. Cyclic Peptide Screening Methods for Preclinical Drug Discovery. J Med Chem. 2022 65(18):11913–26.
9. Li DD, Wang Y, Kim E La, Hong J, Jung JH. Neuroprotective effect of cyclo-(L-pro-l-phe) isolated from the jellyfish-derived fungus aspergillus flavus. Mar Drugs. 2021 Aug 1;19(8).
10. Kwon YU, Kodadek T. Quantitative Comparison of the Relative Cell Permeability of Cyclic and Linear Peptides. Chem Biol. 2007 14(6):671–7.
11. Choe R, Il Yun S. Fmoc-diphenylalanine-based hydrogels as a potential carrier for drug delivery. E-Polymers. 2020;20(1):458–68.
12. Dougherty PG, Sahni A, Pei D. Understanding Cell Penetration of Cyclic Peptides. Vol. 119, Chemical Reviews. American Chemical Society; 2019. p. 10241–87.
13. O'Sullivan JJ, Uyeda KS, Stevenson MJ, Heffern MC. Investigation of metal modulation of oxytocin structure receptor-mediated signaling. RSC Chem Biol. 2023;4(2):165–72.
14. Costa L, Sousa E, Fernandes C. Cyclic Peptides in Pipeline: What Future for These Great Molecules Pharmaceuticals. Multidisciplinary Digital Publishing Institute (MDPI); 2023;16
15. Sun PD, Foster CE, Boyington JC. Overview of protein structural and functional folds. In: Current protocols in protein science . 2004.
16. Eisenberg D. The discovery of the-helix and-sheet, the principal structural features of proteins. 2003.
17. Lim YB, Lee M. Nanostructures of β-sheet peptides: Steps towards bioactive functional materials. J Mater Chem. 2008;18(7):723–7.
18. Carrasco ME. Hydrogen bond models for the simulation of protein folding and aggregation. 2012.
19. 'Lu W'. Encyclopedia of Nanotechnology . Buhshan B, editor. Springer; 2012. 2371–2382 p.
20. Yadav S, Sharma AK, Kumar P. Nanoscale Self-Assembly for Therapeutic Delivery. Front Bioeng Biotechnol. 2020;8.

21. Gazit E, Mitraki A. Plenty of Room for Biology at the Bottom An Introduction to Bionanotechnology. Second. Imperial College Press; 2013.
22. Mendes AC, Baran ET, Reis RL, Azevedo HS. Self-assembly in nature: Using the principles of nature to create complex nanobiomaterials. Wiley Interdiscip Rev Nanomed Nanobiotechnol. 2013 Nov;5(6):582–612.
23. Wang Y, Zhang W, Gong C, Liu B, Li Y, Wang L, et al. Recent advances in the fabrication, functionalization, and bioapplications of peptide hydrogels. Vol. 16, Soft Matter. Royal Society of Chemistry; 2020. p. 10029–45.
24. Tian X, Sun F, Zhou XR, Luo SZ, Chen L. Role of peptide self-assembly in antimicrobial peptides. Vol. 21, Journal of Peptide Science. John Wiley and Sons Ltd; 2015. p. 530–9.
25. Gelain F, Luo Z, Zhang S. Self-Assembling Peptide EAK16 and RADA16 Nanofiber Scaffold Hydrogel. Chem Rev. 2020;120:13434–60.
26. Zhao Y, Yang W, Chen C, Wang J, Zhang L, Xu H. Rational design and self-assembly of short amphiphilic peptides and applications. Vol. 35, Current Opinion in Colloid and Interface Science. Elsevier Ltd; 2018. p. 112–23.
27. Wang X, Zhang S, Zhang J, Wang Y, Jiang X, Tao Y, et al. Rational design of functional amyloid fibrillar assemblies. Chem Soc Rev. 2023;
28. Papanikolopoulou K, Schoehn G, Forge V, Forsyth VT, Riekel C, Hernandez JF, et al. Amyloid fibril formation from sequences of a natural β-structured fibrous protein, the adenovirus fiber. Journal of Biological Chemistry. 2005 280(4):2481–90.
29. Giorgetti S, Greco C, Tortora P, Aprile FA. Targeting amyloid aggregation: An overview of strategies and mechanisms. Vol. 19, International Journal of Molecular Sciences. MDPI AG; 2018.
30. Lee S, Trinh THT, Yoo M, Shin J, Lee H, Kim J, et al. Self-assembling peptides and their application in the treatment of diseases. Int J Mol Sci. 2019;20(23).
31. Fitzpatrick AWP, Debelouchina GT, Bayro MJ, Clare DK, Caporini MA, Bajaj VS, et al. Atomic structure and hierarchical assembly of a cross-β amyloid fibril. Proc Natl Acad Sci U S A. 2013 Apr 2;110(14):5468–73.
32. Rambaran R, Serpell L. Abnormal protein assembly. Prion. 2008;2(3):112–7.
33. Makin OS, Atkins E, Sikorski P, Johansson J, Serpell LC. Molecular basis for amyloid fibril formation and stability. 2005.
34. Bucciantini M, Nosi D, Forzan M, Russo E, Calamai M, Pieri L, et al. Toxic effects of amyloid fibrils on cell membranes: the importance of ganglioside GM1. The FASEB Journal. 2012;26(2):818–31.
35. Malik R, Wiedau M. Therapeutic Approaches Targeting Protein Aggregation in Amyotrophic Lateral Sclerosis. Vol. 13, Frontiers in Molecular Neuroscience. Frontiers Media S.A.; 2020.
36. Sunde M, Serpell LC, Bartlam M, Fraser PE, Pepys MB, Blake CCF. Common Core Structure of Amyloid Fibrils by Synchrotron X-ray Diffraction. 1997.
37. Lindgren M, Hammarström P. Amyloid oligomers: Spectroscopic characterization of amyloidogenic protein states. Vol. 277, FEBS Journal. 2010. p. 1380–8.
38. Yakupova EI, Bobyleva LG, Vikhlyantsev IM, Bobylev AG. Congo Red and amyloids: History and relationship. Vol. 39, Bioscience Reports. 2019.
39. Sulatskaya AI, Lavysh A V., Maskevich AA, Kuznetsova IM, Turoverov KK. Thioflavin T fluoresces as excimer in highly concentrated aqueous solutions and as monomer being incorporated in amyloid fibrils. Sci Rep. 2017;7(1).
40. Sunde M, Blake C. The structure of amyloid fibrils by electron microscopy and x-ray diffraction. Vol. 50, Advances in Protein Chemistry. Academic Press Inc.; 1997. p. 123–59.

41. Lengyel J, Hnath E, Storms M, Wohlfarth T. Towards an integrative structural biology approach: combining Cryo-TEM, X-ray crystallography, and NMR. J Struct Funct Genomics. 2014;15(3):117–24.
42. Gremer L, Schölzel D, Schenk C, Reinartz E, Labahn J, Ravelli RBG, et al. Fibril structure of amyloid-b(1-42) by cryo-electron microscopy
43. Fitzpatrick AWP, Falcon B, He S, Murzin AG, Murshudov G, Garringer HJ, et al. Cryo-EM structures of tau filaments from Alzheimer's disease. Nature. 2017;547(7662):185–90.
44. Kopeček J, Yang J. Peptide-directed self-assembly of hydrogels. Acta Biomateriali. 2009;5(3):805–16.
45. Xuan Q, Wang Y, Chen C, Wang P. Rational Biological Interface Engineering: Amyloidal Supramolecular Microstructure-Inspired Hydrogel. Vol. 9, Frontiers in Bioengineering and Biotechnology. Frontiers Media S.A.; 2021.
46. Kaith BS, Singh A, Sharma AK, Sud D. Hydrogels: Synthesis, Classification, Properties and Potential Applications—A Brief Review. J Polym Environ. 2021;29(12):3827–41.
47. Veloso SRS, Magalhães CAB, Rodrigues ARO, Vilaça H, Queiroz MJRP, Martins JA, et al. Novel dehydropeptide-based magnetogels containing manganese ferrite nanoparticles as antitumor drug nanocarriers. Physical Chemistry Chemical Physics. 2019;21(20):10377–90.
48. Orbach R, Adler-Abramovich L, Zigerson S, Mironi-Harpaz I, Seliktar D, Gazit E. Self-assembled Fmoc-peptides as a platform for the formation of nanostructures and hydrogels. Biomacromolecules. 2009 10(9):2646–51.
49. Liu X, Mao C, He G, Pan X, Liu X, Zhu Y, et al. Hif-1α-mediated mitophagy determines zno nanoparticle-induced human osteosarcoma cell death both in vitro and in vivo. ACS Appl Mater Interfaces. 2020 12(43):48296–309.
50. De Groot NS, Parella T, Aviles FX, Vendrell J, Ventura S. Ile-Phe dipeptide self-assembly: Clues to amyloid formation. Biophys J. 2007;92(5):1732–41.
51. Fichman G, Gazit E. Self-assembly of short peptides to form hydrogels: Design of building blocks, physical properties and technological applications. Vol. 10, Acta Biomaterialia. Elsevier Ltd; 2014 :1671–82.
52. Oliveira CBP, Gomes V, Ferreira PMT, Martins JA, Jervis PJ. Peptide-Based Supramolecular Hydrogels as Drug Delivery Agents: Recent Advances. Gels. 2022;8(11).
53. Jayawarna V, Ali M, Jowitt TA, Miller AF, Saiani A, Gough JE, et al. Nanostructured hydrogels for three-dimensional cell culture through self-assembly of fluorenylmethoxycarbonyl-dipeptides. Advanced Materials. 2006;18(5):611–4.
54. Marchesan S, Vargiu A V., Styan KE. The Phe-Phe motif for peptide self-assembly in nanomedicine. Vol. 20, Molecules. MDPI AG; 2015:19775–88.
55. Ghosh M, Bera S, Schiffmann S, Shimon LJW, Adler-Abramovich L. Collagen-Inspired Helical Peptide Coassembly Forms a Rigid Hydrogel with Twisted Polyproline II Architecture. ACS Nano. 2020;14(8):9990–10000.
56. Li Y, Yang G, Gerstweiler L, Thang SH, Zhao CX. Design of Stimuli-Responsive Peptides and Proteins. Adv Funct Mater. 2023;33(7):1–31.
57. Garcia-Sampedro A, Tabero A, Mahamed I, Acedo P. Multimodal use of the porphyrin TMPyP: From cancer therapy to antimicrobial applications. In: Porphyrin Science By Women (In 3 Volumes). World Scientific Publishing Co.; 2020: 11–27.
58. Billah A. Investigation of multiferroic and photocatalytic properties of Li doped BiFeO3 nanoparticles prepared by ultrasonication. 2016.

59. Tehrani Nejad S, Rahimi R, Rabbani M, Rostamnia S. Zn (II)-porphyrin-based photochemically green synthesis of novel ZnTPP/Cu nanocomposites with antibacterial activities and cytotoxic features against breast cancer cells. Sci Rep. 2022;12(1).
60. Norvaiša K, Kielmann M, Senge MO. Porphyrins as Colorimetric and Photometric Biosensors in Modern Bioanalytical Systems. Vol. 21, ChemBioChem. Wiley-VCH Verlag; 2020: 1793–807.
61. Baglia RA, Zaragoza JPT, Goldberg DP. Biomimetic Reactivity of Oxygen-Derived Manganese and Iron Porphyrinoid Complexes. Vol. 117, Chemical Reviews. American Chemical Society; 2017 :13320–52.
62. Hiroto S, Miyake Y, Shinokubo H. Synthesis and Functionalization of Porphyrins through Organometallic Methodologies. Vol. 117, Chemical Reviews. American Chemical Society; 2017. p. 2910–3043.
63. Jiang YB, Sun Z. Self-Assembled porphyrin and macrocycle derivatives: From synthesis to function. MRS Bull. 2019;44(3):167–71.
64. Funahashi S, Inada Y, Inamo M. Dynamic Study of Metal-Ion Incorporation into Porphyrins Based on the Dynamic Characterization of Metal Ions and on Sitting-Atop Complex Formation. ANALYTICAL SCIENCES. 2001;17:917–27.
65. Guterres KB, Rossi GG, Menezes LB, Anraku de Campos MM, Iglesias BA. Preliminary evaluation of the positively and negatively charge effects of tetra-substituted porphyrins on photoinactivation of rapidly growing mycobacteria. Tuberculosis. 2019 Jul 1;117:45–51.
66. Cocca LHZ, Gotardo F, Sciuti LF, Acunha T V., Iglesias BA, de Boni L. Investigation of excited singlet state absorption and intersystem crossing mechanism of isomeric meso-tetra(pyridyl)porphyrins containing peripheral polypyridyl platinum(II) complexes. Chem Phys Lett. 2018 Sep 16;708:1–10.
67. Maisch T, Rgen Baier J, Franz B, Maier M, Landthaler M, Szeimies RM, et al. The role of singlet oxygen and oxygen concentration in photodynamic inactivation of bacteria. PNAS . 2007;104(17):7223–8.
68. Oyim J, Omolo CA, Amuhaya EK. Photodynamic Antimicrobial Chemotherapy: Advancements in Porphyrin-Based Photosensitize Development. Front Chem. 2021;9.
69. Tian J, Huang B, Hasnain Nawaz M, Zhang W. Review of porphyrin-based photodynamic therapy materials. Coord Chem Rev. 2020;420:212–410.
70. Beyene BB, Wassie GA. Antibacterial activity of Cu(II) and Co(II) porphyrins: Role of ligand modification. BMC Chem. 2020;14(51).
71. Zhang Q, He J, Yu W, Li Y, Liu Z, Zhou B, et al. A promising anticancer drug: A photosensitizer based on the porphyrin skeleton. Vol. 11, RSC Medicinal Chemistry. Royal Society of Chemistry; 2020. p. 427–37.
72. Zou R, Wang Q, Wu J, Wu J, Schmuck C, Tian H. Peptide self-assembly triggered by metal ions. Chem Soc Rev. 2015 Aug 7;44(15):5200–19.
73. Permyakov EA. Metal Binding Proteins. Encyclopedia. 2021 Mar 15;1(1):261–92.
74. Tashiro S, Shionoya M. Stimuli-responsive synthetic metallopeptides. Chemistry Letters. 2013;42: 456–62.
75. Umadevi P, Senthilkumar L. Influence of metal ions (Zn^{2+}, Cu^{2+}, Ca^{2+}, Mg^{2+} and Na^{+}) on the water coordinated neutral and zwitterionic l-histidine dimer. RSC Adv. 2014;4(90):49040–52.
76. Liao SM, Du QS, Meng JZ, Pang ZW, Huang RB. The multiple roles of histidine in protein interactions. Chem Cent J. 2013;7(1).
77. You C, Piehler J. Multivalent chelators for spatially and temporally controlled protein functionalization. Anal Bioanal Chem. 2014;406(14):3345–57.

78. López-Laguna H, Voltà-Durán E, Parladé E, Villaverde A, Vázquez E, Unzueta U. Insights on the emerging biotechnology of histidine-rich peptides. Biotechnol Adv. 2022;54.
79. Wątły J, Hecel A, Rowińska-Żyrek M, Kozłowski H. Impact of histidine spacing on modified polyhistidine tag – Metal ion interactions. Inorganica Chim Acta. 2018 Mar 1;472:119–26.
80. Dmitriev RI, O'Donnell N, Papkovsky DB. Metallochelate Coupling of Phosphorescent Pt-Porphyrins to Peptides, Proteins, and Self-Assembling Protein Nanoparticles. Bioconjug Chem. 2016;27(2):439–45.
81. June RK, Gogoi K, Eguchi A, Cui XS, Dowdy SF. Synthesis of a pH-sensitive nitrilotriacetic linker to peptide transduction domains to enable intracellular delivery of histidine imidazole ring-containing macromolecules. J Am Chem Soc. 2010;132(31):10680–2.
82. Bassan GA, Marchesan S. Peptide-Based Materials That Exploit Metal Coordination. Vol. 24, International Journal of Molecular Sciences. MDPI; 2023.
83. Mahakal S, Suse S. Amino acid Adapted Metal and Metals Oxides. 2020;9(12):107–19. Available from: www.ijert.org
84. Fernández-Garcia M, Rodriguez JA. Metal Oxide Nanoparticles. 2007.
85. Cao Y, Dhahad HA, El-Shorbagy MA, Alijani HQ, Zakeri M, Heydari A, et al. Green synthesis of bimetallic ZnO–CuO nanoparticles and their cytotoxicity properties. Sci Rep. 2021;11(1).
86. Makvandi P, Gu JT, Zare EN, Ashtari B, Moeini A, Tay FR, et al. Polymeric and inorganic nanoscopical antimicrobial fillers in dentistry. Acta Biomaterialia. Acta Materialia Inc; 2020;101:69–101.
87. Pasquet J, Chevalier Y, Pelletier J, Couval E, Bouvier D, Bolzinger MA. The contribution of zinc ions to the antimicrobial activity of zinc oxide. Colloids Surf A Physicochem Eng Asp. 2014;457(1):263–74.
88. Ji P, Wang P, Chen H, Xu Y, Ge J, Tian Z, et al. Potential of Copper and Copper Compounds for Anticancer Applications. Pharmaceuticals. MDPI; 2023;16
89. Chakraborty S, Prakash P, Shah J, Mayya C, Singh S, Ranganathan R, et al. CuO Nanoparticles as Copper-Ion Reservoirs for Elesclomol-Mediated Intracellular Oxidative Stress: Implications for Anticancer Therapies. ACS Appl Nano Mater. 2022;5(1):1607–20.
90. Remko M, Fitz D, Rode BM. Effect of metal ions (Li^+, Na^+, K^+, Mg^{2+}, Ca^{2+}, Ni^{2+}, Cu^{2+} and Zn^{2+}) and water coordination on the structure and properties of l-histidine and zwitterionic l-histidine. Amino Acids. 2010;39(5):1309–19.
91. Zechel S, Hager MD, Priemel T, Harrington MJ. Healing through histidine: Bioinspired pathways to self-healing polymers via imidazole-metal coordination. Biomimetics. 2019;4(1):1–21.
92. Fitz D, Jakschitz T, Rode BM. The catalytic effect of l- and d-histidine on alanine and lysine peptide formation. J Inorg Biochem. 2008;102(12):2097–102.
93. Dudev T, Lim C. Metal binding affinity and selectivity in metalloproteins: Insights from computational studies. Vol. 37, Annual Review of Biophysics. 2008. p. 97–116.
94. Harding MM, Nowicki MW, Walkinshaw MD. Metals in protein structures: A review of their principal features. Vol. 16, Crystallography Reviews. 2010. p. 247–302.
95. John J V., Uthaman S, Augustine R, Chen H, Park IK, Kim I. PH/redox dual stimuli-responsive sheddable nanodaisies for efficient intracellular tumour-triggered drug delivery. J Mater Chem B. 2017;5(25):5027–36.

96. Zhu J, Guo X, Guo T, Yang Y, Cui X, Pan J, et al. Novel pH-responsive and self-assembled nanoparticles based on Bletilla striata polysaccharide: preparation and characterization. RSC Adv. 2018;8(70):40308–20.
97. Bayda S, Adeel M, Tuccinardi T, Cordani M, Rizzolio F. The history of nanoscience and nanotechnology: From chemical-physical applications to nanomedicine. Molecules. 2020;25(112).
98. Semnani D. Geometrical characterization of electrospun nanofibers. In: Electrospun Nanofibers. Elsevier Inc.; 2017:151–80.
99. Billah A. Investigation of multiferroic and photocatalytic properties of Li doped BiFeO3 nanoparticles prepared by ultrasonication. 2016.
100. Pathan AK, Bond J, Gaskin RE. Sample preparation for scanning electron microscopy of plant surfaces-Horses for courses. Micron. 2008;39:1049–61.
101. Curry A, Appleton H, Dowsett B. Application of transmission electron microscopy to the clinical study of viral and bacterial infections: Present and future. Micron. 2006; 37:91–106.
102. Geelen D, Thete A, Schaff O, Kaiser A, van der Molen SJ, Tromp R. eV-TEM: Transmission electron microscopy in a low energy cathode lens instrument. Ultramicroscopy. 2015;159:482–7.
103. Prencipe I, Dellasega D, Zani A, Rizzo D, Passoni M. Energy dispersive x-ray spectroscopy for nanostructured thin film density evaluation. Sci Technol Adv Mater. 2015;16(2).
104. Khurana R, Uversky VN, Nielsen L, Fink AL. Is Congo Red an Amyloid-specific Dye? Journal of Biological Chemistry. 2001;276(25):22715–21.
105. George G, Wilson R, Joy J. Chapter 3 - Ultraviolet Spectroscopy: A Facile Approach for the Characterization of Nanomaterials. In: Thomas S, Thomas R, Zachariah AK, Mishra RK, editors. Spectroscopic Methods for Nanomaterials Characterization. Elsevier; 2017:55–72. (Micro and Nano Technologies).
106. Shabanian M, Hajibeygi M, Raeisi A. FTIR characterization of layered double hydroxides and modified layered double hydroxides. In: Layered Double Hydroxide Polymer Nanocomposites. 2020: 77–101.
107. Mohamed Shameer P, Mohamed Nishath P. Exploration and enhancement on fuel stability of biodiesel: A step forward in the track of global commercialization. In: Advanced Biofuels: Applications, Technologies and Environmental Sustainability. Elsevier; 2019: 181–213.
108. Ma YZ, Sobernheim D, Garzon JR. Glossary for Unconventional Oil and Gas Resource Evaluation and Development. In: Unconventional Oil and Gas Resources Handbook: Evaluation and Development. Elsevier Inc.; 2016. p. 513–26.
109. Ferrara M, Lugano G, Sandinha MT, Kearns VR, Geraghty B, Steel DHW. Biomechanical properties of retina and choroid: a comprehensive review of techniques and translational relevance. Eye. 2021;35(7):1818–32.
110. Mihai MM, Dima MB, Dima B, Holban AM. Nanomaterials for wound healing and infection control. Materials. 2019;12(13).
111. Llor C, Bjerrum L. Antimicrobial resistance: Risk associated with antibiotic overuse and initiatives to reduce the problem. Therapeutic Advances in Drug Safety. 2014;5:229–41.
112. Souza THS, Sarmento-Neto JF, Souza SO, Raposo BL, Silva BP, Borges CPF, et al. Advances on antimicrobial photodynamic inactivation mediated by Zn(II) porphyrins. Journal of Photochemistry and Photobiology C: Photochemistry Reviews. Elsevier B.V.; 2021;49

113. Jiang L, Gan CRR, Gao J, Loh XJ. A Perspective on the Trends and Challenges Facing Porphyrin-Based Anti-Microbial Materials. Small. 2016;12:3609–44.
114. Kou J, Dou D, Yang L. Porphyrin photosensitizers in photodynamic therapy and its applications. Oncotarget. 2017;8(46):81591–603.
115. Agostinis P, Berg K, Cengel KA, Foster TH, Girotti AW, Gollnick SO, et al. Photodynamic therapy of cancer: An update. CA Cancer J Clin. 2011;61(4):250–81.
116. Feng X, Liu C, Wang X, Jiang Y, Yang G, Wang R, et al. Functional supramolecular gels based on the hierarchical assembly of porphyrins and phthalocyanines. Frontiers in Chemistry. 2019; 7
117. Wang R, Ko CH, Brugh AM, Bai Y, Forbes MDE, Therien MJ. Topology, Distance, and Orbital Symmetry Effects on Electronic Spin-Spin Couplings in Rigid Molecular Systems: Implications for Long-Distance Spin-Spin Interactions. Journal of Physical Chemistry A. 2020;124(37):7411–5.
118. Marciel L, Mesquita MQ, Ferreira R, Moreira B, Pms Neves MG, F Faustino MA, et al. An efficient formulation based on cationic porphyrins to photoinactivate Staphylococcus aureus and Escherichia coli. Future Med Chem. 2018;10(15):1821–33.
119. Ajloo D, Hajipour S, Saboury AA, Zakavi S. Effect of cationic and anionic porphyrins on the structure and activity of adenosine deaminase. Bull Korean Chem Soc. 2011;32(9):3411–20.
120. Lesar A, Mušković M, Begić G, Lončarić M, Linšak DT, Malatesti N, et al. Cationic porphyrins as effective agents in photodynamic inactivation of opportunistic plumbing pathogen legionella pneumophila. Int J Mol Sci. 2020;21(15):1–18.
121. Li Y, Yang Y, Qing Y, Li R, Tang X, Guo D, et al. Enhancing zno-np antibacterial and osteogenesis properties in orthopedic applications: A review. Vol. 15, International Journal of Nanomedicine. Dove Medical Press Ltd; 2020: 6247–62.
122. Arakawa H, Takeda K, Higashi SL, Shibata A, Kitamura Y, Ikeda M. Self-assembly and hydrogel formation ability of Fmoc-dipeptides comprising α-methyl-L-phenylalanine. Polym J. 2020;52(8):923–30.
123. Mahler A, Reches M, Rechter M, Cohen S, Gazit E. Rigid, self-assembled hydrogel composed of a modified aromatic dipeptide. Advanced Materials. 2006;18(11):1365–70.
124. Dandash F, Leger DY, Diab-Assaf M, Sol V, Liagre B. Porphyrin/chlorin derivatives as promising molecules for therapy of colorectal cancer. Molecules. MDPI. 2021; 26,
125. Ma X, Sun X, Hargrove D, Chen J, Song D, Dong Q, et al. A Biocompatible and Biodegradable Protein Hydrogel with Green and Red Autofluorescence: Preparation, Characterization and in Vivo Biodegradation Tracking and Modeling. Sci Rep. 2016;6.
126. Fischenich KM, Lewis JT, Bailey TS, Haut Donahue TL. Mechanical viability of a thermoplastic elastomer hydrogel as a soft tissue replacement material. J Mech Behav Biomed Mater. 2018;79:341–7.
127. Arda K, Ciledag N, Aktas E, Aribas BK, Köse K. Quantitative assessment of normal soft-tissue elasticity using shear-wave ultrasound elastography. American Journal of Roentgenology. 2011;197(3):532–6.
128. Criado-Gonzalez M, Iqbal MH, Carvalho A, Schmutz M, Jierry L, Schaaf P, et al. Surface Triggered Self-Assembly of Fmoc-Tripeptide as an Antibacterial Coating. Front Bioeng Biotechnol. 2020;8.
129. Rima M, Rima M, Fajloun Z, Sabatier JM, Bechinger B, Naas T. Antimicrobial peptides: A potent alternative to antibiotics. Antibiotics. 2021;10(9).
130. Brady C, Bell SEJ, Parsons C, Gorman SP, Jones DS, McCoy CP. Novel porphyrin-incorporated hydrogels for photoactive intraocular lens biomaterials. Journal of Physical Chemistry B. 2007;111(3):527–34.

131. Kim JH, Nam DH, Lee YW, Nam YS, Park CB. Self-assembly of metalloporphyrins into light-harvesting peptide nanofiber hydrogels for solar water oxidation. Small. 2014;10(7):1272–7.
132. Li J, Mooney DJ. Designing hydrogels for controlled drug delivery. Nature Reviews Materials. 2016; 1
133. Calvo JJ, Angel SM, So MC. Charge transport in metal-organic frameworks for electronics applications. Vol. 8, APL Materials. American Institute of Physics Inc.; 2020.
134. Elkihel A, Christie C, Vernisse C, Ouk TS, Lucas R, Chaleix V, et al. Xylan-Based Cross-Linked Hydrogel for Photodynamic Antimicrobial Chemotherapy. ACS Appl Bio Mater. 2021;
135. Yegorov YE, Vishnyakova KS, Pan X, Egorov AE, Popov K V., Tevonyan LL, et al. Mechanisms of Phototoxic Effects of Cationic Porphyrins on Human Cells In Vitro. Molecules. 2023;28(3).
136. McCloskey AP, Draper ER, Gilmore BF, Laverty G. Ultrashort self-assembling Fmoc-peptide gelators for anti-infective biomaterial applications. Journal of Peptide Science. 2017;23(2):131–40.
137. Gomes MC, Woranovicz-Barreira SM, Faustino MAF, Fernandes R, Neves MGPMS, Tomé AC, et al. Photodynamic inactivation of Penicillium chrysogenum conidia by cationic porphyrins. Photochemical and Photobiological Sciences. 2011;10(11):1735–43.
138. Ashkenazi H, Nitzan Y, Gá D. Photodynamic Effects of Antioxidant Substituted Porphyrin Photosensitizers on Gram-positive and-negative Bacteria. Photochem Photobiol. 2003;77(2):186–91.
139. Fayyaz F, Rassa M, Rahimi R. Antibacterial Photoactivity and Thermal Stability of Tetra-cationic Porphyrins Immobilized on Cellulosic Fabrics. Photochem Photobiol. 2021;97(2):385–97.
140. Espitia-Almeida F, Díaz-Uribe C, Vallejo W, Gómez-Camargo D, Romero Bohórquez AR. In vitro anti-leishmanial effect of metallic meso-substituted porphyrin derivatives against leishmania braziliensis and leishmania panamensis promastigotes properties. Molecules. 2020;25(8).
141. Huang L, Dai T, Hamblin MR. Antimicrobial photodynamic inactivation and photodynamic therapy for infections. Methods in Molecular Biology. 2010;635:155–73.
142. Dontas IA, Lelovas P, Parara S, Galanos A, Agrogiannis G, Goutas D, et al. Delivery of Porphyrins through Self-Assembling Peptide Hydrogels for Accelerated Healing of Experimental Skin Defects In Vivo. Cureus . 2023;1–17.
143. Glymenaki E, Kandyli M, Apostolidou CP, Kokotidou C, Charalambidis G, Nikoloudakis E, et al. Design and Synthesis of Porphyrin-Nitrilotriacetic Acid Dyads with Potential Applications in Peptide Labeling through Metallochelate Coupling. ACS Omega. 2022;7(2):1803–18.
144. Ong SE, Mann M. A practical recipe for stable isotope labeling by amino acids in cell culture (SILAC). Nat Protoc. 2007;1(6):2650–60.
145. Di Benedetto F, Mele E, Camposeo A, Athanassiou A, Cingolani R, Pisignano D. Photoswitchable organic nanofibers. Advanced Materials. 2008 Jan 18;20(2):314–8.
146. van Staveren DR, Metzler-Nolte N. Bioorganometallic chemistry of ferrocene. Chem Rev. 2004 Dec;104(12):5931–85.
147. Domon B, Aebersold R. Mass spectrometry and protein analysis. Science. 2006; 312: 212–7.

148. Sahoo H. Fluorescent labeling techniques in biomolecules: A flashback. RSC Advances. 2012;2:7017–29.
149. Sameiro M, Gonçalves T. Fluorescent labeling of biomolecules with organic probes. Chem Rev. 2009;109(1):190–212.
150. Lotze J, Reinhardt U, Seitz O, Beck-Sickinger AG. Peptide-tags for site-specific protein labelling: In vitro and in vivo. Mol Biosyst. 2016;12(6):1731–45.
151. Lai YT, Chang YY, Hu L, Yang Y, Chao A, Du ZY, et al. Rapid labeling of intracellular His-tagged proteins in living cells. Proc Natl Acad Sci U S A. 2015 Mar 10;112(10):2948–53.
152. Konopińska K, Pietrzak M, Mazur R, Malinowska E. Tetraphenylporphyrin as a protein label for triple detection analytical systems. Heliyon. 2015;1(4).
153. Konopińska K, Pietrzak M, Malinowska E. Manganese porphyrins - Studies on their potential use for protein labeling. Microchemical Journal. 2014;115:1–5.
154. Diaferia C, Morelli G, Accardo A. Fmoc-diphenylalanine as a suitable building block for the preparation of hybrid materials and their potential applications. J Mater Chem B. 2019;7(34):5142–55.
155. Zapp C, Minsky BB, Boehm H. Tuning RGD motif and hyaluronan density to study integrin binding. Front Physiol. 2018;9.
156. Mizejewski GJ. Role of Integrins in Cancer: Survey of Expression Patterns. Proceedings of the Society for Experimental Biology and Medicine. 1999;222(2):124–38.
157. Jonnalagadda SVR, Ornithopoulou E, Orr AA, Mossou E, Trevor Forsyth V, Mitchell EP, et al. Computational design of amyloid self-assembling peptides bearing aromatic residues and the cell adhesive motif Arg-Gly-Asp. Mol Syst Des Eng. 2017;2(3):321–35.
158. Deidda G, Jonnalagadda SVR, Spies JW, Ranella A, Mossou E, Forsyth VT, et al. Self-Assembled Amyloid Peptides with Arg-Gly-Asp (RGD) Motifs As Scaffolds for Tissue Engineering. ACS Biomater Sci Eng. 2017;3(7):1404–16.
159. Hiyama K, Matsui H, Tamura M, Shimokawa O, Hiyama M, Kaneko T, et al. Cancer cells uptake porphyrins via heme carrier protein 1. J Porphyr Phthalocyanines. 2013;17(1–2):36–43.
160. Park J, Singha K, Son S, Kim J, Namgung R, Yun CO, et al. A review of RGD-functionalized nonviral gene delivery vectors for cancer therapy. Cancer Gene Therapy. 2012;19:741–8.
161. Song Z, Lin Y, Zhang X, Feng C, Lu Y, Gao Y, et al. Cyclic RGD peptide-modified liposomal drug delivery system for targeted oral apatinib administration: Enhanced cellular uptake and improved therapeutic effects. Int J Nanomedicine. 2017;12:1941–58.
162. Desgrosellier JS, Cheresh DA. Integrins in cancer: Biological implications and therapeutic opportunities. Nature Reviews Cancer. 2010;10:9–22.
163. Orgovan N, Peter B, Bosze S, Ramsden JJ, Szabó B, Horvath R. Dependence of cancer cell adhesion kinetics on integrin ligand surface density measured by a high-throughput label-free resonant waveguide grating biosensor. Sci Rep. 2014;4.
164. Jin P, Sha R, Zhang Y, Liu L, Bian Y, Qian J, et al. Blood Circulation-Prolonging Peptides for Engineered Nanoparticles Identified via Phage Display. Nano Lett. 2019;19(3):1467–78.
165. Li F, Zhao Y, Mao C, Kong Y, Ming X. RGD-Modified Albumin Nanoconjugates for Targeted Delivery of a Porphyrin Photosensitizer. Mol Pharm. 2017;14(8):2793–804.

166. Midoux P, Kichler A, Boutin V, Maurizot JC, Monsigny M. Membrane Permeabilization and Efficient Gene Transfer by a Peptide Containing Several Histidines. Bioconjugate Chem. 1998;9:260–7.
167. Palomo JM. Nanobiohybrids: A new concept for metal nanoparticles synthesis., Chemical Communications. Royal Society of Chemistry; 2019;55: 9583–9.
168. Abbas M, Susapto HH, Hauser CAE. Synthesis and Organization of Gold-Peptide Nanoparticles for Catalytic Activities. ACS Omega. 2022;7(2):2082–90.
169. Jeong W jin, Bu J, Kubiatowicz LJ, Chen SS, Kim YS, Hong S. Peptide–nanoparticle conjugates: a next generation of diagnostic and therapeutic platforms? Vol. 5, Nano Convergence. Korea Nano Technology Research Society; 2018.
170. Elango M, Deepa M, Subramanian R, Mohamed Musthafa A. Synthesis, Characterization, and Antibacterial Activity of Polyindole/Ag–Cuo Nanocomposites by Reflux Condensation Method. Polymer - Plastics Technology and Engineering. 2018;57(14):1440–51.
171. Nasrolahi Shirazi A, Mandal D, Tiwari RK, Guo L, Lu W, Parang K. Cyclic peptide-capped gold nanoparticles as drug delivery systems. Mol Pharm. 2013;10(2):500–11.
172. Tan YN, Lee JY, Wang DIC. Uncovering the design rules for peptide synthesis of metal nanoparticles. J Am Chem Soc. 2010;132(16):5677–86.
173. Sidhu AK, Verma N, Kaushal P. Role of Biogenic Capping Agents in the Synthesis of Metallic Nanoparticles and Evaluation of Their Therapeutic Potential. Frontiers in Nanotechnology. Frontiers Media S.A.; 2022; 3
174. Uthaman S, Huh KM, Park IK. Tumor microenvironment-responsive nanoparticles for cancer theragnostic applications. Biomaterials Research. BioMed Central Ltd.; 2018;22
175. Sutherland E, Harding CJ, Czekster CM. Active site remodelling of a cyclodipeptide synthase redefines substrate scope. Commun Chem. 2022;5(1).
176. Lim YY, Zaidi AMA, Miskon A. Combining Copper and Zinc into a Biosensor for Anti-Chemoresistance and Achieving Osteosarcoma Therapeutic Efficacy. Vol. 28, Molecules. MDPI; 2023.
177. Usman MS, Ibrahim NA, Shameli K, Zainuddin N, Yunus WMZW. Copper nanoparticles mediated by chitosan: Synthesis and characterization via chemical methods. Molecules. 2012;17(12):14928–36.
178. Rafie Johan M, Shahadan Mohd Suan M, Liza Hawari N, Ay Ching H. Annealing Effects on the Properties of Copper Oxide Thin Films Prepared by Chemical Deposition. Int J Electrochem Sci. 2011;6:6094–104.
179. Sharma M, Sharma A, Majumder S. Synthesis, microbial susceptibility and anti-cancerous properties of copper oxide nanoparticles- review. Nano Express. 2020;1(1).
180. Maret W, Wedd A. Binding, Transport and Storage of Metal Ions in Biological Cells. The Royal Society of Chemistry . 2014.
181. Gudkov S V., Burmistrov DE, Serov DA, Rebezov MB, Semenova AA, Lisitsyn AB. A Mini Review of Antibacterial Properties of ZnO Nanoparticles. Front Phys. 2021;9.
182. Abebe B, Zereffa EA, Tadesse A, Murthy HCA. A Review on Enhancing the Antibacterial Activity of ZnO: Mechanisms and Microscopic Investigation. Nanoscale Res Lett. 2020;15(1).
183. Zhang S, Cao C, Lv X, Dai H, Zhong Z, Liang C, et al. A H2O2 self-sufficient nanoplatform with domino effects for thermal-responsive enhanced chemodynamic therapy. Chem Sci. 2020;11(7):1926–34.
184. Matsubara T, DiResta GR, Kakunaga S, Li D, Healey JH. Additive influence of extracellular pH, oxygen tension, and pressure on invasiveness and survival of human osteosarcoma cells. Front Oncol. 2013;3(1).

185. Lim YY, Zaidi AMA, Miskon A. Combining Copper and Zinc into a Biosensor for Anti-Chemoresistance and Achieving Osteosarcoma Therapeutic Efficacy. Vol. 28, Molecules. MDPI; 2023.
186. Cheignon C, Tomas M, Bonnefont-Rousselot D, Faller P, Hureau C, Collin F. Oxidative stress and the amyloid beta peptide in Alzheimer's disease. Vol. 14, Redox Biology. Elsevier B.V.; 2018. p. 450–64.
187. Shen F, Fang Y, Wu Y, Zhou M, Shen J, Fan X. Metal ions and nanometallic materials in antitumor immunity: Function, application, and perspective. J Nanobiotechnology. 2023;21(1).
188. Bellezza I, Peirce MJ, Minelli A. Cyclic Peptides in Neurological Disorders: The Case of Cyclo(His-Pro). In: Quorum Sensing: Molecular Mechanism and Biotechnological Application. Elsevier; 2019. p. 257–86.
189. Ning B, Liu Y, Huang T, Wei Y. Autophagy and its role in osteosarcoma. Cancer Med. 2023;12(5):5676–87.
190. Mendes CR, Dilarri G, Forsan CF, Sapata V de MR, Lopes PRM, de Moraes PB, et al. Antibacterial action and target mechanisms of zinc oxide nanoparticles against bacterial pathogens. Sci Rep. 2022 Dec 1;12(1).
191. Nguyen TN, Do QH, Vu TTD, Nguyen TT, Nguyen DT, Nguyen TBN, et al. Enhancement of antibacterial activity by a copper(II) and zinc(II) in chelation with ethylenediaminetetra-acetic acid and urea complex. Chemical Papers. 2022;76(11):7163–76.
192. Siddiqi KS, ur Rahman A, Tajuddin, Husen A. Properties of Zinc Oxide Nanoparticles and Their Activity Against Microbes. Vol. 13, Nanoscale Research Letters. Springer New York LLC; 2018.
193. Macomber L, Imlay JA. The iron-sulfur clusters of dehydratases are primary intracellular targets of copper toxicity. PNAS. 2009;106(20):8344–9.
194. Seo J, Hoffmann W, Warnke S, Huang X, Gewinner S, Schöllkopf W, et al. An infrared spectroscopy approach to follow β-sheet formation in peptide amyloid assemblies. Nat Chem. 2017;9(1):39–44.
195. Yang H, Pritzker M, Fung SY, Sheng Y, Wang W, Chen P. Anion effect on the nanostructure of a metal Ion binding self-assembling peptide. Langmuir. 2006;22(20):8553–62.
196. Fadlelmoula A, Pinho D, Carvalho VH, Catarino SO, Minas G. Fourier Transform Infrared (FTIR) Spectroscopy to Analyse Human Blood over the Last 20 Years: A Review towards Lab-on-a-Chip Devices. Vol. 13, Micromachines. MDPI; 2022.
197. Celik S, Ozel AE, Kecel S, Akyuz S. Structural and IR and Raman spectral analysis of cyclo(His-Phe) dipeptide. Vib Spectrosc. 2012;61:54–65.
198. Reddy PR, Radhika M, Manjula P. Synthesis and characterization of mixed ligand complexes of Zn(II) and Co(II) with amino acids: Relevance to zinc binding sites in zinc fingers. J Chem Sci. 2005;117(3):239–46.
199. Faheem M, Siddiqi HM, Habib A, Shahid M, Afzal A. ZnO/Zn(OH)2 nanoparticles and self-cleaning coatings for the photocatalytic degradation of organic pollutants. Front Environ Sci. 2022;10.
200. Gustiananda M, Haris PI, Milburn PJ, Gready JE. Copper-induced conformational change in a marsupial prion protein repeat peptide probed using FTIR spectroscopy. FEBS Lett. 2002;512:38–42.
201. Sreevalsa VG, Jeeju PP, Augustine MS, Anilkumar KM, Jayalekshmi S. L-Histidine-modified biocompatible zinc oxide nanocrystals. J Exp Nanosci. 2013;8(7–8):937–46.
202. Chohan ZH, Arif M, Akhtar MA, Supuran CT. Metal-based antibacterial and antifungal agents: Synthesis, characterization, and in vitro biological evaluation of

Co(II), Cu(II), Ni(II), and Zn(II) complexes with amino acid-derived compounds. Bioinorg Chem Appl. 2006;2006.
203. McCleland K, Milne PJ, Lucieto FR, Frost C, Brauns SC, Van De Venter M, et al. An investigation into the biological activity of the selected histidine-containing diketopiperazines cyclo(His-Phe) and cyclo(His-Tyr). Journal of Pharmacy and Pharmacology. 2010;56(9):1143–53.
204. Bai X, Li L, Liu H, Tan L, Liu T, Meng X. Solvothermal synthesis of ZnO nanoparticles and anti-infection application in vivo. ACS Appl Mater Interfaces. 2015;7(2):1308–17.
205. Xiong L, Tong ZH, Chen JJ, Li LL, Yu HQ. Morphology-dependent antimicrobial activity of Cu/CuxO nanoparticles. Ecotoxicology. 2015;10:2067–72.
206. Ren G, Hu D, Cheng EWC, Vargas-Reus MA, Reip P, Allaker RP. Characterisation of copper oxide nanoparticles for antimicrobial applications. Int J Antimicrob Agents. 2009;33(6):587–90.
207. Tanna JA, Chaudhary RG, Gandhare N V., Rai AR, Yerpude S, Juneja HD. Copper nanoparticles catalysed an efficient one-pot multicomponents synthesis of chromenes derivatives and its antibacterial activity. J Exp Nanosci. 2016;11(11):884–900.
208. Shi P, Cheng Z, Zhao K, Chen Y, Zhang A, Gan W, et al. Active targeting schemes for nano-drug delivery systems in osteosarcoma therapeutics. J Nanobiotechnology. 2023;21(103).
209. Reed RB, Ladner DA, Higgins CP, Westerhoff P, Ranville JF. Solubility of nano-zinc oxide in environmentally and biologically important matrices. Environ Toxicol Chem. 2012;31(1):93–9.

8. Appendix

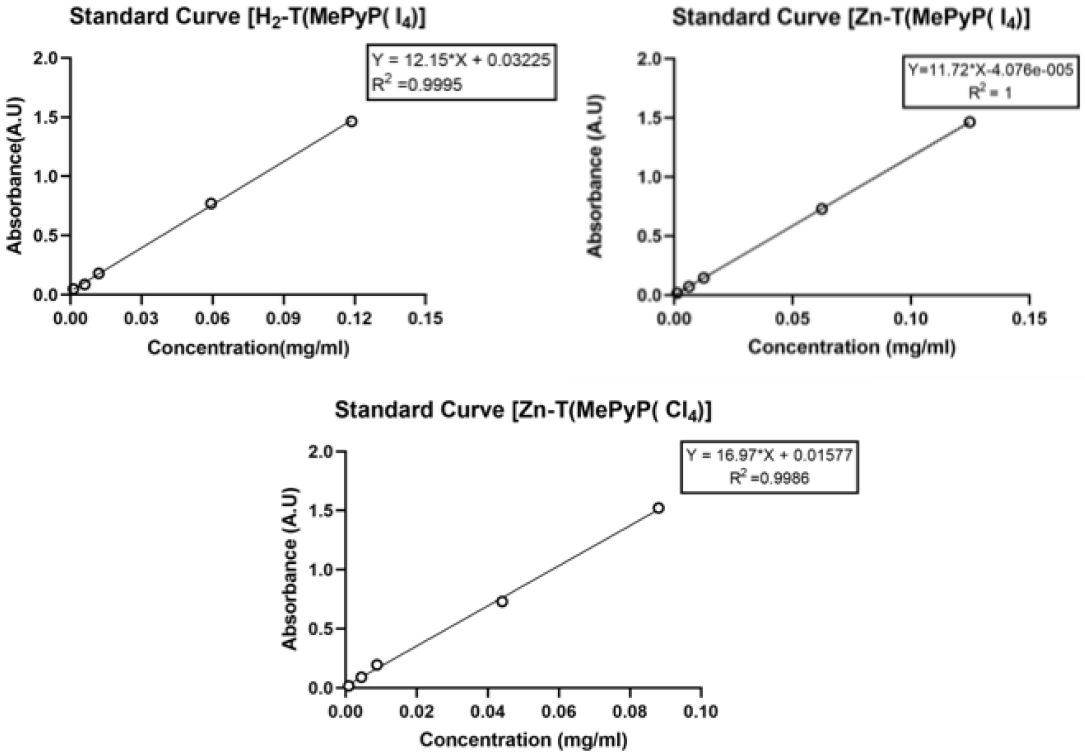

Figure 60: Standard Curves of porphyrin chromophores

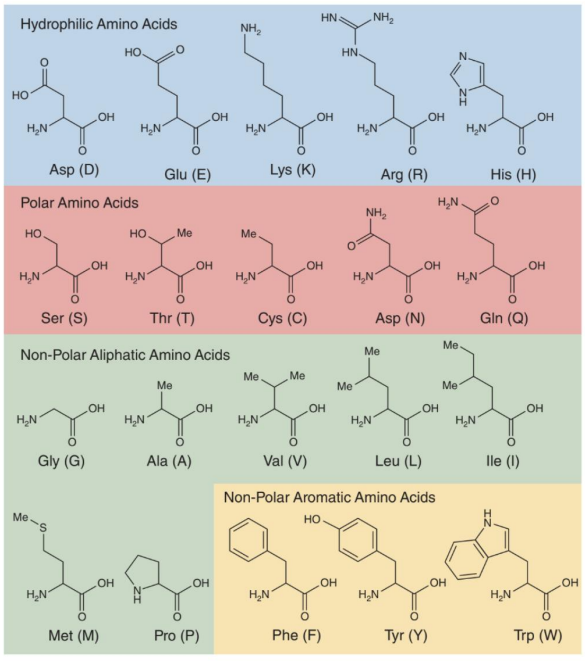

Structures and symbols of the 20 amino acids, which are directly encoded for protein synthesis by the standard genetic code.